



3 1176 00161 4818

NASA Contractor Report 159310

NASA CR-159, 310

NASA-CR-159310
19810003894

PARAMETRIC INFRARED TUNABLE LASER SYSTEM

M. Garbuny, T. Henningsen
and J. R. Sutter

Westinghouse Electric Corporation
Research and Development Center
Pittsburgh, PA 15235

LIBRARY COPY

DEC 16 1980

CONTRACT NAS1-13752
November 1980

SEARCH CENTER
LIBRARY, NASA
AMERICAN LIBRARIES



National Aeronautics and
Space Administration

Langley Research Center
Hampton, Virginia 23665



NF01105

PARAMETRIC INFRARED TUNABLE LASER SYSTEM

M. Garbuny, T. Henningsen
and J. R. Sutter

Westinghouse Electric Corporation
Research and Development Center
Pittsburgh, PA 15235

CONTRACT NAS1-13752
November 1980



National Aeronautics and
Space Administration

Langley Research Center
Hampton, Virginia 23665

N81-12405#

TABLE OF CONTENTS

	<u>Page</u>
ABSTRACT	1
1. INTRODUCTION	2
2. ALTERNATIVES OF SYSTEM CONSTRUCTION.	9
2.1 Functions and Methods.	9
2.2 Features of Angle Tuning [01.4] Grown LiNbO ₃	11
2.3 Plans for the Design of the Systems.	12
3. DEVELOPMENT OF THE LASER OSCILLATOR-AMPLIFIER CHAIN.	17
3.1 Initial Approach	17
3.2 Construction and Performance of the Stable SOAP:Nd Oscillator	18
3.3 Construction and Performance of the SOAP Amplifier Chain.	21
3.3.1 Faraday Rotator.	21
3.3.2 Test Procedures.	23
3.4 Material Quality as Barrier Problem of Performance.	24
3.5 Construction and Performance of the YAG:Nd System with Unstable Resonator.	26
3.5.1 Diffraction Coupled Resonator.	29
3.5.2 Transmission Coupled Unstable Resonator.	30
3.5.3 Two-Mirror Output Resonator.	31
3.5.4 Mode Structure and Radiation Damage.	33
3.5.5 Optimal Mirror Dimensions.	34
4. DEVELOPMENT OF THE OPTICAL PARAMETRIC CONVERTER.	42
4.1 Design Considerations for the Oscillator (OPO)	42
4.1.1 Grating.	45
4.1.2 Tilted Etalon.	46
4.2 Tuning Control and Display	50
4.3 Design, Supply, and Performance of LiNbO ₃ Crystals	53
4.3.1 Gain and Damage Limits	55
4.3.2 Control and Improvement of Crystal Quality.	56
4.3.3 Effect of Beam Diameter.	60
4.3.4 Tuning Range of LiNbO ₃ Crystals.	64
4.5 Development of the Optical Parametric Amplifier (OPA).	66

TABLE OF CONTENTS (cont'd)

	<u>Page</u>
5. PERFORMANCE TESTS AND CAPABILITY OF THE FINAL SYSTEM.	69
5.1 Test Conditions and Limitations	69
5.2 Test Procedures and Results	70
6. AUXILIARY SYSTEMS AND COMPONENTS.	78
7. CONCLUSIONS AND RECOMMENDATIONS	80
7.1 Acquisition of LiNbO ₃ Crystals.	80
7.2 Operation with the Parametric Amplifier	80
7.3 OPO Operation at the Limits of the Tuning Range .	81
7.4 Alternatives for Linewidth Reduction.	81
7.5 Variation of the Parametric Amplifier Arrangement .	82
8. APPLICATION OF THE SYSTEM TO ATMOSPHERIC MEASUREMENTS	85
8.1 Basic Relations	85
8.2 Considerations of Linewidth Compatibility	89
8.3 Examples for the Density Measurements of Specific Gases	94
8.3.1 H ₂ O	95
8.3.2 Temperature Measurements.	96
8.3.3 HCl	97
8.3.4 CO.	98
8.3.5 SO ₂	98
8.3.6 CO ₂ , C _x H _y , and Other Gases.	99
APPENDIX I. SPECTRAL CHARACTERISTICS OF OPTICAL ELEMENTS IN OPO	101
REFERENCES.	106

LIST OF FIGURES

<u>Fig. No.</u>		<u>Page</u>
Plate A	(Photograph) System at time of delivery	8
1	Tuning curve and bandwidth of 1.06 μm pumped LiNbO_3 parametric oscillator (Ref. 5)	11
2	Planned design of parametric system as followed at the start of the program	13
3	Optical system arrangement at end of program	16
4	Laser rod with integrated acoustic Q-switch (Ref. 6)	18
5	Stable oscillator arrangement	19
6	Optical isolator with Faraday rotator and polarizers	22
7	Interaction region between beam and crystal in the stable resonator	28
8	Unstable resonator configuration used by Byer, et al. (Ref. 13)	29
9	Unstable resonator arrangement developed by Westinghouse	31
10	Unstable resonator arrangement with separate outputs for parametric oscillator and amplifier	32
11	Radial profiles of beam intensity: (a) with arrangement of Fig. 8 (from polaroid picture), (b) from arrangement of Fig. 9	34
12	Nearly unstable resonator of the final system arrangement	36
13	Radial intensity profile of beam obtained from resonators of Fig. 12	38
14	(a) Resonator arrangement producing pulses of 175 nsec duration, (b) pulse-time profile	39
15	Pulse-time profile of final pump chain	40
16	Detail design of parametric oscillator	44

LIST OF FIGURES (cont'd)

<u>Fig. No.</u>		<u>Page</u>
17	Calibrated tuning curves for angles of crystal and grating in OPO	54
18	LiNbO_3 damage threshold as a function of temperature	57
19	Oscillation thresholds in the tuning range with a 4.2 mm beam for various crystals	59
20	Oscillation thresholds in the tuning range with a 6 mm beam for various crystals	61
21	Transmittance of an LiNbO_3 (Crystal Technology Corp.) crystal in the idler range	65
22	Transmittance of an LiNbO_3 (Bell Telephone Laboratories) crystal in the UV, visible, and IR range from Ref. 14).	65
23	Parametric pulse energies for increasing drive by the pump chain for several tuning points. Dashed curves were taken for operation with etalon. Percentage data refer to fraction of idler energy of total output.	72
24	Signal and pump recombiner, M_8 from curve trace received from manufacturer (UVIRA).	102
25	OPO pump beam input coupler, M_9 , reproduced from curve trace received from manufacturer (UVIRA).	103
26	OPO output mirror, M_{10} , reproduced from curve trace received from manufacturer (UVIRA).	104
27	Etalon for OPO, E_2 , reproduced from curve trace received from manufacturer (Airtron).	105

LIST OF TABLES

<u>Table No.</u>		<u>Page</u>
I	Pulse Energies from Oscillator at 1100 v and Amplifier of Varying Voltage	41
II	Accuracy Requirements for Angle Control and Digital Display	52
III	Record of LiNbO ₃ Crystals Acquired	60
IV	Effect of Beam Diameter on Double Pass Oscillation Threshold	64
V	Relative Values of Signal and Idler Energies	71
VI	Oscillation Thresholds and Slope Efficiencies for Various Tuning Points	74
VII	Cross Section and Energy Data of OPO System Application to Various Gases	100

PARAMETRIC INFRARED TUNABLE LASER SYSTEM

M. Garbuny, T. Henningsen and J. R. Sutter
Westinghouse R&D Center
Pittsburgh, Pennsylvania 15235

ABSTRACT

By probing vibrational-rotational resonance absorption, infrared tunable lasers are able to detect and measure remotely the densities of pollutant, poisonous, or trace atmospheric gases. After the initial demonstration of this method at relatively small ranges at Westinghouse, a group at Stanford University developed a parametric tunable laser system of pulse energies high enough to promise such determinations at ranges of several kilometers with range and depth information. This is the final report on work under a contract in which Westinghouse undertook to utilize Stanford's results in the further development and construction of such a system for delivery to NASA Langley Research Center. The system operates with a YAG:Nd laser oscillator-amplifier chain which pumps a parametric tunable frequency converter. Its design diverged in several important respects from its prototype at Stanford University. The report describes the applied research and development work undertaken. Functions and design considerations of the various optical components are discussed in detail. Supply and quality of materials, especially crystals in a relatively new state of the art, turned out to be the main limitations to the performance of the system. As desirable, but not necessarily achievable, objectives, efforts were directed towards the generation of pulses with about 50 mJ total energy, tunable from 1.4 to 4.2 μm at linewidths of 0.03-0.1 cm^{-1} . The completed system produced pulse energies of up to 30 mJ. The output is tunable from 1.5 to 3.6 μm at linewidths of 0.2-0.5 cm^{-1} (FWHM), although the limits of the tuning range and the narrower linewidths can be obtained only at some decrease of output energy. A simple replacement of the nonlinear crystals presently in the parametric converter by samples of the higher quality already previously demonstrated is expected to improve the performance to a level closely approaching the original objectives. The system was delivered to NASA-Langley in February 1980.

1. INTRODUCTION

The laser provides a nearly ideal tool for probing the atmosphere, remotely and in real time, with respect to certain physical and chemical properties. The narrow frequency width and beam divergence of laser radiation, emitted in pulses of nanoseconds, or less, duration, can direct large powers per unit frequency interval on sections of the atmosphere at well defined times and locations. If these properties of the laser are combined with tuning over a sufficiently wide frequency range, it is possible to excite molecular constituents selectively at their frequencies of resonance. As a result, the emergence of tunable lasers has extended the range of field applications from such measurements as ranging, aerosol and smoke assessment, and anomometry to a much wider field. This includes (aside from remote temperature, humidity, and pressure determination, which are still in early development stages) the detection and measurement of pollutant and trace gas densities.

Pollution monitoring by laser radiation can be accomplished by one of three alternative basic processes:

- (1) Resonance Absorption
- (2) Resonance Fluorescence
- (3) Raman Scattering

A comparison of the three processes by Kildal and Byer¹ showed that the first of these offered by far the greatest sensitivity, i.e., it required the least laser power for otherwise equal conditions and performance. The optical configuration considered was double-ended in that the laser irradiated a detector through an absorbing medium. A single-ended arrangement which does not require the positioning of a receiver or a mirror at a distance beyond the absorbing medium was described and evaluated by Byer and Garbuny.² This arrangement, with laser and receiver more or less adjacent to each other, uses backscattering of the partially absorbed radiation either from the naturally present

atmospheric aerosol or from a suitable topographic target such as vegetation. The advantages of using the quasi-Mie scattering of aerosol result from the unfailing presence of the latter in the atmosphere and from the capability of that method to yield information on the range R and the thickness ΔR of the pollutant cloud from the time t of light propagation, i.e., from $R = ct/2$ and $\Delta R = c\Delta t/2$. The depth sampled by a beam of pulse length τ is $c\tau/2$. Obviously, accuracy of range information is bought at the expense of the backscattered signal intensity which is usually considerably smaller than that received from a topographic target at the same range. For example, the study² shows graphs which allow a direct comparison of the two methods for CO as pollutant. The minimum pulse energy (for which tuning off a resonance peak is required because CO is already present at about 0.3 ppm in the atmosphere) to detect a concentration of 20 ppm of 100 meter extension at 8.2 km is 10 mJ using a topographic target with 50% diffuse reflectivity, a 100 nsec pulse at 4.7 μm , and a telescope area of 1000 cm^2 . On the other hand, using the distributed Mie scattering of aerosol with a depth resolution of 15 meter, but the same conditions otherwise, a 10 mJ pulse detects a 20 ppm CO concentrations only up to 2.3 km. A range of 8 km requires 100 mJ. These detection limits are defined for $(S/N) = 1$ and a single pair of pulses on and off resonance.

The resonance spectra of most pollutant gases of interest lie either in the near infrared or in the ultraviolet regions, the former corresponding to vibrational-rotational transitions, the latter to electronic transitions often of such energy that the radiation is either absorbed or at least strongly scattered by the atmosphere. In a choice between the near infrared and ultraviolet regions for pollution monitoring by absorption, one has also to consider the availability and performance of the tunable sources as well as of the detectors. Up to a few years ago, the choice between wide-range tunable lasers was limited essentially to the parametric oscillator for the near infrared and the frequency doubled dye laser for the near ultraviolet region with a lower wavelength limit of about 300 nm. For the purpose of monitoring a large number of pollutant gases, the parametric oscillator was then the only choice, since

its already achieved spectral tuning range up to $3.6 \mu\text{m}$ covered fundamental or harmonic vibration resonance regions of the majority of such gases, whereas the limits of the ultraviolet sources excluded a majority of them. In recent years, the arrival of the excimer laser and of Raman mixing processes has extended the range of tunable ultraviolet sources to 200 nm, although atmospheric absorption and scattering limit to some extent the utilization of such extension. Because of this limitation, the infrared region retains its importance for remote pollution monitoring, even though the ultraviolet region allows the use (denied to the infrared) of photomultipliers, the radiation detectors of highest detectivity.

With the help of Prof. R. L. Byer of Stanford University, as consultant, we constructed in 1972 a parametric tunable laser system in which the tuning was achieved by temperature variation of a lithium niobate crystal (LiNbO_3). The instrument was initially used to demonstrate its capabilities for laser spectroscopy, notably its resolution, speed of frequency scanning, and spectral brightness. Although the output energies were only in the range of microjoules, the results were encouraging enough to proceed with the construction of an experimental pollution monitoring system. A parametric tunable laser, dedicated to remote monitoring, was built on the same platform with a receiver consisting of an eight-inch telescope, indium antimonide detector and simple signal processing circuitry. In a measurement, which represented the first of its kind (Henningsen, Garbuny and Byer³), the signal passing through a column of 20 cm thickness of atmospheric pressure carbon monoxide was backscattered from a topographic target at 107 meter distance. The rotational lines in the first overtone spectrum of CO were measured with $S/N = 27$ in (apparent) agreement with the value $S/N = 34$ predicted by the relations of the previous analytical work.²

Efforts at Stanford University (1973/1974) succeeded in growing LiNbO_3 crystal boules along the $[01.\overline{4}]$ axis which is close to the direction in which a laser beam from YAG:Nd at $1.06 \mu\text{m}$ can pump this material for parametric angle tuning (although the $[01.\overline{3}]$ axis is yet closer). Boule sizes in excess of 2 cm diameter and 12 cm length were obtained. A beam

from a YAG:Nd laser directly incident on the crystal was found to produce signal wavelengths from $1.4 \mu\text{m}$ to the degeneracy point at $2.1 \mu\text{m}$ and idler wavelengths from 2.1 to $4.4 \mu\text{m}$. This continuous tuning range from $1.4 \mu\text{m}$ to $4.4 \mu\text{m}$ is obtained by varying the angle between the optical axis, i.e., the $[00.1]$ crystal direction, and the beam from 49.5° to about 45° no exchange of optical parts such as cavity mirrors being required. The tuning range includes fundamental or overtone resonance frequencies of most molecular gases. For purposes of pollution measurements, the method of angle tuning has compelling advantages over temperature tuning with 90° phase match: (1) For molecular infrared spectra, the degeneracy point at $2.1 \mu\text{m}$ is a much better location than that of the temperature tuning method at $1.1 \mu\text{m}$; (2) The pump at $1.06 \mu\text{m}$ avoids the need for frequency doubling; (3) In contrast, the pump beam in the temperature tuning method is generated by frequency doubling, the infrared tuning range up to $3.5 \mu\text{m}$ can be bridged only by switching YAG:Nd pump lines and exchanging mirrors, and the frequencies of the Optical Parametric Oscillator (OPO) output lie far from degeneracy. In addition to a wider infrared tuning range, these features endow the angle tuning method with the potential for considerably larger output powers, a fact enhanced by the large size of the boules obtained in the $[01.\bar{4}]$ growth direction. In fact, the output energies of the angle tuned and the temperature tuned systems stand in the ratio of $1000:1$. Besides that, angle tuning is faster and requires fewer optical elements. All these advantages far outweigh the disadvantages of this method: (1) A wider bandwidth of the output frequencies (in part a consequence of their closeness to degeneracy) and (2) The difference ("walk-off") in the refraction angles which results for the signal and idler beams from the off-axis pump direction. However, the large energies of input and output in prospect compensate both drawbacks. Relatively large energy densities can be spread over large beam spot sizes, so that the diverging waves inside the crystal maintain good overlap and good resolution is obtained for intracavity frequency narrowing gratings or etalons.

By the end of 1974, the Stanford group had demonstrated the wide tuning range of $1.06 \mu\text{m}$ pumped LiNbO_3 , albeit at low powers.

Further developments of the pump source and the OPO cavity elements were still needed to realize the potential for output energies above 1 mJ with useful spectral resolution. Nevertheless, on the basis of the previous analysis² and the experimental demonstrations at Westinghouse,³ it was possible to predict a state of the art in pollution monitoring by the infrared parametric oscillator, with which gas densities could be measured at a range of 2 km by Mie backscatter and, of course, at much larger ranges by the use of topographic targets.

The results and expectations of this recent work conducted at Stanford University under contracts with NASA, NSF-RANN, and AEC, provided the incentive for negotiations between NASA and Westinghouse to further develop, engineer, and construct a deliverable parametric infrared tunable laser system, while "tracking" the ongoing development work at Stanford. Westinghouse submitted in 1974 a proposal in two parts. Part I proposed to apply the Stanford experience in growing [01.4] oriented LiNbO₃ crystals to industrial development and fabrication. Part II proposed the development of the tunable system itself. However, at that time, Crystal Technology had already adopted the Stanford technique and began to produce crystals of [01.4] orientation, and it further appeared that other suppliers of optical crystals might also try its production. On suggestion of NASA-Langley, Part II of the proposal was therefore resubmitted in January 1975 without reference to Part I, which was not pursued further.

The objectives of the proposed contract in 1975 included delivery to NASA-Langley of a system consisting of laser oscillator, laser amplifier, parametric tunable oscillator using [01.4] grown LiNbO₃, gas monitor cell, and all auxiliary equipment necessary for operating the system. The performance objectives included: (1) pulse energies of at least 250 mJ at 10 pps from the laser amplifier, (2) 25 to 70 mJ total parametric output per pulse, (3) tuning range from 1.5 to 4.0 μ m with one set of mirrors and at low powers from 4.0 to 4.5 μ m with another set of mirrors, and (4) a bandwidth of 0.03 cm^{-1} in TEM₀₀ mode. However, it was stressed that since there was no precedence for the performance of such a system, the objectives did not represent firm specifications.

Work began 17 March 1975. The completed system shown in plate A was delivered to NASA Langley in February 1980.

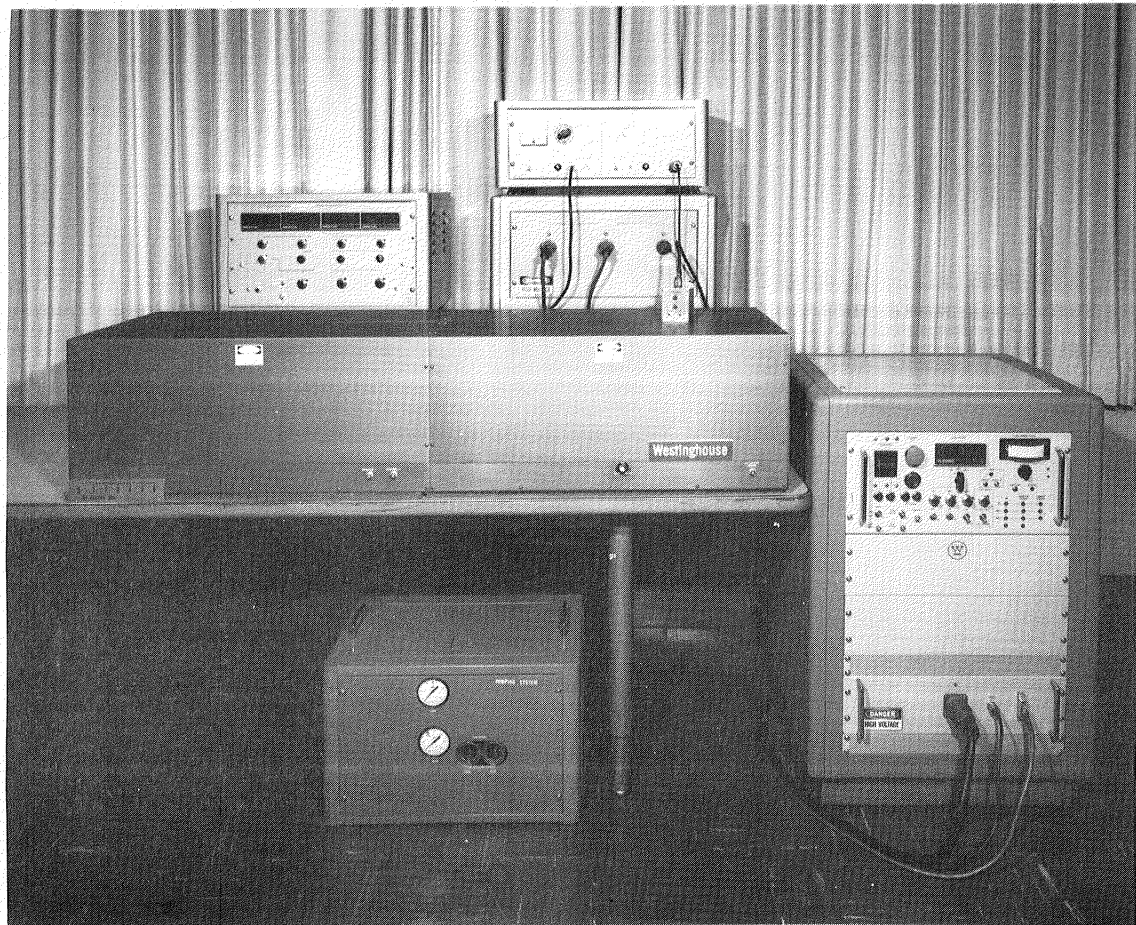


Plate A
(Photograph)
System at Time of Delivery

2. ALTERNATIVES OF SYSTEM CONSTRUCTION

This section will provide an overview of the parametric system as it was first planned and in the arrangement to which it had evolved at the end of the program.

2.1 Functions and Methods

The alternatives available for parametric tuning follow from the two basic equations (in simplest terms, the conservation laws of photon energy $\hbar\omega$ and photon momentum $\hbar\mathbf{k}$, respectively):

$$\omega_p = \omega_s + \omega_i \quad (1)$$

and

$$\bar{k}_p = \bar{k}_s + \bar{k}_i \quad (2)$$

or, for collinear propagation of the three beams, instead of Eq. (2)

$$\omega_p^n = \omega_s^n + \omega_i^n \quad (2a)$$

Here, ω_p is the (angular) frequency of the pump beam which, incident on a nonlinear crystal, couples power into a signal frequency ω_s and an idler frequency ω_i (by definition, $\omega_p > \omega_s \geq \omega_i$) and n_p , n_s , and n_i are the respective indices of refraction. The largest parametric conversion gain is achieved by placing the nonlinear crystal into a cavity which is doubly resonant with the signal and the idler beam. However, unstable operation and difficulty in maintaining the tuning range with the cavity, make an operation necessary in which the cavity is singly resonant either with the signal or the idler.

At a fixed pump frequency ω_p , the refraction indices determine ω_s and ω_i , within a certain bandwidth, by Eqs. (1) and (2) or (2a). At

fixed ω_p , tuning is accomplished by varying the indices either by temperature or by the angle with which the pump beam is incident on the crystal. The bandwidth is correlated to the effect which a deviation from Eqs. (1) to (2a) has on the gain. Equation (2) or (2a) represents a condition of phase match. For a fixed pump frequency ω_p and given values n_p , n_s , n_i , Eqs. (1) and (2) or (2a) determine uniquely ω_s and ω_i for the condition that the three waves maintain exact phase coherence as they propagate through the crystal. Waves generated at frequencies $\omega_s + \Delta\omega_s$ and $\omega_i + \Delta\omega_i$ lose their mutual phase relationship gradually at distances which decrease with increasing deviation $\Delta\omega$. This has the effect of reducing the gain $G(L)$ over a path length L according to the equation⁴

$$G(L) = \Gamma^2 L^2 \frac{\sinh^2 [\Gamma^2 - (\Delta k/2)]^{1/2} L}{[\Gamma^2 - (\Delta k/2)] L^2} . \quad (3)$$

Here the gain parameter Γ is given by

$$\Gamma^2 = \frac{2\omega_i \omega_s d^2 I_p}{n_i^2 n_s^2 n_p^2 c^3 \epsilon_0} \quad (4)$$

where d is the operative coefficient of the nonlinear polarizability tensor, ϵ_0 is the permittivity of vacuum, and I_p is the pump intensity or fluence. Furthermore, Δk represents the mismatch by which Eq. (2) fails to be fulfilled. From Eq. (3) one can obtain a characteristic gain band width Δk_h , at which the gain is half that at phase match.

The bandwidth of a beam emerging from a parametric cavity can always be reduced by filters such as etalons, albeit, at a sacrifice of the output power. However, (ideally lossless) methods of bandwidth narrowing exist for the resonating beam, if applied inside the cavity and, preferably, without perturbing the nonresonating beam. In essence these methods employ frequency filters which narrow the gain profile below that determined by Eq. (3). Examples are (1) intracavity etalons with a finesse which is high for the resonating wave, but very small for the nonresonating beam, and (2) intracavity beam splitters which selectively divert the resonating beam towards frequency narrowing elements

such as gratings or etalons, or both. If such means are employed, the nonresonating frequency, too, can be narrowed, according to Eq. (1), by reducing the frequency width of the pump beam. All these considerations are pertinent for the design particularly of angle tuned parametric systems.

2.2 Features of Angle Tuning [01.4] Grown LiNbO₃

At the start of this program, Professor Byer's group at Stanford University had already reported the first demonstration of angle tuning over a wide spectral range using a 1.06 μm beam of 0.780 mm spot size on [01.4] grown LiNbO₃. In summary, they reported⁵ the following results:

Near degeneracy at 1.9 μm , the threshold of parametric oscillation was 4 mJ, corresponding to 0.21 J/cm². Output energies of more than 1 mJ at 20 nsec, conversion efficiencies of 15%, and the use of pump energies up to 20 mJ were cited for parametric cavities terminated by high reflection mirrors. Figure 1 shows the predicted and measured

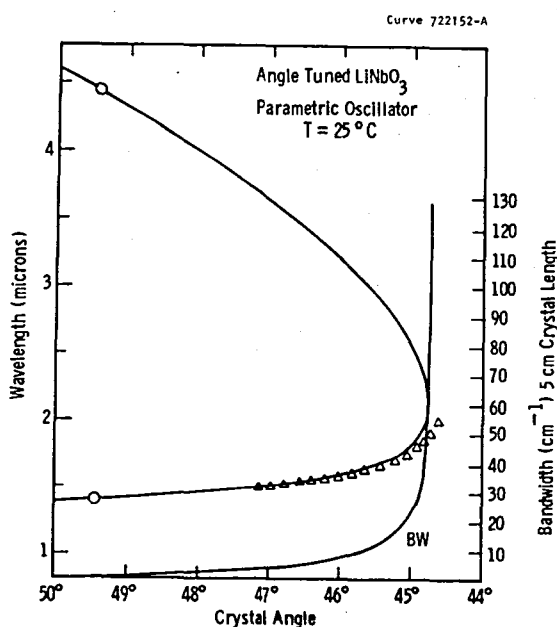


Fig. 1. Tuning curve and bandwidth of 1.06 μm pumped LiNbO₃ parametric oscillator (Ref. 5).

dependence of wavelength on angle over the continuous tuning range from 1.4 to 4.4 μm (the circled point was taken with a different output mirror). Figure 1 also shows the predicted dependence of bandwidth on tuning angle; actually measured bandwidths varied from 3 cm^{-1} near $1.5 \mu\text{m}$ to 23 cm^{-1} near degeneracy.

The Stanford experience demonstrated that [01.4] grown LiNbO_3 could be grown in relatively large sizes so that these experiments could be performed with a 50 mm long crystal of 15 mm diameter. The crystal had also displayed a damage threshold above 1 J/cm^2 so that one could expect, by extrapolation, that it could tolerate pump energies of 2 Joules.

Taken together, these results implied the feasibility of a high energy parametric converter tunable over a wavelength range in the near infrared from 1.4 to 4.4 μm . The Stanford group, therefore, turned at once to the design and development of such a system. Westinghouse, under the contract with NASA-Langley, followed the group in the major design features for the development and construction of a deliverable system.

2.3 Plans for the Design of the System

The new parametric tunable system differed from the older, temperature tuned arrangement in several respects. The laser pump had to deliver pulses of 250 mJ or more in TEM_{00} mode with beam diameters around 5 mm. This required pump amplifiers and means to prevent the unavoidable fraction of radiation, reflected backwards into the beam by intervening surfaces, from undergoing destructive amplification. The relatively large bandwidth of the parametric frequencies required cascading stages of tuning with increasing resolution and the accompanying need for electronic control, digital display, and provisions for access to a computer. As deliverable equipment which, in operation, had to be moved around, the system required a high structural stability against deformation by fractions of a wavelength. Taken alone, these requirements were not new, but they were novel in combination. A particularly vexing problem was the fact that reliance had to be placed on the optical quality and damage threshold of crystals, coatings, and optical components acquired in small quantities from outside suppliers.

An assembly view of the system, as it was originally planned, is shown in Fig. 2 without power supplies, electronic control and other auxiliary equipment. In the main, the optical arrangement consists

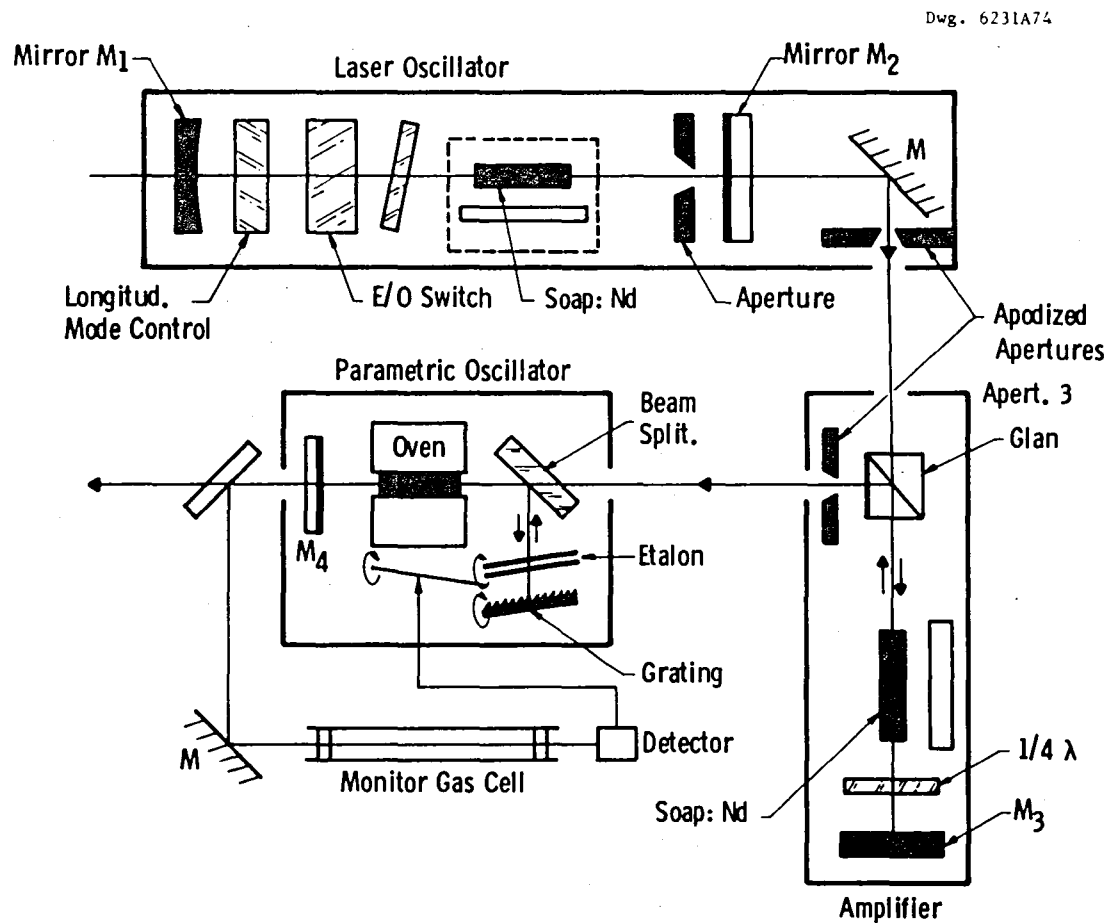


Fig. 2. Planned design of parametric system as followed at the start of the program.

of three parts, viz., the laser oscillator, an amplifier, and the parametric oscillator. Contained in a stable resonator, the laser produces

Q-switched pulses of 5-10 mJ energy at 1.06 μm in a TEM_{00} mode beam. End mirrors and diffraction limited beam divergence form a spot size of 4-6 mm at the entrance of the amplifier section. It was planned to amplify the pulse energy typically to 250 mJ. Subsequently, the pump beam enters a parametric cavity containing three tuning elements, viz., the nonlinear crystal for angle tuning, a grating for narrowing the frequency width to the order of one cm^{-1} , and a etalon to further reduce the bandwidth by a factor of 6-10. Assuming a parametric gain efficiency of 20%, 250 mJ of pump energy should then produce 50 mJ of combined signal and idler energy.

At the end of the contract, the final optical arrangement had evolved to that shown in Fig. 3. The difference between the design concepts in the two figures is, in fact, larger than it might appear. The laser oscillator operates, not with a stable resonator, but with a hybrid between a stable and an unstable resonator. It produces a pulse energy of typically 120 mJ, thus assuming a much larger share in the energy buildup. Therefore, amplification to the required level of energy is possible in a single stage, rather than in double-pass as shown in Fig. 2. Typical output energies of the amplifier are now 300 mJ, but 360 mJ have been demonstrated. These high energies require isolation of the reflected radiation by the Faraday rotator indicated in Fig. 3. Although the available pump energy exceeds the original objective considerably, it was not possible, or rather not prudent to try, to reach the objective of parametric output energies in the range of 25-75 mJ. As described in detail later, the state of the art in crystal growth of LiNbO_3 in industry falls short of what was achieved at Stanford University (and even by our single supplier initially) in quality and quality control. In particular, these industrial crystals (each at a price of about \$3,000) exhibit too high a threshold of energy density at which they begin to oscillate and too low and too unpredictable a threshold at which they are optically damaged. To operate at least 30% below the "average" energy density damage threshold one can exceed the oscillation threshold by only a small factor. Because of the exponential relationship between output energy and gain, one obtains then typically 20 mJ,

when the signal wave is tuned to 1.9 μm , and 10 mJ, when it is tuned to 1.5 μm . These values are not performance limits; to the extent to which one is willing to risk a higher probability of optical damage, one will penetrate into the range of output energies that constituted the original objective. A similar situation exists for the tuning range. For a fixed pump wavelength of 1.06 μm , one obtains according to Eq. (3) an idler wavelength of 3.61 μm for a signal at 1.5 μm , and 3.94 μm for a signal at 1.45 μm . However, spectral analysis of our crystals showed the beginning of an absorption edge near 3.6 μm , and operation at a signal wavelength of 1.4 μm (idler at 3.91 μm) damaged the crystal severely on one occasion, possibly due to the effect of idler absorption. The crystals grown at Stanford University did not have this limitation,

Figure 3 also shows provisions for the use of an optical parametric amplifier (OPA). For such use, part of the pump power can be diverted to energize the amplifier. However, because of the present difficulty of obtaining LiNbO_3 crystals of sufficient quality, the system is delivered without that amplifier crystal.

The development of each of the subsystems are described in the succeeding section.

Dwg. 7719A75

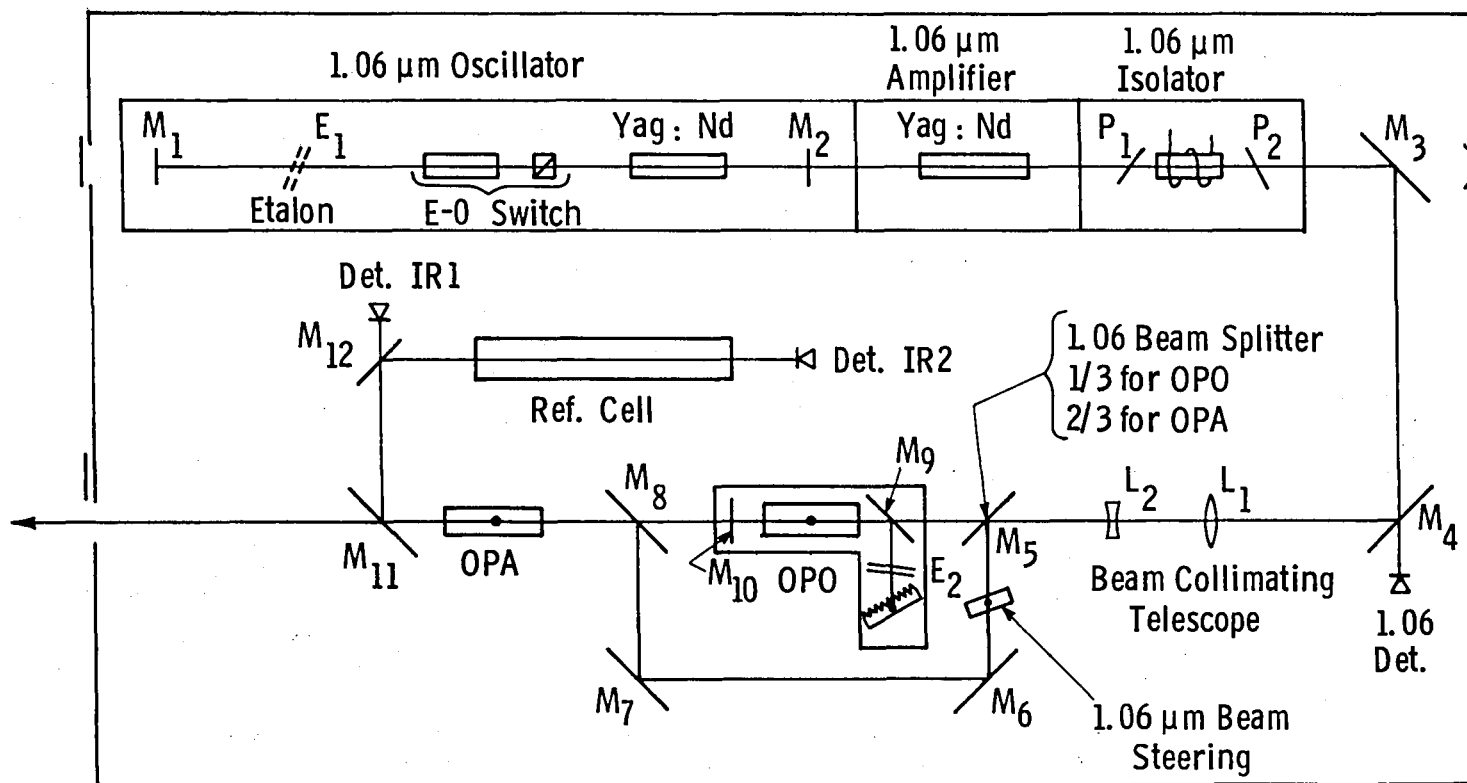


Fig. 3. Optical system arrangement at end of program.

3. DEVELOPMENT OF THE LASER OSCILLATOR-AMPLIFIER CHAIN

3.1 Initial Approach

The original plan for the laser oscillator design is embodied in the stable resonator arrangement shown on top of Fig. 2. The most important feature is the application of SOAP:Nd, i.e., $\text{Ca}_2\text{La}_8(\text{SiO}_4)_6\text{O}_2:\text{Nd}$, a laser material, first developed by the Westinghouse R&D Center. Compared with YAG:Nd, SOAP:Nd laser crystals have one fifth of the gain. Thus, in Q-switching, this material can be pumped to a correspondingly larger energy content before the onset of superfluorescence, i.e., the Q-switch hold-off allows 5 fold larger pulse energies. After the start of Q-switching, the lower gain prolongs the pulse duration by a factor 5 beyond that of YAG:Nd. Alternatively, the lower gain can be used for improved mode control, an option of particular interest for the parametric system. One method by which such mode control can be utilized is shown in Fig. 2. Q-switching is performed in two steps. Initially, the Q-switch is opened to an extent that gain is barely above threshold. This gain is first achieved by a mode of lowest order. By diverting part of this developing mode to a detector, full opening of the Q-switch can be timed to allow only one mode to develop, yet is sufficiently fast to prevent lossy dissipation of the stored energy. The lower rate at which the pulse builds up in SOAP:Nd is thus used to advantage.

An alternative to electrooptic Q-switching is control of beam passage by acoustooptic diffraction. Henningsen and Conroy⁶ combined the laser rod and acoustic Q-switch into a single unit by shaping the SOAP:Nd crystal near its end into a dorsal fin-like side extension to which they attached an acoustic transducer (see Fig. 4). The end of the rod itself was ground into a truncated cone so that the flat end surface provided a sharply defined and automatically centered aperture, while the conical surface scattered, rather than absorbed, any radiation outside that limited by the aperture. There are several advantages to

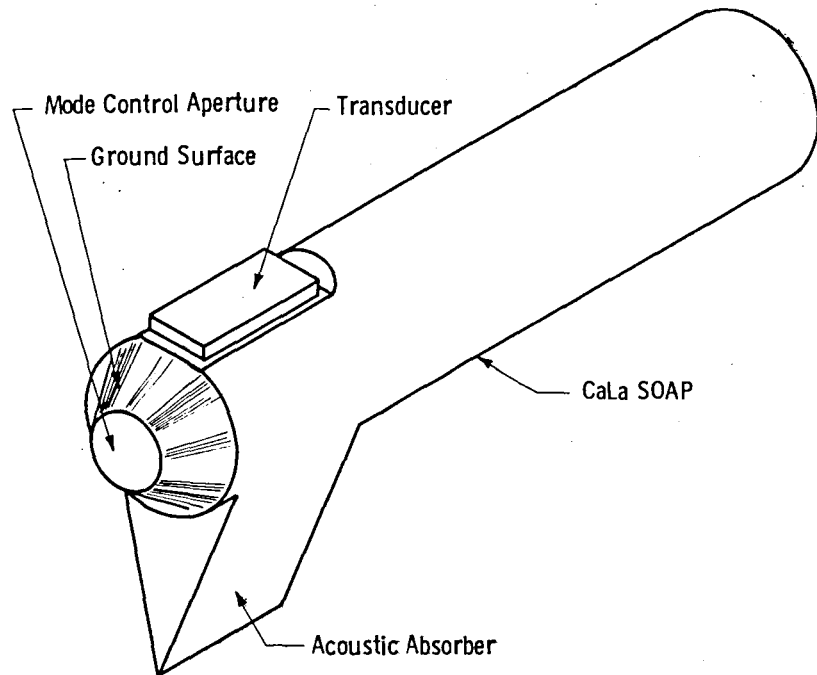


Fig. 4. Laser rod with integrated acoustic Q-switch (Ref. 6).

such an integral unit, viz., reduction of the number of reflecting surfaces by two, alignment stability, simplicity and lower cost. As an acoustooptic method, it shows a delay between the application of an electrical pulse and its effect on the beam via the propagating sound wave. The two-step Q-switching option is, therefore, not available for this combination.

3.2 Construction and Performance of the Stable SOAP:Nd Oscillator

The first laser oscillator built after the program had begun employed a flat 99.9% reflecting back mirror and a 65% reflecting 3 m output mirror (see Fig. 5). High mechanical and thermal stability of the optical path lengths was provided by three (3/4" dia.) invar rods to which all optical parts were connected by specially designed mounts. The mirrors, in particular, were supported by 1" dia. beryllium copper mounts.

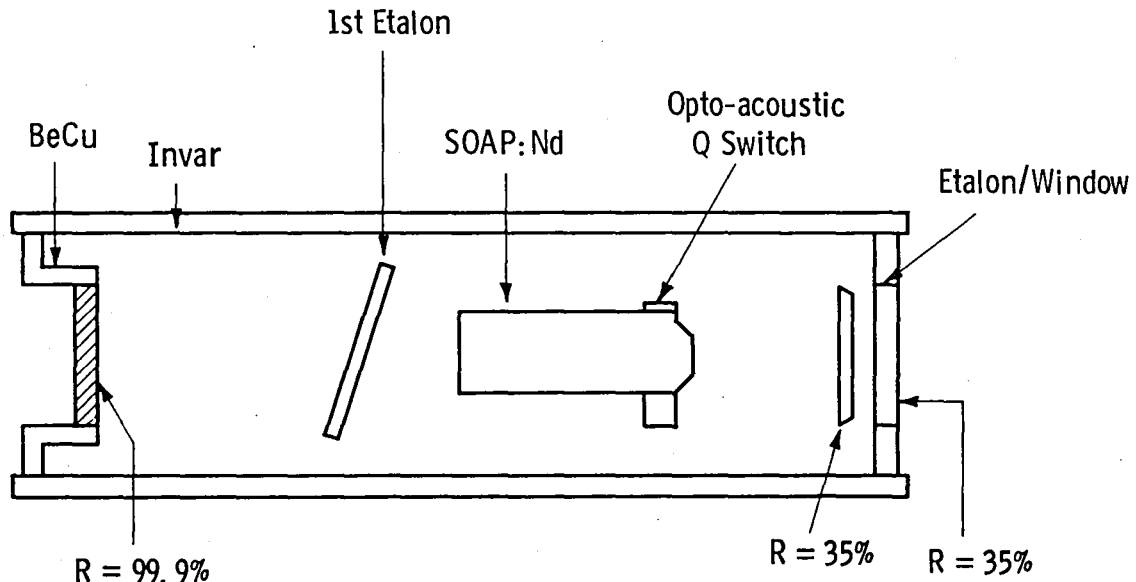


Fig. 5. Stable oscillator arrangement

which reentered the cavity to such a distance that the small thermal expansion of the invar rods was just compensated by that of the mounts.

Q-switching was performed acoustooptically, the switch forming a 4.5 mm long extension of the SOAP:Nd rod as described in the preceding section. Ideally, r.f. (40 MHz) power applied to the transducer maintains a light diffracting acoustic wave in the interaction space of beam and sound during the flashlamp pulse and then stops abruptly to allow passage of the Q-switched pulse. However, reflections of sound from the end and the walls have to be avoided since they intermittantly produce and then suppress a sound field entailing repeated Q-switched pulses. After a series of trials, sound reflections were practically eliminated by providing for the dorsal fin shape shown in Fig. 4 and an absorbing layer of indium amalgamate at its end.

The fluorescent bandwidth of SOAP:Nd of about 30 cm^{-1} is narrowed to $1-3 \text{ cm}^{-1}$ during lasing, depending on the excess of flashlamp

power over the gain threshold. Introduction of a tilted etalon reduced the bandwidth further to as little as 0.03 cm^{-1} . Note that the term "bandwidth" does not imply a continuum of frequencies over a certain interval. Since a cavity of optical path length nL oscillates only in discrete longitudinal modes spaced in frequency apart by $(2nL)^{-1}$, a spectral profile of width $\Delta\nu$ consists of about $2nL\Delta\nu$ lines. In our stable oscillator, $nL = 60 \text{ cm}$ so that a bandwidth of 0.03 cm^{-1} implies the presence of about 4 lines. Because of the mode beating, which produces in time a statistically fluctuating intensity when less than 4-5 modes, but more than one are present, we allowed 4-5 modes to be present. This corresponds to a bandwidth of $0.03-0.04 \text{ cm}^{-1}$. On the other hand, the approach to single mode operation is technically difficult and not justified. The anticipated resolution of the OPO would present a lower limit of bandwidth anyway. It should be added that under certain conditions the FSR (Free Spectral Range) of the etalon was not sufficient to suppress more than one order so that a second line appeared. This could be avoided by the use of a second etalon. As shown in Fig. 5, the output mirror could be constructed as a reflection etalon which provides the required single-line operation.

The laser oscillator produced pulse energies in the range of 5-10 mJ, with spot sizes of about 1 mm. From measurements of the radial intensity distribution and beam divergence, it could be concluded that the laser operated in a TEM_{00} mode. As anticipated, the pulse duration was 50 nsec. Compared to YAG:Nd operation, which under the same conditions, yielded only 9 nsec, the longer pulse length was expected to increase the resolution of frequency selection in the parametric oscillator. It was also found later that the shorter pulse duration reduced severely the optical damage threshold of LiNbO_3 .

These results showed that SOAP:Nd represented an excellent material for laser operation, at least with rod sizes up to $1/8"$ diameter. Containing elements with minimum alignment requirements, the stable oscillator just described was capable of producing pulses of sufficient energy, beam quality, sharpness of frequency, and pulse duration.

3.3 Construction and Performance of the SOAP Amplifier Chain

With an output of 5-10 mJ in pulse energy delivered by the stable oscillator, an amplifier chain increasing that energy by a factor of 50-75 was needed so as to deliver at least 250 mJ to the OPO, after a number of losses, such as reflections and absorption by interposed optical components are accounted for. The choice of SOAP:Nd which had proven successful for the laser oscillator in terms of beam quality and pulse length, required the use of this material also for the amplifier. The SOAP:Nd laser frequency at 9424 cm^{-1} has too small a bandwidth to overlap and pump that of YAG:Nd at 9398 cm^{-1} . SOAP:Nd crystal growth had been developed at the Westinghouse R&D Center and continued under license at Lambda Airtron. Because of a five-fold smaller gain compared to YAG:Nd, it not only stretches the pulse length, but by the same factor increases the pulse energy attainable before the onset of superfluorescence.

3.3.1 Faraday Rotator

Despite the relatively low gain, it was necessary to isolate the amplifier chain from the oscillator optically by a Faraday rotator. In the absence of rotators or polarizers, the front mirror of a cavity forms other resonators with all succeeding mirrors aligned with the beam axis. In the arrangement shown in Fig. 2, even the small fraction of the beam incident on the front of the $\lambda/4$ waveplate and reflected from it through the amplifying rod will enter the oscillator cavity with sufficient power to interfere with mode control or possibly produce optical damage. The arrangement shown in Fig. 6 eliminates the $\lambda/4$ waveplate and provides complete isolation of the beam returning through the amplifier. The polarizers shown have (birefringent) multilayer dielectric coatings, although Glan prisms have also been used in this arrangement. The beam emerges from the oscillator polarized in the horizontal plane, passes through the horizontally oriented first polarizer, experiences a 45° rotation of its polarization in a Hoya Glass rod activated magnetically and continues through the second polarizer which is oriented at 45° to the horizontal plane. The beam now enters the first amplifier performing a double pass through the amplifier rod

Dwg. 7720A53

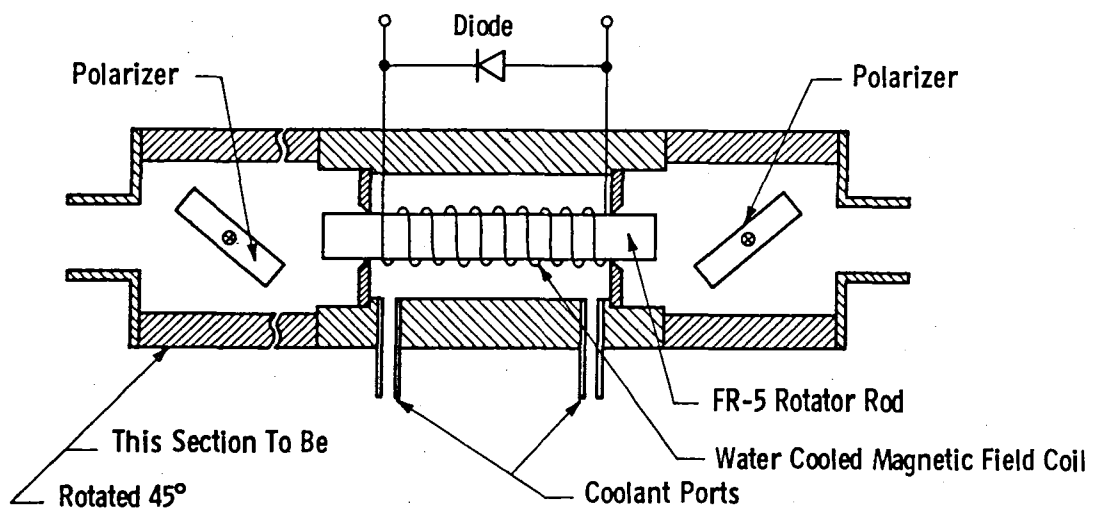


Fig. 6. Optical isolator with Faraday rotator and polarizers.

after reflection from the end mirror. Reentering the Faraday rotator, its polarization is now turned a further 45° into the vertical plane so that it is now reflected by the first polarizer into the second amplifier. The rotator consists of a 45 mm long, 10 mm diameter Hoya Glass rod around which two layers with 60 turns each of #22 (0.64 mm diameter) enameled copper wire were wound in direct contact and mounted in a flow of cooling water. With a Verdet's constant of $-0.0826 \text{ min}/\text{Oe-cm}$ at $1.06 \mu\text{m}$, rotation of the polarization by 45° requires a current of about 220 ampere in this solenoid, producing a field of 8,200 oersted. The design of the rotator and its operation without undue temperature increase and power demand owes its feasibility to the low duty cycle (0.1%) of the laser pulse generation so that a relatively small transistor

power supply can deliver a constant current for durations of about 100 μ sec overlapping the Q-switch pulse. An interlock circuit prevents Q-switching if the rotator current pulse does not appear at the preset time so as to prevent optical damage.

3.3.2 Test Procedures

The progress of the amplifier chain development was monitored by tests that, too, underwent a series of refinements and improvements:

(1) Pulse Energy. Measurements were performed with thermopiles and pyroelectric detectors. Calibration of these detectors was traced to a National Bureau of Standards pyroelectric detector obtained from their Electromagnetic Division.

(2) Beam Quality. The testing techniques used here gradually improved spatial resolution and accuracy of intensity distribution measurement in the following order:

(a) Paper Tests (Polaroid black paper) yield an approximate measure of the spot size and shape, thus are always useful for quick inspection of the beam spot appearance. However, details of the intensity distribution cannot be seen because of a nonlinear response to the flux density.

(b) Far-field Measurements reveal the existence of multiple transverse modes. Useful even with paper detection, they must be applied throughout the development work.

(c) Pinhole Probing of the spot pattern shows the radial intensity distribution with a resolution limited by scattering or the pinhole diameter, but it also shows the wings of that distribution. The process is slow, and the pattern may change during the measurement.

(d) Reticon Scanning of a 64 diode element array displays the radial intensity distribution with a resolution and speed (100 kHz) superior to pinhole probing. However, the fixed pattern noise (non-uniformity of response from element to element) was for the 1.06 μ m radiation pulses considerably larger than the 2-3% specified.

(e) An Infrared Vidicon with TV rate display was obtained from Hamamatsu Company. The system displays a two-dimensional image of

the infrared beam spot. It also can read out the radial intensity distribution of any selected segment. The two-dimensional scanning coverage and resolution in space (and time) are features far superior to the capabilities of methods (a) to (d). Only with this system could localized intensity spikes be detected which initiate optical damage in components following the amplifier.

(3) Frequency Conversion Capability. As soon as possible, the pump beams were tested on OPO cavities,

3.4 Material Quality as Barrier Problem of Performance

In the design of the tunable laser system, certain lower limits for the performance of critical component materials had been assumed. These assumptions were based on suppliers' specifications or past experience with the materials, or both.

In the tests accompanying the development, however, it was found that most optical materials, especially those produced in small quantities, with the state of the art just established fell far short of the manufacturer's specifications or of the performance proven by earlier batches.

The first example of this encountered in the program was the vulnerability to optical damage of the polarizers used in the arrangement shown in Fig. 6. A set of polarizers had been obtained from both Spectra Physics and Coherent Radiation with damage threshold specifications of at least 5 J/cm^2 . Samples received by other laboratories a year earlier were, in fact, reported to have even higher thresholds. However, in our tests begun in May 1976, damage was found to occur between 0.2 and 1.0 J/cm^2 . In some cases, coating cracks developed spontaneously on the shelf. Measures such as expansion of the beam were insufficient to get around this problem. Meanwhile film type polarizers were ordered from CVI, which had just recently delivered samples with a satisfactory damage behavior to another group at Westinghouse. As a standby alternative, we also ordered a set of calcite polarizers from INRAD. Both of these required a change in the design of mounting in the subsequent optical chain because of differences in sample thickness and beam angles.

Thus it was not until November 1976 that the problem was solved with CVI polarizers. The calcite polarizers, except for some beam distortion by one of the prisms, also worked satisfactorily, but because of unavoidable reflection losses on the prism surfaces they reduce the output energy by 50% in double pass operation.

An even larger problem was the optical quality of the SOAP:Nd rods in the diameter sizes needed for the amplifiers. Before SOAP:Nd crystal development was turned over by Westinghouse to Lambda Airtron under license, an optical quality had been reached which was satisfactory for the applications originally intended, such as ranging, but these practical objectives did not include the requirement of single transverse mode operation. However, oscillators using 3 mm diameter SOAP:Nd rods generated perfect Gaussian beam profiles and, for the purpose of this project, had the advantage over YAG of five times longer pulse duration. For rods of larger diameter, tests of the refraction index uniformity by interferometry showed the need for careful selection. The option of finding crystals of sufficient quality appeared available to us in the case of SOAP:Nd since boules of 1/4" to 1/2" diameter had been saved from the crystal program. Actually, however, we expected to use crystals from Lamdba-Airtron which had entered into a contract with the government to perfect growth techniques of SOAP:Nd crystals. Before the start of the present work we had, in fact, already received a 1 1/2" long SOAP:Nd rod of very high quality from Lambda-Airtron for the purpose of damage testing.

When the amplifier development was well underway, it was found that the amplification of a Gaussian beam pulse to more than about 50 mJ required a high optical quality of SOAP:Nd. This was established by tests of the beam quality with reticons and videcons. The tests showed that the desired beam quality could be obtained with SOAP:Nd rods only to the extent to which they showed a nearly perfect interferometric pattern. However, none of the crystals at hand had areas larger than about 3/16" diameter with the needed pattern perfection. There is little doubt that SOAP:Nd can be grown over larger sizes with the quality it exhibited in the oscillator crystals, and it is even likely that the samples actually sent out, after the crystal growth work was completed,

fulfilled this condition. Unfortunately, Lambda-Airtron was unable to reproduce the original quality, which we had seen previously, in crystals of the required greater length; nor could they be counted on to deliver such crystals in the near future.

Under these constraints, the best of the SOAP:Nd crystal rods were selected and machined to the design specifications. When the beam from the oscillator, expanded in diameter to 4-6 mm, emerged from such an amplifier rod in single pass, its quality was still quite high, but deteriorated considerably in double pass and became even worse after the second amplifier. This progression was mirrored in the performance of the beam when it was tested in the parametric cavity. The beam from the first amplifier in single pass produced parametric conversion with an efficiency which was not far from the theoretically expected value. However, it proved useless to add further amplification stages since no gain in OPO output energy was obtained and angle tuning became limited to a rather small frequency interval.

These results demonstrated the need for a change from SOAP:Nd to YAG:Nd as an amplifier and, therefore, also as an oscillator medium. The alternative of improving crystal growth techniques of SOAP:Nd to the needed quality, while merited because of the longer gain buildup times and greater energy storage, appeared to require lead times beyond the scope of this project.

3.5 Construction and Performance of the YAG:Nd System with Unstable Resonator

In response to the terms of this contract, we kept in close touch with the Applied Physics Department of Stanford University and incorporated, wherever applicable, advances in their parametric work which predated our program by more than a year. This was possible with the help of Prof. R. L. Byer who served as a consultant to Westinghouse.

At the time when we had reached an impasse with the supply of suitable SOAP:Nd crystals and thus had to turn to YAG:Nd, Byer's group had itself undertaken a major design change of their parametric system.

Their YAG:Nd based oscillator-amplifier chain had grown to unwieldy length and complexity. The small pulse energy produced by the oscillator had to be built up in rather small steps by a series of amplifiers with two or more Faraday isolators between them (a consequence, of course, of the limited energy holding capacity of YAG:Nd). However, the problem could be solved by replacing the stable oscillator by an unstable resonator, a feature first applied to lasers by Stanford's A. E. Siegman⁷ in 1964.

The unstable resonator abandons the condition that ray traces and, except for a scalar factor of attenuation or amplification, field amplitudes $U(x,y,z)$ repeat themselves after each round trip between the mirrors. For mirror radii R_1 and R_2 and cavity length L , unstable operation thus lies outside the stable resonator condition⁸

$$0 \leq \left(1 - \frac{L}{R_1}\right) \left(1 - \frac{L}{R_2}\right) \leq 1 \quad . \quad (5)$$

In high energy laser cavities, a complicating factor is presented by the lensing effect of the laser medium as its index changes under the influence of heating by the flash lamps. This lensing effect can be characterized by a focal length f which for YAG:Nd can be determined from the electric input power P_E to the flashlamps by the empirical relation⁹

$$\frac{d\left(\frac{1}{f}\right)}{dP_E} = 1.0 \cdot 10^{-3} \text{ W}^{-1} \text{ m}^{-1} \quad . \quad (6)$$

Equation (6) has only order-of-magnitude significance because, first, the heating of the laser rod may change due to such variables as lamp aging and, second, the thermally induced focal length varies for polarized light rays incident at various polar coordinates (r, θ) on the face of the rod by as much as a factor 1.7 due to the anisotropy of the YAG:Nd crystal.⁹ Typically, for $P_E = 100$ watts, the rod will act like a positive lens of $f \approx 10$ meter, but the effect may be decisive if the resonator operation occurs near the limits of Eq. (5).

The factor which usually limits the oscillator power in stable resonators is a small interaction volume which the lowest order mode

assumes in the laser medium (see Fig. 7). In a cavity of length L , the beam waist is of the order of $(L\lambda)^{1/2}$ so that in a cylinder of radius r the ratio of mode volume to the volume of the medium near the beam waist is $\approx (L/\lambda)/(\pi r^2)$. Thus a YAG:Nd rod of 0.3 cm radius pumped inside a 60 cm long stable cavity yields only a few percent of its stored energy. On the other hand, an unstable resonator permits its lowest mode to diverge so that after a series of reflections all of the laser medium is filled by the mode volume. As a result, up to 250 mJ output could be obtained, an energy which the stable YAG:Nd chain could reach only with two or three amplifiers.

Dwg. 7720A50

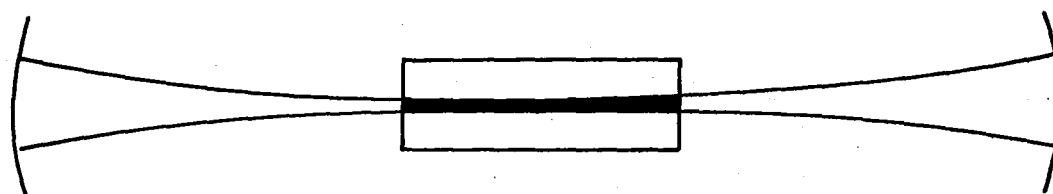


Fig. 7. Interaction region between beam and crystal in the stable resonator.

3.5.1 Diffractive Coupled Resonator

The unstable resonator configuration constructed by Byer's group has been analyzed by Siegman and Miller¹⁰ and is shown in Fig. 8. It

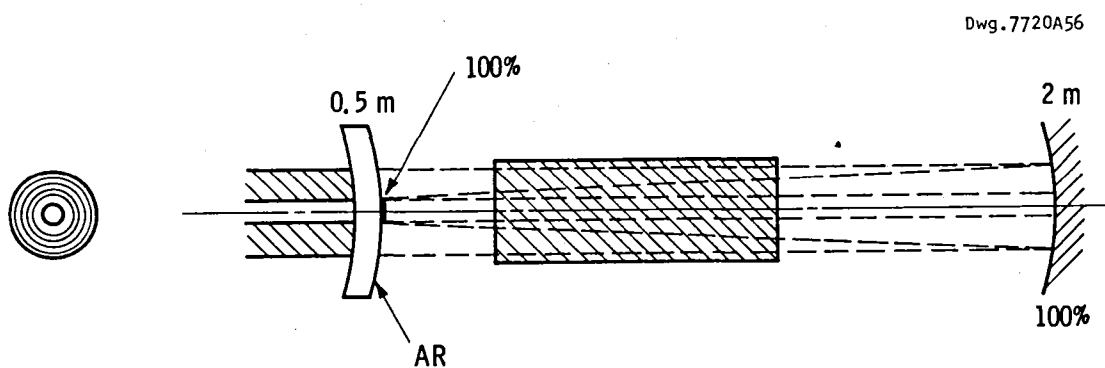


Fig. 8. Unstable resonator configuration used by Byer, et al. (Ref. 13).

consists of a concave fully reflecting 2m mirror facing a convex fully reflecting 0.5 m mirror of small size (1.8 mm diameter). The buildup of the lowest mode may be understood as that of an (almost stable) oscillator near the axis and that of an amplifier in the surrounding shell. The beam emerges around the small mirror, diffraction coupled into a collimated beam which is doughnut-shaped in the near field, but assumes in the far field approximately the diffraction pattern of a Gaussian radial intensity distribution. Because the far-field operation would place the OPO approximately 10 meters behind the oscillator, the

near field doughnut shaped beam was adopted. Although this beam performed in terms of conversion efficiency and bandwidth of the signal and idler as well as would have been expected from a Gaussian shape, it was responsible, in part, for a number of optical damage events afflicting the LiNbO_3 crystal. Byer's group, therefore, turned to far-field operation, but reduced the space requirements in one of two ways. The first method transformed the beam to about one tenth in diameter, so that it attained a far field pattern after one meter. The beam was then expanded again and passed through an apodized aperture. In the second method, the beam was folded back and forth between two mirrors for a total path length of ten meters. The second of these methods was found preferable since it avoided the type of optical component damage which the high power density of the first was apt to produce. However, our project was already in the final stage when these results were obtained.

Although these damage problems and their possible solution had not yet surfaced, our project proceeded by pursuing several options. The most direct way was to follow the Stanford approach. In that approach, the 1.8 mm diameter mirror (see Fig. 8) must be held to very accurate centering on the optical axis, as well as to a sharp edge definition, because of the diffraction output coupling requirement. In one type of construction, the mirror was evaporated as a "polka dot" on an AR coated meniscus shaped blank with 1 meter radius. Several of these mirrors were manufactured for us by Lambda Co., but all lacked adequate centering. In a second procedure, the 1.8 mm mirror was sectioned out from a 1 meter radius mirror blank by cavitron. The stem of this mirror is ground to a smaller diameter and inserted into a tight fitting center bore of a neutral meniscus of the type used for the polka dot.

3.5.2 Transmission Coupled Unstable Resonator

Another unstable resonator arrangement, which is based on a design developed at Westinghouse, is shown in Fig. 9. The cavity consists of a convex highly reflecting 1 meter radius mirror facing a concave 35% reflecting 2 meter radius mirror. The operation of this resonator is quite similar to that shown in Fig. 8 in that it encourages

Dwg. 7720A48

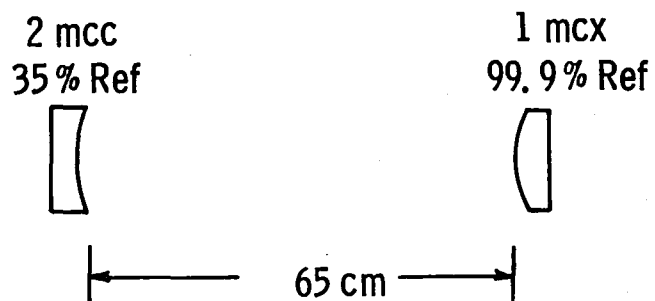


Fig. 9. Unstable resonator arrangement developed by Westinghouse.

the buildup of oscillation near the axis, the beam diverging so as to utilize most of the crystal's stored energy and leaving the cavity to the outside partly by transmission, and partly by diffraction coupling. The design has the advantage of replacing the doughnut shaped spot by a distribution in which the radial distribution has a maximum in the center. Furthermore, the design avoids the stringent centering requirement of the small mirror arrangement. It does lack the transverse mode control presented by the small mirror but without a noticeably deteriorating effect on the beam quality. Tests by the far field pattern and by beat frequency generation failed to reveal the existence of multiple transverse modes.

3.5.3 Two-Mirror Output Resonator

A hybrid of the two unstable resonator arrangements described is shown in Fig. 10. It uses the polka dot mirror in combination with

Dwg. 7720A49

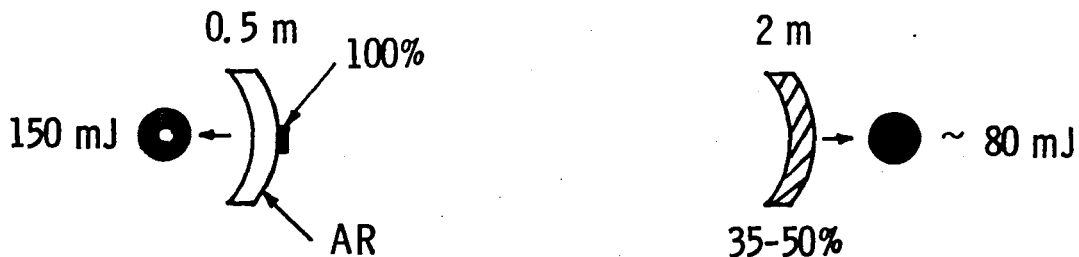


Fig. 10. Unstable resonator arrangement with separate outputs for parametric oscillator and amplifier.

the concave 35% reflecting mirror, with a doughnut shaped beam output of about 150 mJ from the former and an approximately Gaussian output of about 80 mJ from the latter. This hybrid arrangement was studied by us, and tried by the Stanford group, with the thought of (1) using the full beam (of which single transverse mode behavior is presumably assured by the 1.8 mm mirror) for the parametric oscillator; and (2) superposing the doughnut shaped beam on the output of the OPO as input for a parametric amplifier which was thought to tolerate that beam shape better than the parametric oscillator. However, both groups abandoned the design, although for different reasons: the Stanford group, because it was at that time satisfied with the doughnut beam and saw no reason to

divide the resonator power; the Westinghouse group, because of concern about pattern interaction resulting in optical damage to components.

3.5.4 Mode Structure and Radiation Damage

Even the best pattern obtainable with the 1.8 mm mirror exhibited unavoidably the doughnut shaped spot. Figure 11a shows a typical beam profile obtained with that type of resonator. The experience gained with SOAP:Nd generated beams had indicated that loss of efficiency in amplification and parametric conversion, as well as likelihood of optical damage, increased to the extent to which deviations from a Gaussian radial profile became more pronounced. In particular, the probability of optical damage was found, not surprisingly, to increase for patterns exhibiting sharp peaks or spikes. Presumably, a steep gradient of the flux density, produces stress concentrations through the resulting temperature or electric field gradients which are more destructive than a more uniform distribution of the peak intensity. A similar destructive role is probably played by shape variations of the intensity with time, $\delta I/\delta t$, a process favored by short pulse times. On the other hand, the inefficiency of amplification and parametric conversion is apparently caused by spatial index variations and a resulting phase mismatch over the mode volume. Unlike the SOAP:Nd beam after double pass, the doughnut shaped beam, which is considered to be a single transverse high order mode, has a radially symmetric profile. One could expect therefore the good efficiency of amplification and frequency conversion from such a resonator which was in fact later demonstrated. One could also expect that, unless the small mirror was perfectly aligned, and remained perfectly aligned, the resulting spikes in the pattern would ultimately contribute to optical damage. Following initial experimentation with the doughnut shaped beam, we therefore concentrated on the development of resonator arrangements of the type shown in Fig. 9. As mentioned before, the Stanford group finally circumvented the doughnut shape problem by far-field operation. As it turned out, we could not have used this approach, because of time limitations and because either of the two alternatives of that operation require, over long dimensions, a structural stability which was not easily reconciled with the requirements of an easily transportable device.

3.5.5 Optimal Mirror Dimensions

The radial beam profile of the mirror arrangement shown in Fig. 9 is reproduced in Fig. 11b. From the start, energy delivery was

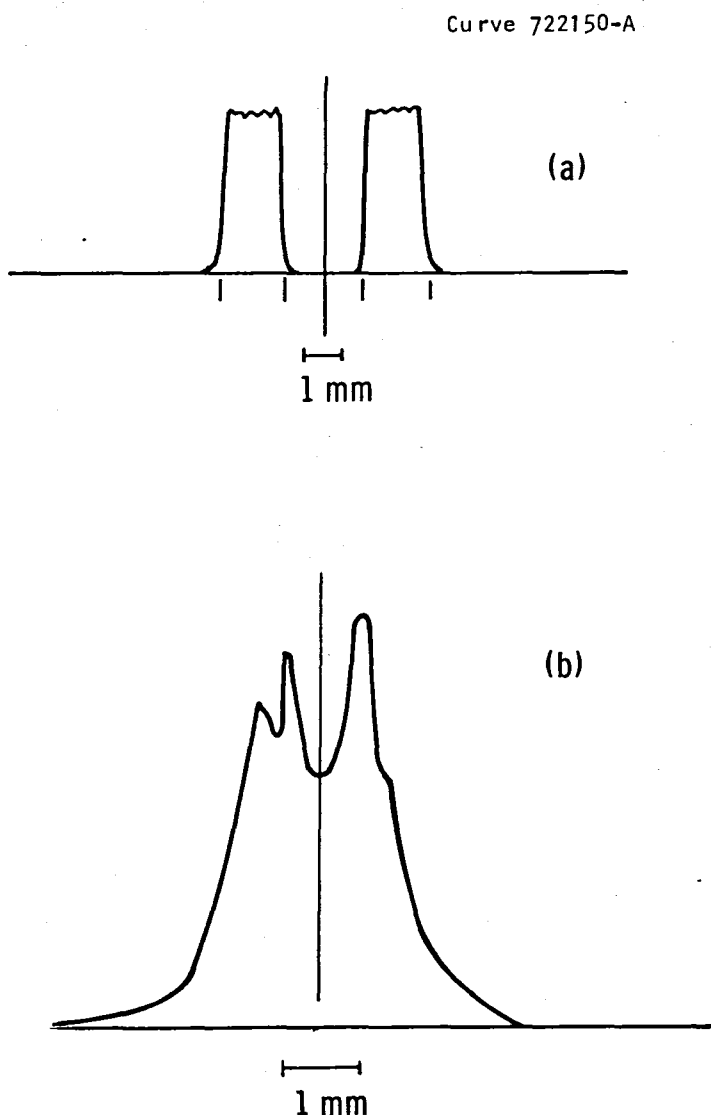


Fig. 11. Radial profiles of beam intensity: (a) with arrangement of Fig. 8 (from polaroid picture); (b) from arrangement of Fig. 9.

adequate. A combination of unstable resonator and single amplifier (7 mm diameter and 75 mm length) could produce pulse energies well in excess of 300 mJ. However, the output was held to a maximum of 330 mJ as a

safeguard against possible radiation damage in the amplifier YAG:Nd rod. During the duration of this project, no YAG damage was in fact produced. We had also acquired a larger amplifier rod (8.5 mm diameter and 85 mm length), but when tested interferometrically, it was of substantially lower optical quality than the 1/4" diameter rods of YAG:Nd. Because of the satisfactory energy delivery of the 1/4 diameter rod and the questionable quality of the larger amplifier, the latter remained unused.

As experimentation with the parametric system progressed, certain changes in the dimensions of the resonator shown in Fig. 9 became necessary. First, mirrors of different curvatures were tried so as to arrive at a radial beam profile that remained as free of spikes or peaks as possible along the propagation path. The main concern was occasional optical damage of the lithium niobate crystal of the parametric oscillator. In theory, such damage cannot occur, if the peak intensity of the beam remains below the specified damage threshold of the LiNbO_3 crystal. In practice, damage thresholds vary considerably and unpredictably and, again, large spatial or time variations of beam intensities may be more important for the damage mechanism than the peak intensity. Because of the statistical distribution (over a small number of samples) of damage thresholds and damage occurrences, it required here, as well as at Stanford, relatively long times of operation before any particular cause of damage was identified for a multiplicity of damage events. However, by varying the curvatures and spacing of the mirrors, the previously mentioned conjectures regarding the damage mechanisms were found to be consistent with experiment. Given a certain LiNbO_3 crystal quality and a correspondingly adjusted fixed pump pulse energy, the probability of damage is smallest, if (1) the radial intensity profile of the beam is as smooth as possible, and (2) the pulse duration is made as long as is still compatible with efficiency and other limitations.

Following these objectives, the design of the transmission coupled resonator shown in Fig. 9 evolved to less unstable configurations until it reached the arrangement shown in Fig. 12. The cavity consists of a flat and a concave mirror spaced 109 cm apart. The stability criterion, Eq. (5), assumed here the form

$$0 \leq \left[1 - L \left(\frac{1}{R} + \frac{1}{f} \right) \right] \leq 1 \quad (7)$$

where R is the radius of the concave mirror and f is the focal length of thermal lensing in the rod (which enters twice into a round trip). In typical operation, the oscillator is pumped by discharging a $28 \mu F$ capacitor at 1,000 volt and 5 Hz through a flash lamp, corresponding to 84.7 watt average power. With f about 12 m from Eq. (6), $R = 2$ m, and an optical path length $L \approx 1.15$ m, the term in the square brackets of Eq. (7) is 0.33; hence the powered resonator is stable; for an operation with 1,500 volt at 10 Hz, it would be unstable. However, because of the uncertainties pertaining to thermal lensing and, in particular, to the error limits of Eq. (6), a clear distinction cannot be made, i.e., the operation is, at any rate, near the borderline.

The arrangement of Fig. 12 was nearly optimal in operation among all tested configurations involving only a resonator and an amplifier.

Dwg. 7720A51

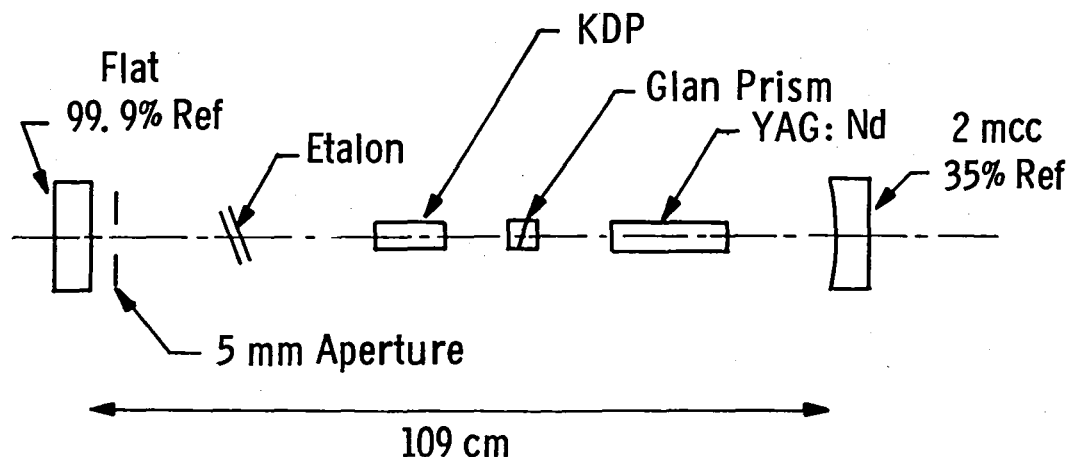


Fig. 12. Nearly unstable resonator of the final system arrangement.

It yielded pulse energies of 100-150 mJ and, after amplification, the range of 300-330 mJ which is considered safe with respect to radiation damage in the amplifier itself. In particular, it was nearly optimal with respect to the conditions (1) and (2) cited before. Radial spot profiles, as shown in Fig. 13, had a near-Gaussian shape without severe localized peaks.

The pulse length, defined here as the interval between the times when the pulse reaches half maximum on rise and fall, is proportional to the photon dwell time (or "lifetime") t_c in the cavity for equal population inversion conditions.⁸ The photon dwell time (i.e., the mean time which the photon spends in the cavity before its absorption on the inside or transmission to the outside) equals

$$t_c \approx \frac{2L}{c(r_1 r_2)} \quad (8)$$

for a stable cavity bounded by mirrors of reflectivity r_1 and r_2 , provided absorption and transmission of these mirrors represent all the losses encountered in a round trip through the cavity. In an unstable cavity of the polka dot type (see Fig. 8), however, t_c is the average time the photon is kept in the cavity before it is diffracted to the outside. With about two round trips (as determined by the cavity dimensions), a cavity of 60 cm length allows a dwell time of ≈ 8 nsec. The population inversion conditions can be characterized by the ratio n_i/n_t of the initial inverted population, n_i , at a given operating point before the Q-switch to that at threshold, n_t . Analysis of the process in four-level lasers shows⁸ that the pulse power reaches its peak when the inverted population has been depleted to the threshold value n_t . For $n_i \gg n_t$, stimulated emission builds up to the peak in a time shorter than t_c . Each stimulated photon reduces the inverted population by two. Therefore, at the peak, the number of photons in the cavity is nearly $1/2(n_i - n_t)$. This population then decays with the photon dwell time t_c to a value below n_t . As a result, the pulse width, under conditions of high initial inversion, is only a little larger than t_c . For the unstable cavity of Fig. 8, then the pulse duration is in the order of 10 nsec.

In the development of transmission coupled resonators for optimal pulse durations, the theory could serve only as a loose guide because practical conditions introduce variations from the simple assumptions which are too complex for analytical consideration. Examples for resonator configurations with which various pulse lengths were obtained are shown in Figs. 12 and 14. The arrangement of Fig. 12 using at first an optical path length $L=65$ cm between a flat mirror with $r_1=0.999$ and a

Curve 722149-A

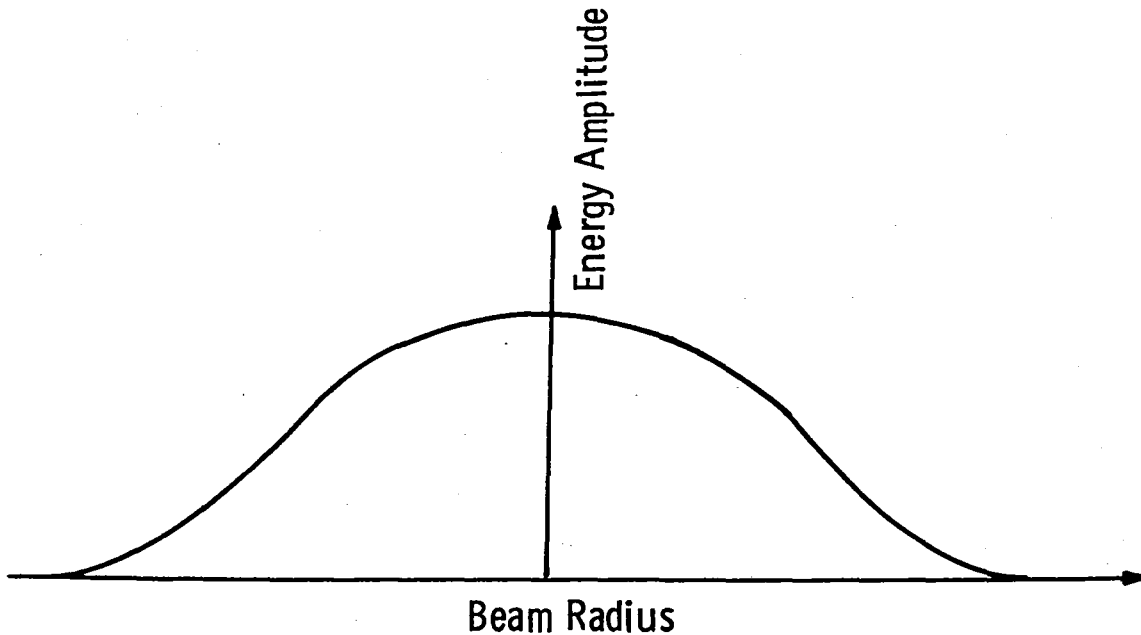


Fig. 13. Radial intensity profile of beam obtained from resonators of Fig. 12.

concave mirror with $r_2 = 0.35$, has a photon dwell time of $t_c = 6.7$ nsec according to Eq. (8), if the value $(1-r_1 r_2)$ does not have to be corrected

for losses additional to those due to mirrors. The inverted population in the laser rod is approximately proportional to the square of the voltage V with which a capacitor energizes the pumping flashlamp. With a threshold oscillation obtained for $V_t = 618$ volt, application of $V=1250$ volt produces a pulse with a rise time of 2 nsec and a decay time of about 4 nsec. The latter is shorter than the theoretical value of t_c because of absorption losses in the rod and in the polarizer and Q-switch. The asymmetrical time behavior of the pulse is not unlike that to be expected for $n_i/n_t \approx 4$. Experimentation designed to find conditions in which much longer pulse times are obtained along with smooth radial intensity profiles led us to the exploration of longer cavities.

An extreme of long pulse duration was found with the arrangement shown in Fig. 14a. Here two plane mirrors with $r_1 = 1$ and $r_2 = 0.35$,

Curve 722151-A

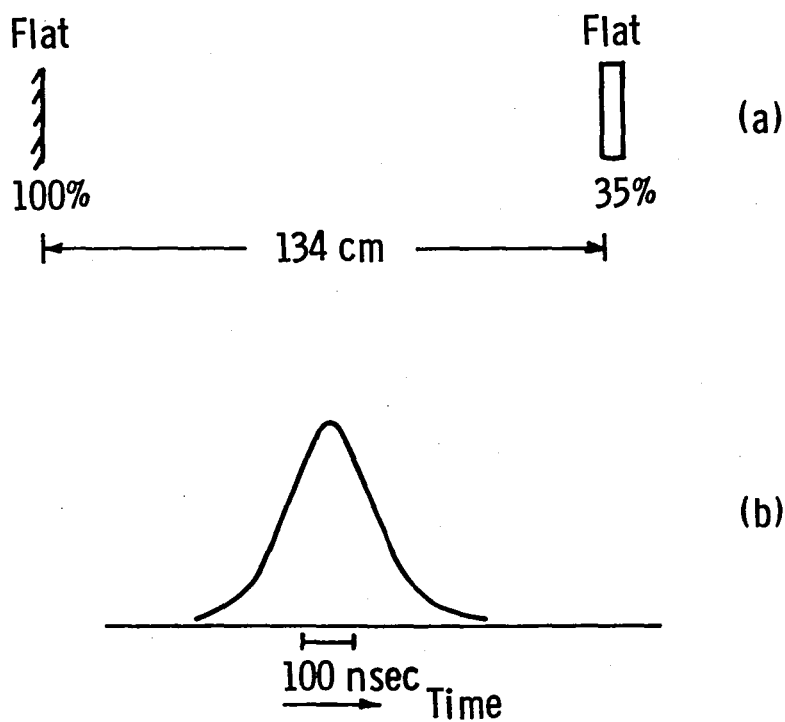


Fig. 14. (a) Resonator arrangement producing pulses of 175 nsec duration.
(b) Pulse-time profile.

respectively, bounded a cavity of $L \approx 139$ cm optical path length. The cavity is just within the limits of stability because of the thermal lensing by the rod. However, due to the loose coupling of the extended radiation field to the rod, the latter is completely filled by the waist of the beam. With a measured threshold at $V_t = 640$ volt, the cavity delivered pulse energies of 175 mJ at 1100 volt and 240 mJ at 1250 volt. At 1100 volt, the pulse has the symmetrical time behavior shown in Fig. 14b, corresponding to a duration of 175 nsec. This value corresponds to $12.2 t_c$ (cf., Eq. 8), and comparison with the theoretical pulse-time shapes imply then a ratio $n_i/n_t \approx 1.5$. Hence $V_t \approx 1100/(1.5)^{1/2} = 900$ volt, rather than the measured $V_t = 640$ volt. However, the discrepancy can be interpreted as due to the fact that in loosely coupled rods the measured threshold corresponds to the onset of oscillation in filamentary regions rather than through the full bulk of the crystal. Although the radial intensity distribution of the beam displayed a smooth Gaussian profile, no parametric conversion was obtained, presumably because the pulse duration was too long for efficient conversion.

The configuration finally adopted at Westinghouse had the cavity length and dimensions shown in Fig. 12. It consists of a plane mirror with $r_1 = 1$ separated by $L = 115$ cm from a concave 2 meter radius mirror with $r_2 = 0.35$. The threshold was measured at $V_t = 600$ volt. The pulse time behavior at 1100 volt is shown in Fig. 15. It exhibits a pulse

Curve 722147-A

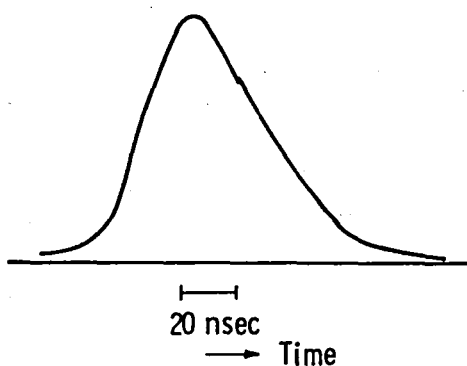


Fig. 15. Pulse-time profile of final pump chain.

length of 40 nsec. From Eq. (8), the photon dwell time is here $t_c = 11.8$ nsec so that the pulse width equals $3.39 t_c$. This corresponds to a theoretical value of $n_i/n_t \approx 2.5$ so that $V_t \approx 695$ volt. This exceeds the measured value by a smaller percentage than was the case in the preceding example, reflecting the fact that the resonator produces tighter coupling.

With a pulse duration of 40 nsec and a smooth, near Gaussian intensity profile of the spot, this cavity fulfilled the two conditions mentioned before and emerged as the optimal compromise between the conflicting requirements of high energy performance and minimal threat of radiation damage to the later stages of the optical chain. In fact, operation with this cavity for various tests has not produced any component damage over several months.

Table I lists the pulse energies produced by the oscillator-amplifier chain measured in front of the OPO, i.e., after losses in the rotator and corner mirrors have already been encountered. The oscillator flashlamp is energized with 16.9 J per pulse from a 28 μ F capacitor charged to 1100 volt. The voltages shown in Table I for the amplifier flashlamp are discharged from a 56 μ F capacitor.

Table I. Pulse Energies from Oscillator at 1100 v and Amplifier of Varying Voltage

<u>Amplifier</u>		<u>Pulse Energy from Oscillator-Amplifier</u>
<u>Volt</u>	<u>Joule</u>	<u>Millijoule</u>
0	0	110
600	10.1	152
700	13.7	190
800	17.9	235
900	22.7	285
1000	28.0	320
1100	33.9	355

When used without an etalon, the oscillator-amplifier chain produced a linewidth of $0.10-0.15 \text{ cm}^{-1}$. Thus, if the signal wave from the OPO has a linewidth of 0.2 cm^{-1} to 0.4 cm^{-1} or more, the etalon in the oscillator can be left out since it adds little to the resolution of the idler wave.

4. DEVELOPMENT OF THE OPTICAL PARAMETRIC CONVERTER

The conversion of the 1.06 μm pump beam into a signal and idler wave is based on angle tuning of $(01\bar{4})$ grown LiNbO_3 . Section 1 has already described the state of the art of such crystals at the start of this program, our initial proposal to grow such crystals ourselves, and the subsequent decision to rely on the supply from Crystal Technology and, possibly, other manufacturers who had indicated an interest at that time. Among these other sources, only Harshaw could supply us with a crystal. This had been cut along $[01\bar{4}]$ from a large boule which had been grown in the more easily attained $[100]$ direction. However, after tests at our laboratories and at Stanford failed to obtain parametric conversion with it, Harshaw indefinitely postponed further work on this type of crystal. Crystal Technology succeeded in producing $[01\bar{4}]$ grown LiNbO_3 crystals which exhibited, in our own tests and at Stanford, parametric conversion thresholds nearly as low as those of the crystals originally developed at Stanford. Nevertheless, our experience with the supply of materials, still in an early state of the art and in low quantity demand, (cf. Sect. 3.4), repeated itself. After initial high performance, the quality of succeeding samples gradually fell off and became the dominant bottleneck for the speed of the development work and the finally attained performance.

4.1 Design Considerations for the Oscillator (OPO)

The performance objectives of the parametric frequency converter are (1) high conversion efficiency (or high output energy), (2) a tuning range as wide as the transmittance of LiNbO_3 permits, and (3) a bandwidth (or linewidth) sufficiently narrow for the intended measurement purpose. The first two of these performance characteristics depend mainly on the quality of the LiNbO_3 crystal and the energy and beam quality of the pump beam. However, the bandwidth of the resonating wave is determined by the OPO, while that of the nonresonating wave adds contributions from the OPO and the pump beam. Thus the most stringent design requirement is the necessity

of additional tuning elements. This can be seen from Fig. 1 containing the tuning and bandwidth curves at various angles of incidence with respect to the optical axis of LiNbO_3 . Near degeneracy at $2.12 \mu\text{m}$, the wavelengths of signal and idler vary sharply with angle, a result of the angle behavior of the ordinary and extraordinary refraction indices which occur in Eqs. (1)-(4). For a given fall-off in gain (Eq. 4) with mismatch and a given beam divergence, the bandwidth is therefore very large at degeneracy, viz., up to 60 cm^{-1} . Hence further frequency selecting means are necessary, at least for the major part of the tuning range. This led to the design shown in Fig. 16 in which a dichroic beam splitter at the entrance to the parametric cavity serves as a window for the pump and idler beam, but as a mirror for the signal. The beam splitter coating design is determined by the wavelength range of the signal ($1.4 \mu\text{m}$ to $2.1 \mu\text{m}$), well above the $1.06 \mu\text{m}$ wavelength of the pump beam, as well as by the orthogonal polarizations of the two beams. While the pump wave passes through the beam splitter without reflection and then through the crystal towards the output mirror, the signal it generates is reflected towards a side arm of the cavity in which it encounters first a tilted etalon and then a plane grating in Littrow mounting. The signal thus finds itself in a resonant cavity bounded by a grating and an output mirror which is 70% reflecting. Broadly tuned by the crystal angle, the signal wave is now fine-tuned, first by the grating angle to a narrower width, then to a yet narrower line by the etalon tilt.

After passing through the LiNbO_3 crystal, the pump beam power is reduced by the fraction which has been converted into signal and idler power. To utilize the remaining fraction, the output mirror in this system reflects nearly 100% of the $1.06 \mu\text{m}$ beam, as well as 70% of the signal. In this double pass operation, the pump beam traverses the crystal a second time, contributing further to the conversion process, passes through the beam splitter, and leaves the pump chain via the Faraday rotator. The pump pulse energy required for the threshold of parametric oscillation, where the conversion loss to the pump is (by definition) near zero, is reduced significantly in double pass operation.

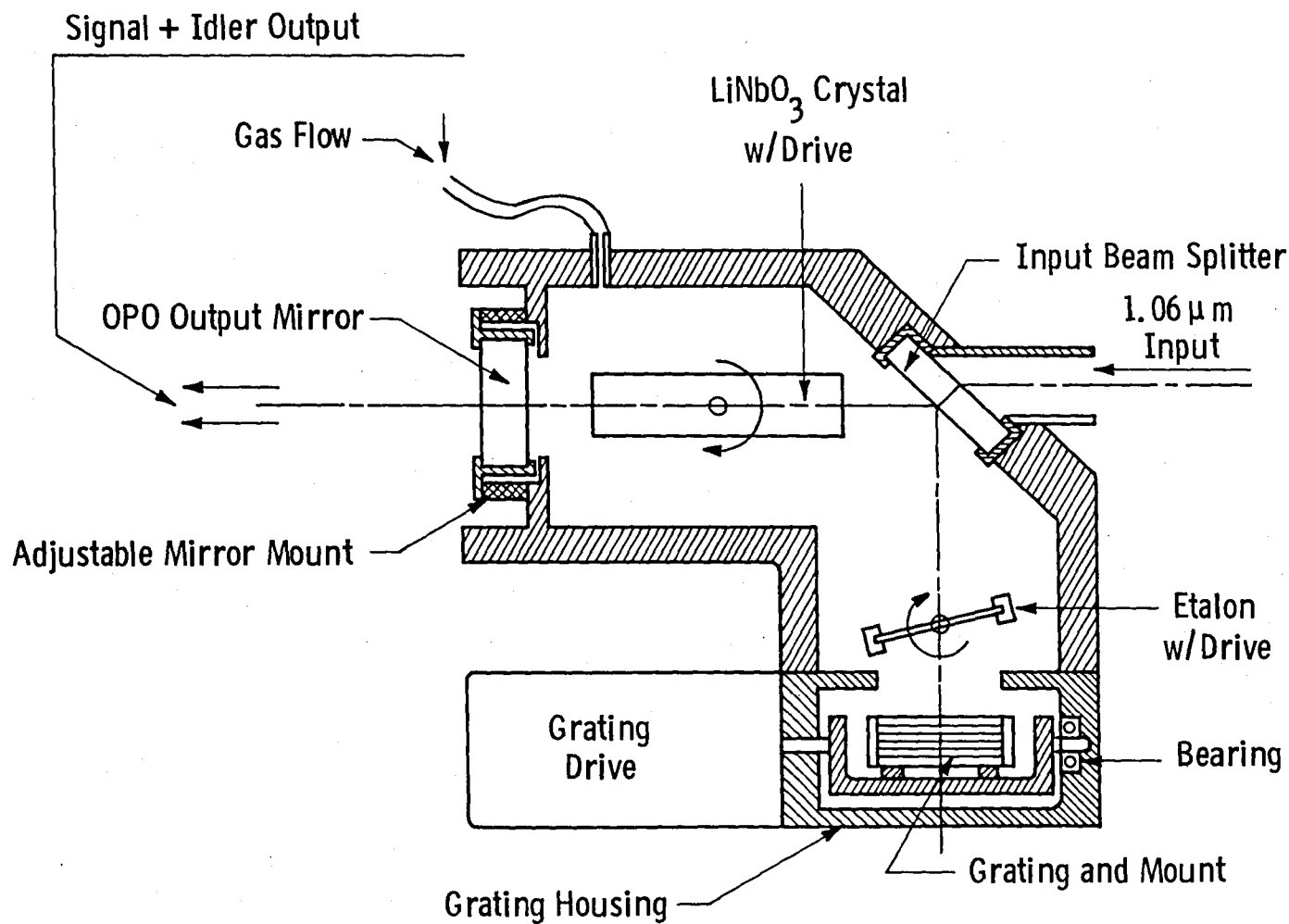


Fig. 16. Detail design of parametric oscillator.

Since a wave reflected onto itself gives rise to a standing wave with amplitudes that can approach twice that of incidence with four-fold energy density, one has to consider the possibility of a lowered damage threshold. However, the same broadening of the pump frequency which contributes to the broadening of the idler wave, also produces a broadening of the standing wave pattern. The spatial (positive and negative) amplitudes or loops are separated by $\lambda/(2n)$ in a medium of index n. If the end surface of the crystal is spaced D cm from the output mirror, the reflected wave meets the incident wave with a retardation of $2D/\lambda$ wavelength and with broadening of this length by $2D \Delta\lambda/\lambda$. Hence the ratio R of the (spatial standing wave) loop broadening to the loop interval is

$$R = \frac{4nD}{\lambda^2} \Delta\lambda$$

With $D = 1$ cm, $\lambda = 1.06 \mu\text{m}$, $\Delta\lambda = 3 \cdot 10^{-5} \mu\text{m}$, and $n = 2.2$, $R = 2.5$. Thus even for $\Delta\lambda = 1 \cdot 10^{-5} \mu\text{m}$ ($\Delta\nu = 0.1 \text{ cm}^{-1}$), the standing wave pattern is smeared out to an almost uniform axial field distribution. Indeed, no reduction of the damage threshold has been observed in double pass operation.

4.1.1 Grating

The frequency discrimination of the grating is given by the resolution which it offers to a beam of effective spot diameter, a, and angle of incidence, α . The theoretical limit for the resolution is equal to the product of the order m and the number of grating lines which, with a spacing d, are covered by the beam, viz.

$$\frac{v}{\Delta v} = \frac{ma}{dc\cos\alpha} \quad . \quad (9)$$

The grating equation in terms of frequency in units of cm^{-1} yields then from Eq. (9)

$$\Delta\nu = \frac{1}{2a \tan\alpha} \quad . \quad (10)$$

The grating selected among the standard rulings available from Bausch and Lomb had 600 lines per millimeter and a blaze angle of $28^\circ 41'$, corresponding to a blaze wavelength of $1.60 \mu\text{m}$. The effective spot diameter of the beam, i.e., the width of an equivalent rectangular beam which illuminates the lines it covers with equal intensity, is of the order of 0.5 cm. The angle of incidence α for tuning from $1.4 \mu\text{m}$ to $2.13 \mu\text{m}$ varies from 24.8° to 39.4° , respectively. This corresponds to a theoretical bandwidth $\Delta\nu$ varying from 2.2 cm^{-1} to 0.82 cm^{-1} respectively. The actually measured bandwidths of the cavity without the etalon are between 1 and 2 cm^{-1} . However, the agreement is probably fortuitous because of factors not considered here, especially the bandwidth narrowing effect of multiple traversals of the signal wave and the broadening effect of the beam divergence. Furthermore, while the grating resolution decreases for shorter signal wavelength, angle tuning becomes the more dominant frequency selection process because of the decreasing slope of wavelength with crystal angle (see Fig. 1).

4.1.2 Tilted Etalon

The intracavity use of tilted etalons for linewidth narrowing can be driven, in principle, to the point of limiting oscillations to a single longitudinal mode.¹¹ However, it is quite difficult to combine this capability in parametric oscillators with high energy performance and stability in operation. One of the reasons is the requirement that the free spectral range (FSR) of the etalon, given by its index of refraction n and thickness d , viz.,

$$\text{FSR} = 1/(2nd) \quad (11)$$

be large enough so as to limit oscillation to one line in the center of the frequency band admitted by the other tuning elements. In the present case, with the bandwidth limited by the grating to 2 cm^{-1} (FWHM) or less, the FSR should be a small multiple of that value, depending on the gain threshold for oscillation. Tests were performed with two Lambda-Airtron etalons, consisting of silica flats ($n = 1.46$) coated to

a reflectivity of $r = 0.60$. The first of these, 1.0 mm thick with an FSR of 3.4 cm^{-1} could indeed limit oscillations to a single line, but slight detuning from the center of the grating bandpass would permit a neighboring etalon order to be amplified. Since the simultaneous presence of two lines in the output can be detected only with a spectrum analyzer, it was preferred to use the other etalon which, with $d = 0.5 \text{ mm}$, had a free spectral range of 6.8 cm^{-1} and therefore ensured a single-order spectrum.

The disadvantage of a large free spectral range is, of course, the correspondingly large line width $\Delta\nu_h = \text{FSR}/\mathcal{F}$ for a fixed finesse of the etalon, \mathcal{F} , which (in the absence of scattering and absorption) is determined by the reflectivity:¹²

$$\mathcal{F} = \pi \frac{r^{1/2}}{(1-r)} . \quad (12)$$

For a number of reasons, however, a reflectivity of 60% producing a finesse of 6.1 represents an upper practical limit for etalons used in lasers or parametric converters, at least at higher energies. At higher reflectivities, the circulating power inside the etalon may become excessive and, furthermore, losses increase. Aside from absorption and scattering caused by the coatings, these losses result from walk-off by the beam in the tilted etalon. A certain portion of the beam misses constructive interference and is reflected, rather than transmitted, by the tilted etalon. At a tilt angle θ , the loss equals¹³

$$\ell = \mathcal{F}^2 \left[\frac{4\theta d}{na} \right]^2 \quad (13)$$

where a is again the effective beam diameter and θ/n the angle of reflection inside the etalon. To keep this loss at tolerable levels, the finesse can therefore be raised only to the extent to which the beam diameter can be maximized and the tilt angle minimized. This latter option, however, is limited by two conditions. First, a minimum tilt angle θ_0 must be maintained since, at zero angle of incidence, the signal will oscillate between the etalon and the output mirror. Within a free spectral range, the etalon therefore selects a frequency given by

$$\Delta v = v_o (\theta - \theta_o)^2 / (2n^2) \quad (14)$$

where v_o is the frequency (in cm^{-1}) for $\theta = \theta_o$ and Δv is the (always positive) increment in frequency due to the additional tilt. The maximum increment to which the etalon may have to be tuned is the free spectral range so that Eq. (14) with Eq. (11) yields for the maximum tilt angle

$$\theta_m = \theta_o + (n\lambda_m/d)^{1/2} \quad (15)$$

where λ_m is the largest wavelength to be tuned, i.e., here $\lambda_m = 2.13 \cdot 10^{-4}$ cm at degeneracy. The maximum tilt angle of a 1 mm etalon with $\theta_o = 0.020$ rad is then according to Eq. (15) $\theta_m = 0.0758$ rad. With a finesse of $F = 6.1$, the loss in single pass, as given by Eq. (13), is a still tolerable 6.4%. On the other hand, a reflectivity of 70% would produce a loss of 12.6%. The etalons were therefore designed with 60% reflectivity.

A finesse of 6.1 with a FSR of 6.8 cm^{-1} will result in a line-width of 1.1 cm^{-1} . However, the repeated traversal of the signal beam in the OPO cavity will narrow the bandwidth of grating and etalon. The present cavity, in effect, does increase the finesse by a factor of about two.

The selection of a narrower frequency width out of a homogeneously broadened band by an intracavity etalon should not produce losses other than those due to walk-off, and to a smaller extent, absorption and scattering. These losses are those of gain and thus produce a larger percentage of loss in the output. Nevertheless, unlike the external etalon, which sacrifices the energy of the frequency components it does not pass, the internal etalon draws energy from the entire homogeneously broadened pass band into its narrowed frequency region to which it restricts the buildup of modes. This advantage, however, does not apply to inhomogeneously broadened radiation,¹¹ which consists of frequency components fixed by the resonances of different oscillators or by some other cause. Such other cause is the divergence of the beam incident

on the grating to which the grating responds with inhomogeneous broadening. Thus the fraction of energy contained in the inhomogeneously broadened portion of frequencies outside the etalon bandpass is lost to the conversion process, just as if the etalon were arranged external to the parametric cavity.

Whereas intracavity losses may reduce the gain only by a small percentage, they reduce the output power by a larger factor which, of course, depends on the input power relative to the respective oscillation thresholds. Under present operating conditions (300-350 mJ pump energy) the insertion of the etalon reduces the output power by about a factor of two, in the average taken over the tuned wavelength range. With a bandwidth reduction by up to a factor four, the application of the etalon inside the cavity saves about a factor of two in power for equal linewidths (in addition to the simultaneous narrowing of signal and idler waves).

A clue to the major cause of the etalon induced losses can be obtained from their wavelength behavior. As seen by inspection of Eqs. (13) and (15), the loss contribution by walk-off increases with the tuned wavelength, the increase being linear, if θ_0 is zero. On the other hand, the loss contribution by beam divergence decreases with increasing wavelength. This can be shown from the grating equation, viz., $m\lambda = 2ds\sin\alpha$, which for a beam divergence $\Delta\alpha$, yields

$$\Delta\lambda = 2d(1-\sin^2\alpha)^{1/2} = (4d^2-\lambda^2)^{1/2} \quad . \quad (16)$$

Equation (16) represents inhomogeneous line broadening (neglecting effects of narrowing by multiple cavity passes). With $d = 1.67 \mu\text{m}$, the effect of increasing wavelength is a slow decrease of energy loss by etalon band narrowing. The energy difference between the oscillation threshold in operation without etalon and the threshold with etalon should indicate the fractional loss caused by the latter. Unfortunately the observed thresholds for the onset of oscillation are those of filamentary regions which pass through different parts of the crystal in angle tuning. The more meaningful thresholds "corrected" for full oscillation across the beam spot area can be obtained approximately from

extrapolation of the gain curves. Another indicator for the etalon losses is the ratio of the respective slope efficiencies with and without etalon at a fixed multiple of the pump threshold energy. However, this evaluation also depends on an exact knowledge of the corrected thresholds. On the basis of the data taken so far, the corrected threshold ratio increases for increased signal wavelengths. From this one may infer, tentatively, that the etalon losses are to the major part due to walk-off. On the other hand, the slope efficiencies with etalon operation are only a few percent smaller than obtained without on both ends of the tuning range. This observation is not necessarily in conflict with the prior one but it does underline the need for a more detailed study of the etalon loss effect.

4.2 Tuning Control and Display

The signal wave, which resonates in the parametric cavity between the grating and the output mirror, has to be tuned through the spectral range from $1.40 \mu\text{m}$ ($7,142 \text{ cm}^{-1}$) to $2.15 \mu\text{m}$ ($4,651 \text{ cm}^{-1}$), i.e., through an interval of about $2,500 \text{ cm}^{-1}$. The tuning is controlled by setting the angles of the three frequency selecting elements, viz., the LiNbO_3 crystal, the grating, and the etalon, to calibrated values of a digital scale or display. This control and display must, of course, be sufficiently sensitive and accurate so that the selected frequency is defined as narrowly as the spectral resolution of the respective element permits. Thus the following requirements result for the three tuning operations:

(1) Tuning the angle of the LiNbO_3 crystal over a range of about 5° covers the full spectral domain of the system for signal and idler waves (see Fig. 1). The bandwidth is very narrow near $1.4 \mu\text{m}$, where the frequency changes relatively little with angle, and is quite broad at degeneracy where the slope of the tuning curve is large. Stated differently and more accurately, the bandwidth results from the (frequency independent) minimum angular increment which the nonlinear operation of the crystal can distinguish. The accuracy of angle

control and display must be equal to, or better than, this increment. Inspection of Fig. 1 shows that an angular definition of one arc minute, representing 1/300th of the tuning range, amply fulfills that condition.

(2) The grating, used in first order so that $\lambda = 2ds\sin\alpha$, is turned from 24.8° to 40.2° through the tuning range. A lower limit for the (dynamic) bandwidth is 1 cm^{-1} , which corresponds in the average to an angular increment of $15^\circ/2,500$, i.e., to about 22 arc seconds. The smallest increment occurs at the smallest wavelength since, from the grating relation,

$$\Delta\alpha = 2ds\sin\alpha \tan\alpha \Delta\nu . \quad (17)$$

At $1.4 \mu\text{m}$, with $\lambda = 1.67 \times 10^{-4} \text{ cm}$, this amounts to 13.4 arc seconds or about 1/4000 of the angular range.

(3) The etalon has to be tuned over its free spectral range, $\text{FSR} = (2nd)^{-1}$, at any interference order. Its linewidth, FSR/\mathcal{F} , corresponds to an angular increment of θ obtained by differentiation of Eq. (14):

$$\Delta(\Delta\nu) = (2\mathcal{F}nd)^{-1} = 2v_o(\theta - \theta_o)\Delta\theta / (2n^2) = (2v_o\Delta\nu)^{1/2} \Delta\theta / n \quad (18)$$

so that

$$\Delta\theta = \frac{1}{2\mathcal{F}} \left(\frac{n}{v_o d} \right)^{1/2} \quad (19)$$

where the most demanding case, viz., $\Delta\nu = \text{FSR}$ has been introduced. For an etalon thickness $d = 0.05 \text{ cm}$, $\mathcal{F} = 10$, and the largest value of v_o , viz., $7,143 \text{ cm}^{-1}$, the angular definition amounts to 11 arc minutes. The etalon, of course, is the tuning element of smallest band width. Whereas a slight detuning of the grating merely reduces the output power by a small fraction, the etalon determines the frequency of peak emission and, thus, the peak should be tuned within about 1/10 of the linewidth, reducing the angle tolerance to about one arc minute. Since the largest tuning angle is 0.076 rad (see Eq. (15)), corresponding to 4.5° , the readout should have a resolution of 1 part in 300.

Table II summarizes the requirements of angle control and read-out definition for the three tuning elements.

Table II. Accuracy Requirements for Angle Control and Digital Display

Tuning Component	Angle Tuning Range	Angle Accuracy	Display
LiNbO ₃ Crystal	5°	1 arc minute	1:300
Grating	15°	13 arc second	1:4000
Etalon	4.5°	1 arc minute	1:300

The choice of devices which can perform angle tuning with the desired accuracy depends also on other considerations such as speed of the tuning operation, convenience of scale reading, compatibility with computer control and read-out and, last but not least, reproducibility of frequency setting for random access. For example, conventional mirror mounts with manually controlled micrometer screws respond to these conditions poorly or not at all.

The angle control means chosen as the best answer to all these requirements are the Moving Iron Galvanometers produced by General Scanning.

The galvanometer uses a rotating iron armature held between four stationary pole pieces. The latter form a balanced magnetic circuit which can be modulated by driving coils providing a linear electromagnetic torque to the armature. Capacitive position sensing produces an error signal for negative feedback to the coil current so that a desired angle is attained without overshoot. Specifications include a repeatability error of less than 50 microradian (10 arc seconds) and a thermal drift of 30 arc seconds/degree C.

Three of these galvanometers are provided as integral parts of the parametric oscillator cavity. Each is controlled by a voltage that is displayed with four digits for the crystal and the grating and with three digits for the etalon. Furthermore, the voltage interval between the steps of the last digit can be fine-tuned.

It is not impossible under laboratory conditions, if they include temperature control of the optical system with 0.25°C stability and

stationary location, to attain a long term repeatability of tuning conditions with the accuracy required by Table II. After calibration of the voltage scale in terms of frequency and wavelength with an accuracy of 1:10,000, one could then perform tuning to any desired operating point without periodic reference to a wavelength standard. Tuning and data acquisition could then be left to a computer which would receive, as single input, the desired wavelength on a code for the gas spectrum resonance of interest. Repeatability of the voltages from day to day for a fixed setting and reproducibility of the calibration within a few tenths of a percent was indeed observed. Figure 17 shows calibration curves for the angles of crystal and grating in terms of the digital readout in volts versus signal and idler wavelengths in μm . The calibration was obtained by comparison with a Jarrell-Ash Spectrometer Model 82-000. However, a reproducible calibration for the etalon angle can not be performed. The etalon, as the final tuning element, provides a resolution of 10,000 for the location of a spectral line, requiring a stability beyond the scope and objectives of this system.

The delivered system includes a monitor cell which, when filled with selected gases of interest, allows fine-tuning directly to desired resonance lines which are found with the aid of the calibration curves. Using several gases, one can establish whether misalignment has caused changes in the calibration.

4.3 Design, Supply, and Performance of LiNbO_3 Crystals

Most of the essential components making up the parametric converter, such as dichroic coating mirrors, the LiNbO_3 crystal, and the galvanometers represent developments of the last 10 years. However, because of their extended use in other areas of optics, the problems of quality control had been overcome at an early stage, except for the case of the crystal. Demand for (014) grown LiNbO_3 crystals is still limited, and there exists only a single commercial supply source: Crystal Technology Inc.

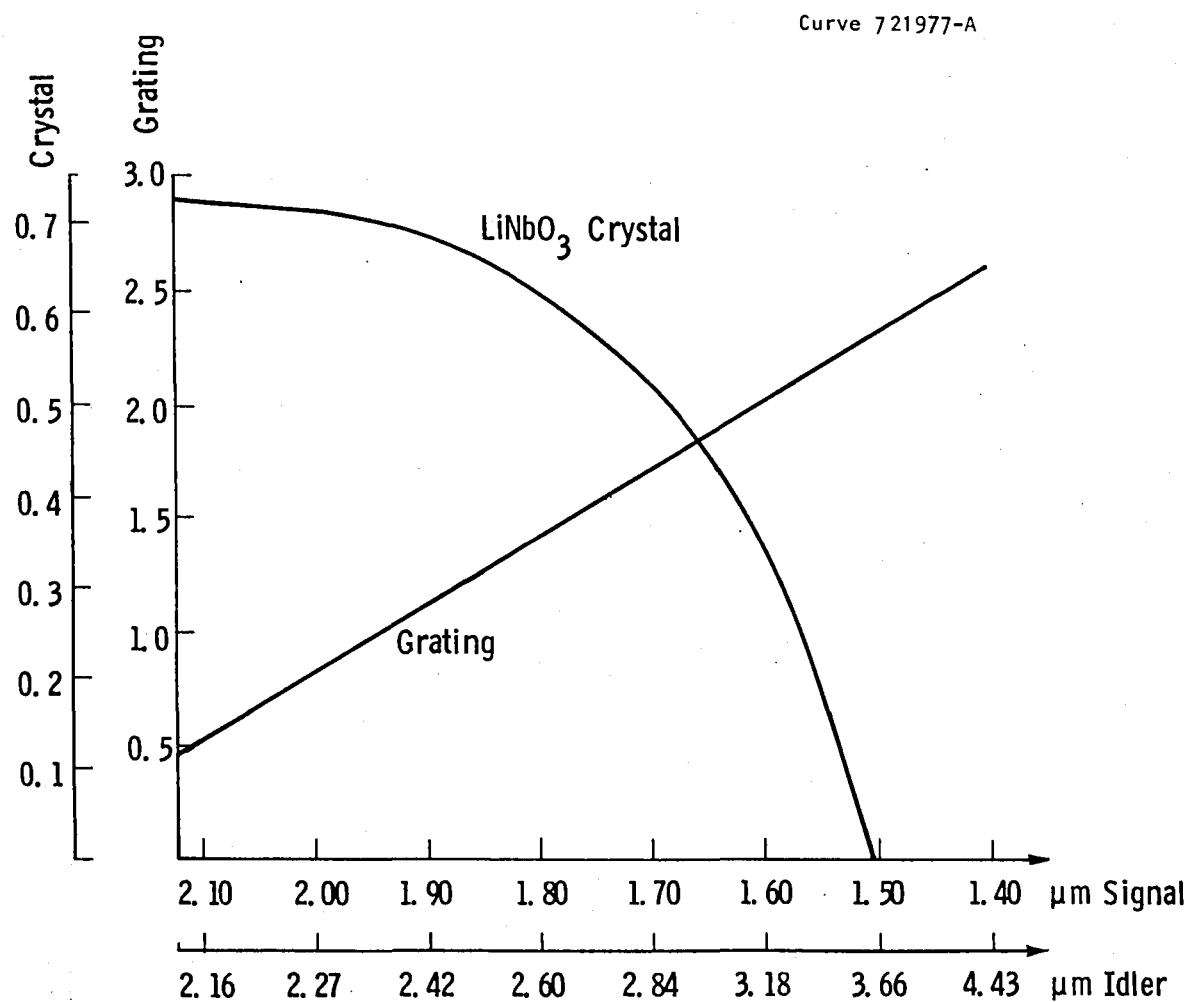


Fig. 17. Calibrated tuning curves for angles of crystal and grating in OPO.

4.3.1 Gain and Damage Limits

The design of a crystal from an (014) grown boule involves only the choice of diameter and length. These are determined by considerations of conversion gain, damage threshold, and walkoff. The gain at band center follows from Eq. (3) for $\Delta k = 0$:

$$G = \sinh^2 \Gamma L \cong 1/4 e^{2\Gamma L}; e^{\Gamma L} \gg 1 \quad (20)$$

where for a Gaussian beam and defect-free LiNbO_3 crystal Γ at degeneracy ($\omega_i = \omega_s$) equals¹³

$$\Gamma_o = 1.5 \cdot 10^{-4} I^{1/2} (\text{cm}^{-1}) \quad (21)$$

where I is the pump intensity in watts/cm². For given pulse energy or power of the pump, the gain increases exponentially with (linearly) decreasing beam diameter. However, energy density and intensity are both limited by the respective damage thresholds to which they should assume ratios of no more than 1:2. The gain increases exponentially also with crystal length L . Again, this approach is limited by birefringent walkoff, typically at an angle of 0.04 rad. Another limitation to increasing the length is the expectation, corroborated by experience, that increased crystal volume is likely to have decreased quality.

We experimented with crystals varying in length from 50 to 60 mm and in diameter from 10 to 15 mm. These acquisitions considerably exceeded the original expectation of purchasing only three crystals, of which two were to have been spares. The expectation was based on the initial experience of the Stanford workers. Using the Gaussian beam from a stable resonator on a crystal grown at the university, they encountered no radiation damage over a period of nine months with pulse energy densities of over 1.8 J/cm², which was threefold the threshold for oscillation. However, when the need for larger pulse energies forced the groups at Stanford and Westinghouse to use beams of larger diameter from unstable resonators, radiation damage of the crystals made its appearance at unpredictable levels of energy density. The damage

mechanism is not well understood, but it is clear that the space-time distribution of the pulse energy and defects of crystal quality are both involved. The measures taken to improve beam quality by avoiding discontinuities or stress concentrations have been described in Section 3.5.5.

4.3.2 Control and Improvement of Crystal Quality

The improvement of crystal quality, of course, required the cooperation of the supplier. Ideally, the LiNbO_3 crystal should exhibit the gain behavior predicted by Eqs. (20) and (21) and reach the desired output level at pulse energies well below the damage threshold. However, these criteria cannot be used as the basis for the acceptance or rejection of a crystal because they also involve the quality of the pump beam. Simpler criteria are the pump energy threshold for the onset of parametric oscillation under well defined beam and cavity conditions and the damage threshold. Empirically it is known that about 10% conversion efficiency is obtained for pump powers of twice the oscillation threshold and about 20% for threefold threshold. Thus the damage threshold should be six times larger than the oscillation threshold for 20% conversion efficiency.*

After negotiations over several months an agreement was reached under which Crystal Technology would have its crystals tested by Quantaray before they were released for delivery. The tests consisted of oscillation threshold measurements in a simple cavity embodied by two aligned mirrors. These thresholds were, of course, lower than those to be expected in cavities containing grating, beam splitter, and etalon, but correlation factors can be established, and the tests, at any rate, produced a

* It does not matter whether these relative values refer to energy densities at the spot distribution peak or to an average over the beam spot area, provided one compares similar radial profiles of energy density. However, because spot profiles vary greatly with different systems and experimental conditions, it is often preferred to define the damage threshold as that of the peak density. The latter exceeds the average spot density by a form factor which depends on the distribution shape.

statistical performance scale on which a pass-fail criterion was based. Crystal Technology also agreed to deliver to us crystals accompanied by disk-shaped boule sections (blanks) cut axially adjacent to the rod itself. This contributed to the determination of safe operation levels.

On our part, we explored the possibility of increasing damage resistance for given beam and crystal quality conditions. Experiments were performed with blanks, delivered by Crystal Technology, that were antireflection (A.R.) coated or uncoated. The most important result of these tests was the finding that the damage threshold could be reduced by more than a factor of two in uncoated crystals operated at higher temperatures (150–250°C). However, A.R. coated crystals which per se already exhibited a higher threshold than the uncoated samples, gained only about 33% of damage threshold increase (see Fig. 18). These and

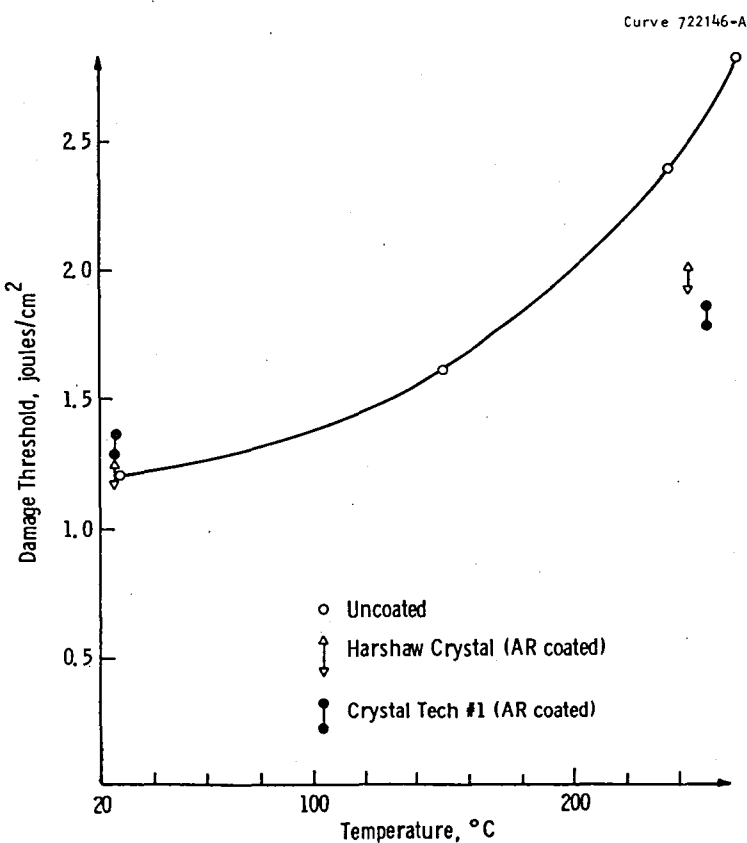


Fig. 18. LiNbO_3 damage threshold as a function of temperature.

other observations emphasized the important role of the crystal surface in damage processes. Experiments on the small blank samples, for example, showed that a damage spot first appeared on the back (beam exit) surface of the disk and another subsequently on the front surface, both on intersections with the beam axis. This sequence repeated itself even when the back surface was left diffusely reflecting after cutting. It is likely that reflection of the beam, by adding an electric field in phase with the incoming field, increases the vulnerability of the exit side. However, damage tests on disks suspended in index matching fluids proved negative: behavior and thresholds of damage remained unchanged. It was concluded that the only operational method for damage threshold reduction discovered by these experiments was the operation at elevated temperatures. The difficulty of redesigning the crystal mounting for elevated temperature operation was that it involved a major design change, mainly because the galvanometer response is extremely sensitive to temperature drifts. The uncertain advantages for coated crystals and the magnitude of the necessary changes required argued against adoption of the heating method on this contract.

It was established, further, that crystal damage could also be initiated in the bulk rather than at the surface. By passing a He-Ne laser beam through the crystal and viewing forward scattering from it as close to the axis as safely possible, defects could be detected that had escaped other means of observation. Such defects were found in rods that had not yet been exposed to high energy pump radiation. In at least one other sample, we viewed scattering after radiation damage was suspected. Here a bulk defect had given rise to a string of scattering centers, their pearl-string appearance suggesting a self-focusing mechanism. We suggested to Crystal Technology that they include this inspection method in their quality control program.

Table III presents a record of the crystals acquired and their present condition. Figure 19 shows the oscillation threshold as a function of signal wavelength for various crystals with their date of acquisition. The significance of the latter is that the trend of performance with time, as measured by delivery dates, has been rather downward, an

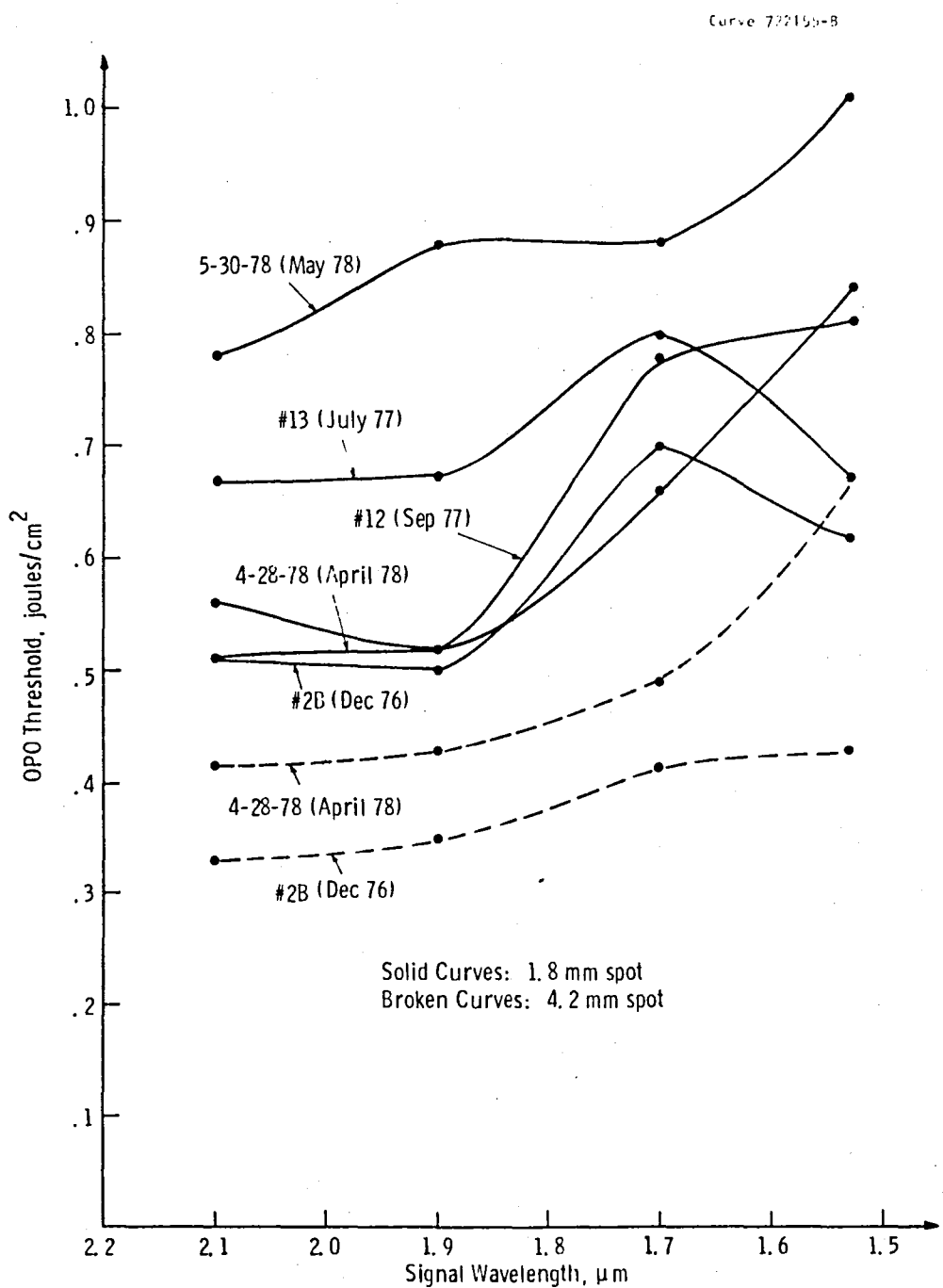


Fig. 19. Oscillation thresholds in the tuning range with a 4.2 mm beam for various crystals.

observation which, as described in Section 3.4, also applies at least for some time to other materials and processes which are at an early state of the art.

Table III. Record of LiNbO₃ Crystals Acquired

Date of Manufacturer Delivery	Dimensions	Manufacturer	Purchaser	Condition
Dec. 1974	10 x 50 mm	Harshaw	Westinghouse	Did not oscillate
Jan. 1975	10 x 45	Crystal Techn.	Westinghouse	Damaged, not usable
Dec. 1976	10 x 50	Crystal Techn.	Westinghouse	Damaged, not usable
July 1977	11 x 50	Crystal Techn.	Westinghouse	Good
Sept. 1977	12 x 50	Crystal Techn.	Westinghouse	Damaged, but usable
April 1978	15 x 60	Crystal Techn.	Westinghouse	Good
June 1978	15 x 60	Crystal Techn.	Returned	High oscillation thresh
April 1979	15 x 60	Crystal Techn.	Returned	Contained defects

The five solid curves of Fig. 19 were all taken with a simple O.P.O. cavity consisting of two 90% reflecting mirrors pumped by a Gaussian beam of 1.8 mm diameter at half power. The value of such oscillation threshold measurements lies in the possibility of comparing relative performance through the tuning range of various crystals. The absolute values of thresholds depend on beam shape, pulse length (here 10 nsec) and alignment precision which are difficult to reproduce. Nevertheless, it is seen that the most recently produced crystal had the highest threshold and that the performance of earlier crystals is in general better. The dashed curves of Fig. 19 were taken with a 4.2 mm diameter beam from the hybrid unstable resonator (60 cm mirror spacing).

4.3.3 Effect of Beam Diameter

Similar curves are presented in Fig. 20 for a spot diameter of 6 mm. It will be seen that for increasing spot diameter, one observes a decreasing oscillation threshold. The reason for this behavior is most likely birefringent walk-off which affects beams of smaller diameter

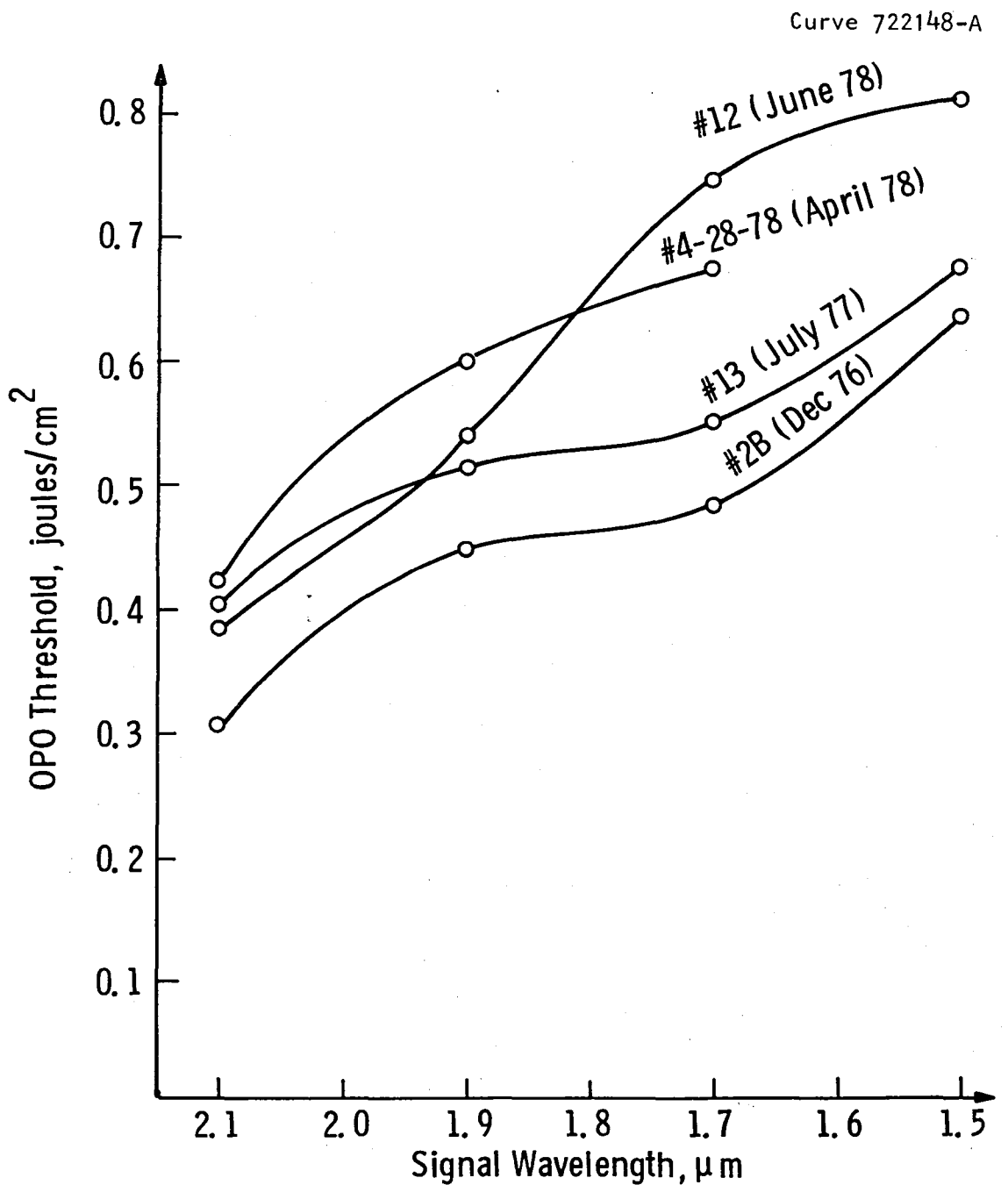


Fig. 20. Oscillation thresholds in the tuning range with a 6 mm beam for various crystals.

more than those that are wider. A walkoff angle of 0.04 rad displaces the two axes of the pump and signal beams by 2 mm at the end of a 50 mm path length.

If one approximates the interaction space of two 1.8 mm diameter beams by that of two 1.8 mm diameter cylindrical beams, one obtains a conversion gain which decreases along the propagation path to the value zero at 45 mm. The actual decrease of gain with propagation distance through the crystal depends on the radial intensity profile; for Gaussian beams, the decrease is quite fast in the beginning and approaches zero asymptotically near the end of the crystal in this example. If the gain is high, it behaves as if the crystal had been shortened from a length L to $L_1 = L - \Delta L_1$, so that it is reduced by a factor $\exp(2\Gamma \Delta L_1)$, according to Eq. (20), from the value for zero walkoff. An "effective" value L can be determined, in principle, by measuring the crystal gain and applying Eqs. (20) and (21). In practice, the gain parameter Γ depends on crystal quality and beam shape, and the measured values of gain include cavity losses. However, it is possible to arrive at more meaningful relative values. Here we use the arguments (1) that two beams of different spot size reach the same gain, $G_1 = G_2$, at their respective oscillation thresholds and (2) that, according to Eq. (3), the gain G at degeneracy depends only on the product ΓL (throughout the range of ΓL). Hence, at threshold, $G_1(\Gamma_1 L_1) = G_2(\Gamma_2 L_2)$. Thus if we compare the oscillation threshold of two beams with similar, but not necessarily Gaussian, shapes of different diameters a_2 and a_1 , then we obtain for the relationship of the threshold intensities I_2 and I_1 , according to Eqs. (21) or (4):

$$I_2^{1/2} L_2 = I_1^{1/2} L_1 \quad (22)$$

where L_2 and L_1 are the respective (effective) interaction lengths for the two beams and where we have assumed identical gain conditions aside from the effect of the different beam diameters. In practice, this assumption can hold only approximately, first, because alignments for different beam spots will differ somewhat, and second, because the

crystals are not strictly homogeneous and the gain parameter will vary somewhat across the bulk. The effect of beam spot diameter on the oscillation threshold of O.P.O. double pass operation is shown in Columns I and II of Table IV for a Gaussian beam as well as for the semi-Gaussian profile produced by the pump chain of the final system. Column III shows the percentage reduction of the interaction length, $\Delta L/L_3$, i.e., compared to L_3 for the largest spot diameter listed in the third row. These values follow from Eq. (22) written in the form

$$\frac{\Delta L}{L_3} = 1 - \left(\frac{I_3}{I} \right)^{1/2} . \quad (23)$$

The data for Table IV were obtained with crystals of 50 mm length and a damage threshold in single pass of 3.5 J/cm^2 (10 nsec pulse). This is assumed to correspond to a damage threshold of 1.8 J/cm^2 in double pass so that the values of Column IV result which list the ratio of damage to oscillation threshold.

Because of the difficulty in producing identical gain conditions for a comparison of the effect of spot size, the reproducibility of these relative values is not better than 10-20%. Nevertheless, the trend of the oscillation threshold to lower values for larger beam diameters is clearly established. The corresponding increase of interaction lengths, derived from them, imply that beams of about 1.5 mm diameter interact less than over 2.5 cm, those of 4 mm over less than 4 cm. These upper limit estimates result from the consideration that the effective interaction length even of the largest diameter beam in Table IV falls short of the 5 cm crystal length. In particular, the data for $\Delta L/L_3$ of the Gaussian beam are based on the length for 3 mm diameter. That length itself is probably less than 3 cm so that the Gaussian interaction path at 1.4 mm will be less than 2.5 cm. This can be confirmed by two-dimensional diagrams for the interaction space of two beams with Gaussian radial distribution inclined at 0.04 rad with respect to each other.

The significance of lowered threshold densities for oscillation lies in the increase of conversion efficiency, first, because of the

increased operation-to-threshold ratio for fixed input fluence and, second, because of the higher damage-to-oscillation threshold ratio which allows larger pump energy densities. As seen in Table IV, the present system exhibits a damage to oscillation threshold ratio of 6.2. Since these data were taken at 10 nsec, it is possible that a larger ratio is obtained with the present pulse time of 40 nsec.

Table IV. Effect of Beam Diameter on Double Pass Oscillation Threshold

Beam Diameter mm	<u>Gaussian Spot Profile</u>		
	I	II	III
	Oscillation Threshold J/cm ²	$\Delta L/L_3$	Damage/Oscillation Threshold
a_1	1.4	0.7	26%
a_2	2.0	0.53	15%
a_3	3.0	0.38	0
			2.6
			3.4
			4.7

Semi-Gaussian Spot Profile

Beam Diameter mm	<u>Oscillation</u>		
	Oscillation Threshold J/cm ²	$\Delta L/L_3$	Damage/Oscillation Threshold
	Damage/Oscillation Threshold		
a_1	1.4	0.70	35%
a_2	4.3	0.50	24%
a_3	6.0	0.29	0
			2.6
			3.6
			6.2

4.3.4 Tuning Range of LiNbO₃ Crystals

Intrinsic absorption in the near infrared limits LiNbO₃ only for wavelengths larger¹⁴ than about 5.0 μ m. However, impurity generated extrinsic absorption shifts the onset of absorption to somewhat shorter wavelengths and also produces a narrow absorption band near 2.87 μ m. This band, and perhaps that near the edge, is caused by OH-radical absorption. Figure 21 shows the transmittance between 2.5 and 4.5 μ m which was measured with a 6 cm long crystal obtained from Crystal Technology. This may be compared with the transmittance shown in Fig. 22 of a crystal grown at the Bell Telephone Laboratories¹⁴ where crystal

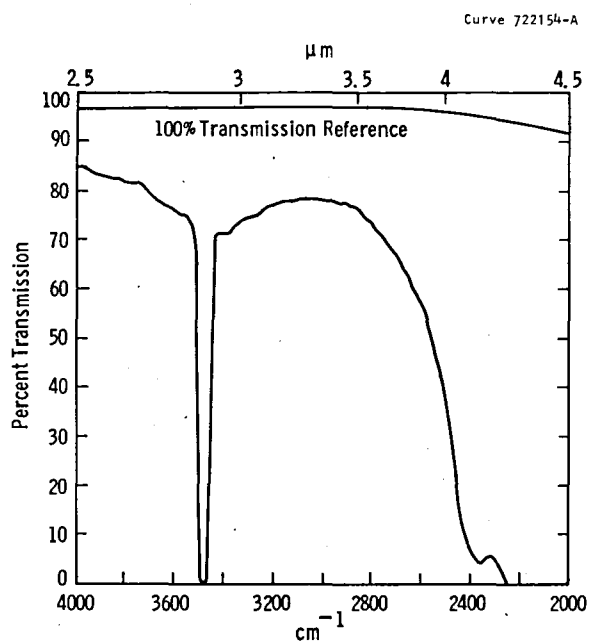


Fig. 21. Transmittance of an LiNbO_3 (Crystal Technology Corp.) crystal in the idler range.

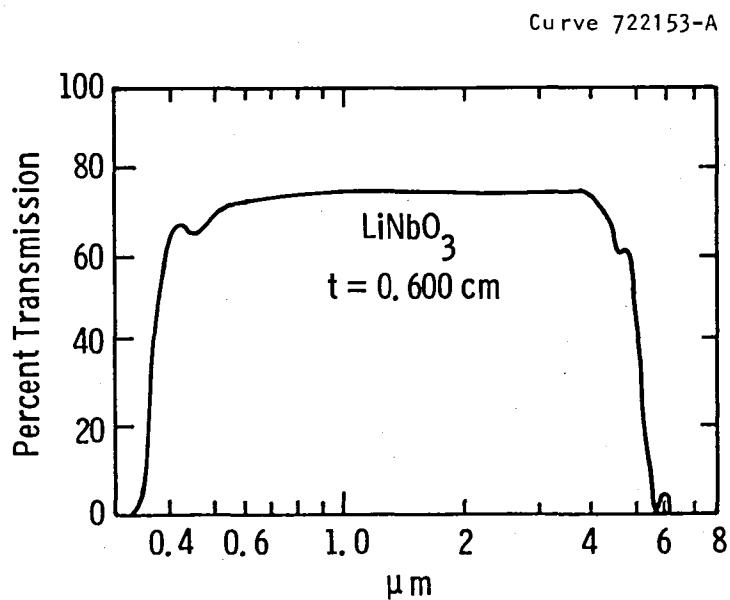


Fig. 22. Transmittance of an LiNbO_3 (Bell Telephone Laboratories) crystal in the UV, visible and IR range (from reference 14).

growth of LiNbO_3 originated. In this comparison, the transmittance must first be corrected for 29% reflection from the two surfaces and second for the factor 10 by which the crystal length in Fig. 21 exceeds that of Fig. 22 and which enters the corrected transmittance as the 10th power. Nevertheless, it is seen that the absorption band at 2.87 μm can be avoided and that useful transmission is obtained at wavelengths well above 4.0 μm . The OPO of the present system has an upper wavelength limit of 3.7 μm where the crystal has about 20% absorptance. The quality represented by Fig. 22 would extend that limit to about 4.4 μm . In the Stanford crystal growth process, OH is removed by a scavanger addition, the absorption band at 2.87 μm is eliminated, and the crystals can generate parametric conversion^{13,15} through 4.4 μm .

The extension to 4.4 μm requires a cavity gain increase for the signal by replacing the output mirror with one of high reflectivity at about 1.4 μm . In our case, this measure is precluded by the crystal absorption. Should Crystal Technology adopt the process for the removal of impurities, the oscillation range will be increased.

Figure 1 shows that the band width of angle tuning the crystal near this limit is quite small. Thus grating action may be unnecessary, and one may replace the grating by another mirror with high reflectivity at 1.4 μm .

4.5 Development of the Optical Parametric Amplifier (OPA)

Parametric amplification is indicated, if the parametric oscillator can be driven to efficient operation with part of the pump power, while the remainder of the latter is still capable of extracting sufficient gain from a second nonlinear crystal. Typically, a laser-amplifier chain generating 300 mJ pulse energy would have a useful 200 mJ pulse energy available for the amplifier, provided it can generate 10-20% conversion efficiency in the parametric oscillator with 100 mJ pump energy. Under such conditions, the three parametric waves interact in the amplifier crystal at high amplitude values, but under conditions in which the loss producing components of a resonating cavity are absent.

This advantage is particularly important for the idler beam which is generated in two directions by the signal and pump waves inside the OPO cavity. Since the idler beam is not resonating, only half of its power is emitted towards the output window. The latter transmits typically two-thirds of the idler spectrum which thus emerges with 33% of the generated power.

The presence of a parametric output mirror, which reflects the pump beam for double pass operation, and also the damage limit of the oscillator crystal, exclude a design in which the three beams proceed together towards the amplifier. Instead, the construction shown in Fig. 3 is adopted. A combination of two beam splitters and two highly reflecting mirrors lead a designated fraction of the pump beam around the oscillator cavity to collinear superposition with idler and signal beam in front of the amplifier. The first beam splitter functions as amplitude divider, the second as dichroic mirror, reflecting most of the pump beam, but passing most of the signal and idler. The amplifier housing requires means to adjust the angle of its LiNbO_3 crystal to galvanometer mount similar to that used in the OPO.

The construction of this amplifier arrangement was carried through, although it became apparent that the quality and quantity of available LiNbO_3 crystals would not suffice to reach gains for which amplifier operation was indicated. Tests showed oscillation thresholds of a magnitude which required the entire available pump power for even a 10% efficient conversion of this pump power in the OPO. Nevertheless, experiments were undertaken to determine whether an advantage would result from a division of the pump power between oscillator and amplifier. Amplification by a factor of three was obtained with a 3 mm diameter beam of 115 mJ for the oscillator and 250 mJ for the amplifier. The oscillator then operated at less than twice threshold. At 1.7 μm signal wavelength, the total output amounted to 6-7 mJ, considerably less than obtainable with the oscillator alone when pumped with full power of the driving chain. Other divisions between parametric oscillator and amplifier with the available crystals did not improve these performance values.

The amplification factor is very large for the smallest signal powers, but decreases as the signal power is increased and assumes finally

(at several mJ/cm^2) approximately the slope $E_{\text{sig}}^{1/2}$ so that the amplified signal increases as $E_{\text{sig}}^{1/2}$. In contrast, an increase of the pump energy produces an increase of the amplification factor at slightly higher than a linear rate. This implies that for a given pump energy, the amplification factor will increase for decreasing oscillation threshold. Taken together, the characteristics of parametric amplifier operation are useful for crystals of high damage to oscillation thresholds, particularly under tuning conditions which produce low gain in oscillation buildup. Such conditions exist for the idler beam, for operation with etalons, and for operation near the limits of the tuning range.

The delivered system includes the amplifier section, but the first beam splitter and an amplifier crystal have to be inserted to convert from OPO to OPO/OPA operation.

5. PERFORMANCE TESTS AND CAPABILITY OF THE FINAL SYSTEM

The development of the present system involved to a large extent original applied research. It was initially intended to be developed by tracking the results of Professor Byer's group at Stanford University. However, as described in various previous sections, that work (as well as that pursued in one or two other laboratories) was itself still in a stage of experimenting with different means and configurations, many of which were not suitable for the intent and scope of the Westinghouse project. The latter, therefore, had to develop and test some of its own innovative concepts. These included the hybrid resonator, a highly efficient Faraday isolator design and its control, improvements on the basic arrangement of the parametric cavity, and advances in the operation of LiNbO_3 crystals to increase the damage to oscillation threshold ratio. In the cooperative interaction with Stanford, these innovations were usually tested and, if suitable, adopted by Byer's group. The majority of the developments in our work were, of course, adaptations to the Stanford results, including the high energy operation with the large crystals of (014) grown LiNbO_3 , as well as the overall system concept. Experiments on new methods, components, and subsystems are to a large extent performance tests themselves. Such test results have already been described in the preceding sections. However, near the end of the contract, tests on the assembled and finalized system were performed just before its delivery and these will be described in this section.

5.1 Test Conditions and Limitations

As shown in Table III of Section 4.4.2, there were only two undamaged LiNbO_3 crystals left which were delivered to NASA-Langley together with two damaged crystals. At the time of this writing Crystal Technology has informed us that there are now a number of good quality

crystals available, but while the laser system testing was done it was not possible to obtain crystals of lower oscillation threshold than those at hand. Thus the tests were performed with a crystal which, for the same beam area, had a considerably higher oscillation threshold than the Crystal Technology samples that were first received, but damaged in earlier tests. A second constraint of the supply limitation was that further damage could not be risked. For example, because one crystal had been damaged in tuning to 1.45 μm signal wavelength, perhaps due to the corresponding absorption edge of the idler spectrum, operation at signal wavelengths shorter than 1.5 μm was avoided. An upper limit of 300 mJ for the pump energy incident on the parametric cavity was strictly observed in all tests with all pump pulse durations, although the present crystals might have a higher (but untested) safely limit at the present pulse length of 40 nsec. The system, of course, had been designed for 300 mJ pump energy because that is sufficient to attain the conversion efficiency objectives with LiNbO_3 crystals of the original quality. In fact, higher pump energies may also damage components in the optical chain in front of the parametric cavity.

5.2 Test Procedures and Results

As a first step, the scale of the grating angle was calibrated by comparison with the fourth order grating of a Jarrell-Ash spectrometer as already discussed in Section 4.3 (see Fig. 17). This calibration was carried out for the signal wavelengths between 1.5 μm and 2.15 μm , to which the idler wavelengths are related via Eq. (1), although the idler calibration could also be verified directly by comparison with the spectrometer up to 2.7 μm . In any tuning procedure, the grating angle is varied, as the first among the three tuning elements, to the desired wavelength either by comparison with a spectrometer or with a suitable absorption line of the gas monitoring cell. Next the crystal is rotated so that the maximum of its response is coincident with that of the grating. Adjustment of the etalon angle then completes the fine-tuning process.

In the test operation of the final system, the pump pulse energy was next varied at a fixed wavelength setting to measure oscillation

threshold, output energies, and slope gain. This procedure was repeated with and without inclusion of the etalon and for various fixed wavelengths (see Fig. 23). Two sets of such output energy measurements were performed with a calibrated Gen-Tec pyroelectric detector of 7/8" diameter receiving surface. In one set of measurements, the total energy of signal and idler was recorded, correcting for the small fraction of the pump beam still remaining (after reflection from the back mirror) and its harmonic by detuning the grating. The measured total of conversion energy is shown in Fig. 23 by the full curves for operation without etalon and by the dashed curves for operation with etalon. In the second set of measurements, the output beam was dispersed by a silica prism. By blocking the other wavelength components, the energy content of each individual dispersed beam could be determined. Additional measurements established correction factors for the absorption losses experienced by the idler in the prism and a focusing lens in front of the detector. Typical relative readings of signal and idler energy and the corrected ratio of idler to the sum of signal and idler energy are shown in Table V.

Table V. Relative Values of Signal and Idler Energies

Idler Wavelength μm	Signal Wavelength μm	Signal Energy	Idler Energy	Idler Energy Corrected	Ratio Idler/(Idler+Signal)
2.4	1.9	11	3.0	3.3	23%
2.8	1.7	4.0	0.4	0.8	17%
3.5	1.5	5.5	0.5	0.8	13%

The percentage contribution of the idler to the total converted energy is shown on representative curves of Fig. 23. In terms of the basic conversion process, equal numbers of idler and signal photons are produced by the same number of photons, so that the energy ratio of idler/(idler+signal) photons equals $\lambda_s / (\lambda_s + \lambda_i)$. These two components suffer losses before emerging from the cavity, each because of different causes. Since the signal is resonating, it undergoes many small absorption

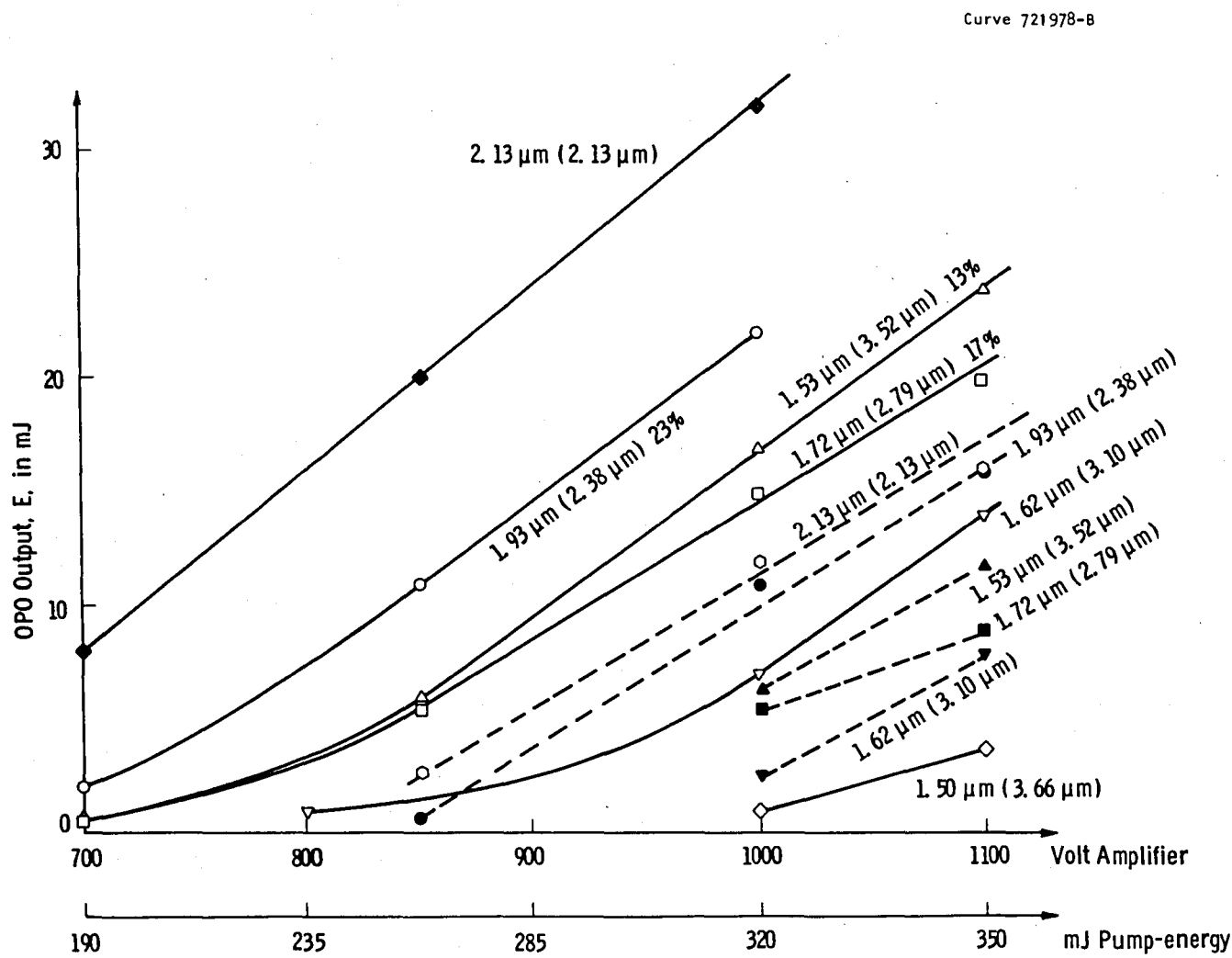


Fig. 23. Parametric pulse energies for increasing drive by the pump chain for several tuning points. Dashed curves were taken for operation with etalon. Percentage data refer to fraction of idler energy of total output.

processes. On the other hand, the idler is generated in the forward and backward direction with respect to the pump beam, and the output mirror transmits typically only 66% of the idler as determined by a separate measurement. The idler also suffers absorption in some spectral regions within the crystal as shown by Fig. 21. To some extent, the loss of one component is shared by the other since the parametric buildup or pump depletion of one amplitude component is proportional to the amplitudes of the other components. For example, at the peak of the OH absorption band in the LiNbO_3 crystal, at $2.87 \mu\text{m}$, the idler, and the signal at the corresponding wavelength of $1.68 \mu\text{m}$, fail to oscillate. At the wings of this absorption band, e.g., at $2.79 \mu\text{m}$ and $3.10 \mu\text{m}$, the total output power is still depressed compared to that at $3.52 \mu\text{m}$, as seen in Fig. 23. The last column of Table V reflects the other losses experienced by the idler beam. For example, at $3.5 \mu\text{m}$, the quantum energy ratio $\lambda_s / (\lambda_i + \lambda_s)$ equals $1.5/5$ or 30%. Half of this percentage is propagating towards the input and only $2/3$ of the remaining 15% are transmitted by the output window. The fact that the measured ratio is not 10%, but actually 13% may be ascribed to losses experienced by the signal.

Aside from effects caused by the localized OH absorption peak, the general trend of the output power is monotonically towards lower values as tuning proceeds away from degeneracy. There are at least two causes for this behavior. First one obtains from Eq. (4) that tuning the (angular) signal frequency from the degeneracy point $\omega_p/2$ by a fraction δ higher to $1/2 \omega_p (1+\delta)$, and correspondingly the idler frequency to $1/2 \omega_p (1-\delta)$, reduces the gain parameter by the factor

$$\frac{\Gamma}{\Gamma_0} = (1-\delta)^2^{1/2} . \quad (24)$$

A second cause is absorption which increases for the idler with wavelength, as seen in Fig. 21 (after accounting for reflection of the crystal faces which are AR coated only for the resonating signal). The absorption affects also the signal power via the buildup process as discussed before.

The individual curves for output vs. input power are characterized by two parameters, viz., the oscillation threshold and the subsequent rate of output power increase or slope efficiency. In Fig. 23, these two parameters, which reflect gain and loss conditions for each operating point represented by a curve, show different trends.

Table VI presents oscillation thresholds and slope efficiencies with, and without, etalon operation for various tuning points on the signal wavelength scale. For this purpose, the high gain part of the output energy curves of Fig. 23 is approximated by a straight line through two representative points. The intersection of the straight lines with the pump energy scale is defined as threshold and the slope as the slope efficiency.

Table VI. Oscillation Thresholds and Slope Efficiencies for Various Tuning Points

Signal Wavelength μm	Oscillation Threshold		Slope Efficiency	
	without etalon mJ	with etalon mJ	without etalon %	with etalon %
2.13	140	239	19.2	18.2
1.93	190	252	18.3	16.9
1.72	217	260	18.3	11.6
1.62	285	304	23.3	18.3
1.53	220	275	23.0	18.0

The reproducibility of these data depends on tight control of alignment settings, as mentioned before, although individual measurements can be quite accurate. With this reservation, Table VI shows the interesting feature that although the oscillation thresholds vary over a considerable range, the slope efficiencies remain mostly close to 20%. Furthermore, there appears to be little correlation between threshold and slope efficiency. For example, for operation without etalon, the thresholds at 2.13 μm and 1.62 μm are 140 mJ and 285 mJ, respectively,

whereas the corresponding slope efficiencies are 19.2% and 23.3%. The practical significance of these relationships is that once threshold is reached, the output, even for tuning conditions of relatively high loss, increases with a slope efficiency of about 20%. Therefore, assume one obtains for a certain setting only 1 mJ output with 300 mJ pump energy, i.e., 0.3% overall efficiency. Then 50 mJ increase of the input, or 50 mJ decrease of the oscillation threshold, will apparently boost the output to 11 mJ. This represents an 11-fold improvement of overall efficiency for a 17% increase of pump power or decrease of threshold.

It appears difficult to establish a simple model for the interpretation of the features exhibited by Table VI and Fig. 23. However, certain inferences can be drawn from Eqs. (3) and (4). At phase match (center of generated frequency band) $\Delta k = 0$, so that the gain equals

$$G = \sinh^2 \Gamma L \quad (25)$$

for which the limiting values are

$$G = \Gamma^2 L^2 \text{ for } \Gamma L \ll 1 \quad (26)$$

$$G = 1/4 e^{2\Gamma L} \text{ for } e^{\Gamma L} \gg 1 \quad (27)$$

According to Eq. (4), Γ^2 is proportional to the pump intensity I . In the parametric cavity with various lossy elements including the 70% reflecting output mirror, the required gain for threshold oscillation and above is represented by Eq. (27) rather than (26). This is obvious also from Eq. (21), which with the measured values for the threshold, $I = 1.24 \times 10^7 \text{ W/cm}^2$ at $L = 6 \text{ cm}$, yields $\Gamma_0 L = 3.17$ and $e^{\Gamma_0 L} = 24$ at degeneracy. At phase match the gain is thus determined by

$$G = 1/4 \exp [C(1-\delta^2)^{1/2} I^{1/2} L] \quad (28)$$

where C is a constant obtainable by comparison with Eq. (4) and δ is again the fraction by which the parametric frequencies have been detuned from

degeneracy. However, inspection of Fig. 23 shows that, in the range of higher energies, the conversion yield is not exponential, but rather linearly increasing with flashlamp voltage, i.e., it is approximately proportional to I .

A model for the gain behavior at increasing pump energy can be conceived as an analog to the buildup of energy density with path length as a pulse propagates in a laser amplifier. Here, the energy density increases first exponentially until it reaches a level of stimulating emission at which it completely empties all stored energy in its path so that further buildup of energy density is linear with increasing distance.

In the case of parametric gain, we must assume that the conversion process depletes a central part of the pump beam to a point of saturation (e.g., 50%). There exist then, two possibilities. First, this central part may be literally the center of the radial intensity pattern of the pump beam. This part would saturate first after exponentially reaching a limiting value Γ_m . As the pump energy is further increased, the saturating beam area forms an expanding circle. Thus the output energy continues to increase, not exponentially, but rather more or less as I^α , where α is close to unity. Alternatively the central part of the beam may be a spectral region close to phase match which, according to Eq. (3) has the largest gain. As this region saturates, further increase of pump intensity brings the adjacent parts of the spectral gain profile to saturation. Again this frequency spreading of the maximum gain will proceed proportional to a low power, rather than exponential, order of the pump intensity. Although its role may not be dominant, such a mechanism must be involved because of the finite divergence of the pump beam. The various angular components of the beam generate responses of different frequency selection from the three tuning elements so that the broadening is partly inhomogeneous. A detailed experimental study examining the radial spot pattern and its spectral profile as a function of pulse energy of the signal and idler beam might indicate which, if any, of these models apply.

At any rate, the point of these, and of other similar, interpretations for the features in Fig. 23 and Table VI is that they predict an exponential increase of the gain up to the region around oscillation threshold and further a more linear increase as pump energy increases beyond that. This in turn explains the sharp increase of the threshold for increasing loss followed by a slope efficiency with little dependence on such loss. Such considerations are of significance for design plans of parametric converters with greater energy and efficiency.

OPO linewidth measurements of the final system from 1.5 to 2.1 μm performed with a Tropel scanning interferometer yielded a grating limited width of 2.0 cm^{-1} (FWHM). Introduction of the 0.5 mm etalon reduced this width to $0.4\text{--}0.6 \text{ cm}^{-1}$. A more accurate experiment was performed by displaying the fringe pattern of an interferometer with fixed spacing on the image tube of a Hamamatsu system. This limited measurements to the signal wave region around $1.9 \mu\text{m}$ because of the requirements that (1) the finesse of the measuring interferometer is known and (2) frequency doubling is used to accommodate the wavelength response of the image tube for fringe pattern display. The 0.5 mm etalon was found to produce a linewidth averaging 0.40 cm^{-1} . With a YAG:Nd pump linewidth of 0.15 cm^{-1} , the idler then assumes a linewidth of about 0.43 cm^{-1} (which will be approximated to 0.5 cm^{-1} in the examples of Section 8). Without the etalon, the average linewidth of the signal wave amounts to 2.0 cm^{-1} . Comparison of the solid and dashed curves in Fig. 23 shows that the introduction of the etalon reduces the pulse energies by a factor of about two. Nevertheless, the resolution improvement by about 4.6 implies that the etalon increases the pulse power per unit frequency interval by 2.3, aside from providing higher specificity. Introduction of the 1.0 mm etalon should produce a signal linewidth of 0.2 cm^{-1} , an idler linewidth of 0.25 cm^{-1} , and an increase of the spectral radiance by a factor of about 4, although in this case the absence of other etalon orders must be ascertained.

"On and Off" switching of frequency displacements by about 1 cm^{-1} reproduces the imaged fringe patterns within 0.04 cm^{-1} , i.e., within the limits of observation. Over periods of about 10 minutes, no linewidth changes were detectable. No systematic tests were performed in which the

reproducibility of tuning settings for crystal, grating, and etalon was measured after changes over large fractions of the tuning range. However, a high reproducibility was noted for the settings of these elements with respect to each other to achieve maximum power. This is ultimately due to the reproducibility of the galvanometer angle response to the control current after large excursions. Therefore, a corresponding operational stability and control reliability can be expected.

6. AUXILIARY SYSTEMS AND COMPONENTS

Research and development work in this project dealt in the main with devices in the art of optics and quantum electronics, and this report is largely confined to this domain. A larger part of the equipment delivered under this contract contains the support systems for the tunable laser. These systems serve the requirements of power supply, controls, timing, rod and lamp cooling, and inert gas supply to keep the surfaces of optical components dustfree. This equipment, itself, is the product of a considerable engineering and design effort. The detailed account of the systems and components involved, which include interlocks to prevent radiation damage, if, for example, water supply or rotator fail to function, is beyond the scope of this report. A detailed description of the auxiliary systems and directions for their operation, of cause, is contained in the Manual accompanying this report. However, a brief enumeration of the problems encountered in this engineering effort is pertinent.

The main power supply charges three capacitors (each 28 μ F, 2 KV) which have to deliver energy pulses of the required voltage and frequency to the two laser flashlamps. Instead of using the less efficient circuitry containing thyratrons or other gas tubes as rectifiers, the power supply contains transistor bridge networks which increase frequency and then magnitude of the line voltage before rectification to a stable d.c. voltage for the capacitors. The power supply for the Faraday rotator represents a novel feature in that it supplies the required high magnetizing currents only for the minimum duration necessary to provide radiative isolation around the time of Q-switching. No other problems were encountered here but the maximizing of efficiency and the design of interlocks which prevent Q-switching in case of rotator failure.

An electronic unit, described in the Manual, allows manual, or automatic alternating, tuning on and off a desired gas resonance line. Manual tuning is needed to establish the frequencies of maximum and minimum resonance (e.g., between rotational lines) by comparison with the gas monitor cell.

Dust prevention, especially on the ferroelectric crystals, represented another problem solved in several steps by care during assembly, confinement of the beam within hermetically secured enclosures and positive pressure of an inert gas.

Two pumps provide, respectively, cooling water for the flash-lamps and ethylene glycol for cooling and index-matching of the laser rods. To avoid the need for a connection to a water supply, the heat is transferred to air by an exchanger which in turn is cooled by fans.

7. CONCLUSIONS AND RECOMMENDATIONS

A number of conclusions have already been stated in this report or are at least implicit in it. A few of these suggest only an exchange of components, either with those already delivered or with items available commercially. Other conclusions however, were arrived at after the construction of the deliverable system reached its final stage with tests revealing the desirability of further changes which would have produced an unacceptable delay in delivery. Some of the latter class are included mainly as considerations for a second generation of parametric infrared tuning systems.

7.1 Acquisition of LiNbO₃ Crystals

Lack of quantity and quality of available LiNbO₃ crystals have created the most serious limitation in the performance of the system. Replacement of the presently installed crystal by one with lower oscillation threshold would immediately be expected to allow larger parametric output. Uncertainty of replacement possibilities, furthermore, have limited the range of parameters that were tested. This applies, for instance, to tuning the signal wavelength below 1.5 μm and to tests with various OPA conditions.

At the time of this writing, Crystal Technology is making an attempt to improve quantity and quality of their LiNbO₃ supply. We emphasize the need for the commercial supply of crystals with the transmittance shown in Fig. 22 (ref. 14).

7.2 Operation with the Parametric Amplifier

Provided LiNbO₃ crystals of lower oscillation threshold are obtained, tests with the OPA should be resumed. As discussed in Section 4.5, the gain conditions for the idler are particularly favorable for parametric amplification.

7.3 OPO Operation at the Limits of the Tuning Range

As shown in Fig. 1, at the limits of the tuning range the bandwidth of angle tuning is comparable to that of the grating and may be even less. At idler wavelengths above 3.5 μm , it may be advantageous to replace the grating by a plane mirror with a resulting decrease of cavity losses.

Another improvement for operation near the tuning limits is possible with an output mirror which is coated for high reflectivity near 1.45 μm , but again highly reflecting at 1.06 μm .

7.4 Alternatives for Linewidth Reduction

The system was delivered with an 0.5 mm thick etalon in the OPO cavity which can be exchanged for a 1 mm thick etalon that was also used previously. The thicker etalon has twice the resolution, but half the free spectral range, of the etalon with 0.5 mm thickness. If the tuning of the 1 mm etalon is not accurately centered on the peak of the grating spectrum, the etalon may pass two orders. The existence of this condition can only be discovered with a frequency analyzer, such as a scanning Fabry-Perot interferometer. If an analyzer is available, operation with the thicker etalon may be preferable. A compromise solution may be the acquisition of an etalon 0.75 mm thick.

A number of other alternatives exist for the reduction of the output linewidth, provided that the quality of the crystal is improved. First, a second etalon outside the cavity of 2-3 mm thickness will reduce the linewidth in proportion to the thickness and finesse. Although output power is in part sacrificed, the spectral irradiance available to a narrow absorption line may be unimpaired.

Another alternative is intracavity application of two etalons, typically of 0.8 mm and 5 mm optical path thickness. This can be accomplished without a construction change of the cavity. One replaces the etalon with a structure consisting of a silica etalon (which may be the 0.5 mm flat now in the cavity) and a flat parallel mirror (which may have a spacing of 5 mm) forming an air etalon with the adjacent surface

of the first etalon. It follows from the etalon equations that if a beam of wavelength λ_o has normal incidence ($\theta_i = 0$) on the etalon, a turn of the latter by $\Delta\theta_i$ will tune to $\lambda_o - \Delta\lambda$, where $\Delta\lambda \cong 1/2(\Delta\theta_i)^2 \lambda_o / n^2$. Since $\Delta\theta_i / n$ has the same value for both etalons, they tune to the same wavelengths, but the thin etalon passes a linewidth of about 0.3 cm^{-1} , whereas the air etalon narrows this width to about 0.05 cm^{-1} .

The two etalon system just described is capable of considerable variations. Instead of a mirror, a second etalon can be used forming essentially a three-etalon combination with an air-space etalon between the two silica etalons. Again, instead of keeping the two etalons parallel by a suitable flat ring, they may be rotated from the normal incidence position in opposite directions, $+\Delta\theta_i$ and $-\Delta\theta_i$, by simple gear connections with the galvanometer shaft. This has the effect of completely decoupling the two etalons from each other.

A solution for the problem of further line narrowing adopted by Professor Byer's group involves a major change of the parametric cavity. A prism of high index material (forming a one-dimensional telescope) is introduced in front of the grating. The effect of this is a spreading of the beam over a larger area of the grating with a corresponding increase of the grating resolution. This allows the use of an etalon with a correspondingly smaller free spectral range and linewidth.

7.5 Variation of the Parametric Amplifier Arrangement

In the planning of a second generation infrared parametric tunable system, the interactions and optical path arrangements between the parametric oscillator and amplifier should receive further attention. For example, one arrangement which had previously been considered and, perhaps unjustly, been rejected, is a single axis pump system. By this is meant that the pump beam proceeds, not from a beam splitter around the oscillator to the amplifier, but undivided from the (single pass) oscillator to the amplifier. In other words, from the oscillator, the three beams proceed together. The tuning angle of the second LiNbO_3 crystal compensates for walkoff. The arguments for this alternative are that even with a conversion efficiency as high as 20%, the oscillator

leaves 80% of the beam energy unconverted. If this portion is used for the amplifier, then it and the oscillator receive each more pump power than they could with the by-pass method in any conceivable combination. A 300 mJ pump pulse used on crystals of the quality they represent in the present system acts with 300 mJ on the oscillator and with 270 mJ on the amplifier. A further advantage is the great simplification in the alignment of a single axis system compared to the four mirror arrangement of the by-pass. A further study of this alternative is therefore indicated.

Another factor which reduces efficiency in parametric amplification (and to some extent also in oscillation) is the time required for the buildup of the oscillation which requires several transits of the resonating wave through the cavity, each of nL/c duration. In particular, the amplifier conversion process cannot even begin until threshold is reached in the oscillator, while in the meantime the pump pulse typically passes its peak. The buildup time is affected by the gain, the length of the cavity, and the number of transits required. Various trade-offs are possible, and the study of their optimization may lead to considerably higher overall efficiencies and output powers.

8. APPLICATION OF THE SYSTEM TO ATMOSPHERIC MEASUREMENTS

We discuss in the following the application of the system to the remote monitoring and measurement of pollutant and trace gases with estimates of the performance to be expected for many species of interest. Such estimates are possible by applying the previously derived² performance predictions for differential absorption spectroscopy to the values of output energy, tuning range, and linewidths measured with the present system. A further substantiation of the estimates is possible by a comparison to the performance observed in recent years with such other systems as have been used for remote infrared gas monitoring. These empirical results agree quite well with the predictions, as first noted³ for the case of CO.

8.1 Basic Relations

The Differential Absorption Spectroscopy method compares pulse power signals received from a target which scatters back radiation from a laser transmitter tuned alternatively on and off an absorption resonance line of the monitored gas. If the width of the laser line, $\Delta\nu$, is of the order of, or smaller, than the linewidth of the gas, the difference between the two signals is given by

$$\begin{aligned} P_r^{\text{off}} - P_r^{\text{on}} &= P_r^{\text{off}} (1 - e^{-2(N_{AR} + N_p L) \bar{\sigma}}) \\ &= (K_0 A P_o / \pi R^2) e^{-2\alpha_s c^R} (1 - e^{-2(N_{AR} + N_p L) \bar{\sigma}}) \end{aligned} \quad (29)$$

where, with the choice of symbols used before,²

P_r^{off} = power received with laser tuned off resonance

P_r^{on} = power received with laser tuned on resonance

N_A = number density of species molecules [cm^{-3}] occurring naturally in the atmosphere

R = range to backscattering target

L = thickness of pollutant cloud in the direction of the laser beam

N_p = number density of species molecules added to the atmosphere as pollutant, averaged over L

$\bar{\sigma}$ = absorption cross section of species at the laser frequency averaged over laser bandwidth

$P_o = E_o / \tau$ = transmitted laser power with pulse energy E_o during pulse width τ

ρ = fraction of radiation backscattered by target into unit solid angle

A = telescope mirror area

α_{sc} = attenuation coefficient of atmosphere due to scattering and absorption by coincidental resonance with other species

The backscattered fraction ρ equals either the diffuse reflectance of a dense target such as sand and water or, alternatively, the fraction $(c\tau/2)\beta(R)\pi$, i.e., the atmospheric volume coefficient of Mie-type back-scattering times the path length sampled by the laser beam during the pulse time τ .

The number of pollutant molecules encountered by the laser beam follows from Eq. (29):

$$N_p L = (1/2\bar{\sigma}) \ln(P_r^{\text{off}}/P_r^{\text{on}}) - N_A R \quad . \quad (30)$$

The signal-to-noise ratio, S/N, with which $N_p L$ can be measured by a given system depends on environmental optical parameters which can be optimized, if a choice exists. An example is the diffuse reflectivity of topographic targets¹⁷ which varies, depending on the target composition and the frequency, between 1% and 99%. Because of anomalous dispersion, sea water scatters back from 1% to 3% of normally incident radiation

between, respectively, about 2.7 and 3.6 μm . For beachsand, $\rho = 0.7$ at 2 μm and $\rho = 0.45$ at 4 μm , whereas for diverse leaf surfaces, ρ at 2.5 μm varies typically from 5%-15%. If the gas of interest has a sufficiently large spectral range of resonances within the tuning range of the OPO, a choice among them may depend on such frequency dependence of the target reflectances.

The application of aerosol as retroreflecting target encounters an even larger range of backscatter coefficients. For clouds,^{17,18} where a diffuse reflectance is the result of multiple scattering within a relatively small depth, $\rho = 0.4$ at 1.8 μm , $\rho = 0.55$ at 2.5 μm , and $\rho = 0.12$ at 3.0 μm . On the other hand, very much smaller ρ -equivalent values are obtained for volume backscattering by Mie particles in the clear atmosphere. For example, the pulse width of 40 nanoseconds delivered in the present OPO system produces a sampling depth $ct/2$ of 6 m. At 5 km visibility, with a Mie backscatter coefficient estimated at 0.2 km^{-1} , this yields an effective diffuse reflectance of $\rho \approx 1 \cdot 10^{-3}$. Integration of the received signal over 2 microseconds would increase that value to $\rho = 0.05$ at the expense of depth resolution which would increase to 300 m.

A corresponding range of values is encountered in the atmospheric attenuation α_{sc} which, if produced solely by Mie scattering, can be related¹⁹ to the visibility V by the relation

$$\alpha_{\lambda}^{\text{MIE}} = (3.91/V)(0.55/\lambda)^{0.585} V^{1/3} \text{ km}^{-1} \quad . \quad (31)$$

Equation (31) holds well for wavelength λ up to about 1.5 μm , but there is some question about its validity for laser radiation and for wavelengths larger than 1.5 μm .

To the extent to which a choice of accessible resonance frequencies exists, those with coincidences by other gases must be avoided. If the gas of interest has a natural abundance in the atmosphere with a density N_A , N_A must be either already known or it must be measured over a path not containing the gas as pollutant.

As described in reference (2), the detection and measurement of a pollutant may be quite difficult, if the pollutant has also a natural

abundance in the atmosphere and if it presents a large optical density $N_A R$ with tuning to the peak of the resonance line. Even if the pollutant does not occur naturally in the atmosphere, but is present in large quantities, it will saturate absorption. In either case, the signal-to-noise ratio can be maximized by optimized detuning from the resonance peak. This optimization is different for different purposes, namely, whether one merely wishes to detect the presence of a pollutant or whether one intends to measure, with maximum accuracy, the amount of pollutant encountered by the beam. The various cases can be summarized as follows:

(i) Detection, $N_A = 0$. As shown by Eq. (29), a maximum differential signal is obtained for a maximum optical density $2N_p L \bar{\sigma}_{\max}$. Hence, tuning to the peak of resonance is indicated.

(ii) Detection, $(N_A R + N_p L) \bar{\sigma}_{\max} > 1$. The differential signal component due to $N_p L$ has a maximum, if the laser is detuned from peak resonance so that the cross section is reduced from $\bar{\sigma}_{\max}$ to

$$\bar{\sigma}_{\text{opt}} = \ln(1+q)/2N_p L \quad (32)$$

where $q = N_p L/N_A R$. It is assumed that $N_A R$ is known. In the important case that $N_A R \gg N_p L$, the laser is tuned to the point for which

$$\bar{\sigma}_{\text{opt}} = (2N_A R)^{-1}, \quad N_p L \ll N_A R \quad (33)$$

According to Eq. (33), as $q \rightarrow 0$, $P_r^{\text{off}}/P_r^{\text{on}} \rightarrow e^{-1}$ so that optimal tuning adapts to the cross section at which $2R$ is the depletion length. On the other hand, for increasing q , optimal tuning according to Eq. (32) proceeds towards the peak of resonance until, in the limit, case (i) is reached. Actually, only one P_r point is needed, viz., that defined by Eq. (33). If the condition $P_r^{\text{on}}/P_r^{\text{off}} < e^{-1}$ is obtained, the pollutant is present in the observation path.

(iii) Measurement $(N_A R + N_p L) \bar{\sigma}_{\max} > 1$. Large optical densities of the pollutant, i.e., $N_p L \bar{\sigma}_{\max} \gg 1$, are easiest to qualitatively detect, yet difficult to quantitatively measure since the differential

signal reaches saturation. Since the measurement accuracy is inversely proportional to the noise of the detector, optimized tuning depends on the nature of the noise limitation. The detectors used in the infrared region are in general, limited either by background or dark current noise for which²

$$\bar{\sigma}_{\text{opt}} = 1.11/2(N_p L + N_A R) \quad . \quad (34)$$

For $N_A = 0$, the optimized cross section makes the path length $2L$ in the pollutant cloud equal to 111% of the depletion length. Experimentally, the optimum condition for measurement is reached when (for $N_A = 0$) $p_r^{\text{on}}/p_r^{\text{off}} = 0.33$.

8.2 Considerations of Linewidth Compatibility

The absorption cross section discussed in the preceding section depends not only on the frequency of the laser with respect to the peak of a resonance line, but on the widths of laser and molecular resonance lines as well. The integrated cross section (line strength) of a gas molecule

$$S = \int_{-\infty}^{+\infty} \sigma(v) dv \quad (35)$$

is independent of line shape and width. Therefore the cross section at the (monochromatic) frequency v_0 of the line peak is inversely proportional to the width of the absorption line:

$$\sigma(v_0) = CS/\gamma \quad (36)$$

where 2γ is the FWHM spectral linewidth and C is a form factor depending on the line shape (e.g., $C = 1/\pi$ for Lorentzians). If the spectral intensity distribution of the laser radiation is approximated by a rectangle of linewidth Δv , the averaged cross section $\bar{\sigma}$ is given by

$$\bar{\sigma} = (1/\Delta\nu) \int_{v_1}^{v_2} \sigma(v) dv, \quad \Delta\nu = v_2 - v_1 \quad . \quad (37)$$

It follows from Eqs. (35)-(37) that the averaged cross sections $\bar{\sigma}$ are in the limit of very small and very large laser linewidths, respectively:

$$\bar{\sigma} = \sigma(v_o) \quad \Delta\nu \ll \gamma \quad (38)$$

$$\bar{\sigma} = \frac{S}{\Delta\nu} = \frac{\sigma(v_o)}{c} \frac{\gamma}{\Delta\nu} \quad \Delta\nu \gg \gamma \quad (39)$$

The vibrational-rotational spectra of atmospheric gases may, or may not, be resolved into discrete rotational lines depending on whether the linewidths are, respectively, small or large compared with the frequency intervals between successive rotation lines.

At sea level, pressure broadening produces linewidths typically²⁰ of $2\gamma = 0.1-0.2 \text{ cm}^{-1}$ FWHM. At altitudes up to 20 km, pressure broadening remains dominant, so that the linewidth at a given temperature, is inversely proportional to the pressure. Above about 30 km, the lines are Doppler broadened to widths which vary typically from 0.001 cm^{-1} or less for relatively heavy molecules to 0.005 cm^{-1} or more for light molecules. Between 20 and 30 km altitude, the spectral profiles are convolutions of Lorentzian (pressure) and Gaussian (Doppler) distributions.

The linewidth of the present OPO is either 0.3 cm^{-1} or 0.5 cm^{-1} when used with the thick or thin etalon, respectively. In addition, it is possible to introduce a passive etalon in front of the detector. With an etalon finesse of three or five, respectively, a spectral width of 0.1 cm^{-1} is attained. With an optical path length $2L_{\text{OPO}} = 42.5 \text{ cm}$ for the round trip between grating and output mirror, the resulting mode spacing of 0.0235 cm^{-1} allows four longitudinal modes to be maintained within 0.1 cm^{-1} which, according to previous experience, should be sufficient for stability of pulse intensity. In the following we present a brief analysis examining the measurement conditions for which the application of an external etalon is either an advantage or disadvantage.

Up to elevations of several kilometers, the rotational lines within the vibrational bands of polyatomic molecules such as $C_x H_y$, SF_6 , and H_2O are mostly pressure broadened into pseudocontinua, although the peaks of a rotational structure may be superposed. In addition, there is considerable overlap of different bands. The exceptions are such linear polyatomic molecules as CO_2 and N_2O which have spacings of the rotational lines that are sufficiently large compared to the linewidth so as to display a discrete rotational structure. With the approach to the Doppler broadening regime at high altitudes, also some of the band continua are resolved into a discrete rotational structure,²⁰ albeit with a large number of lines per cm^{-1} .

Thus it appears that, for the remote density measurement of many polyatomic gases, the use of an external etalon offers no advantage. A width of $0.5 cm^{-1}$ probes either an increment of the band continuum or a corresponding number of rotational lines at high altitude monitoring. A reduction of the laser linewidth by an external etalon has then only the effect of reducing the total laser power received by the detector.

A different situation exists for molecular spectra in which the rotational spacing is (1) relatively large compared to the rotational linewidth, viz., for spacing-to-width ratios of 3:1 or more and (2) the band is not overlapped by another band. This condition applies to the spectra of diatomic molecules, linear polyatomic gases, and high J-value transitions of some of the other polyatomic gases. If the laser linewidth is larger than the width of the gas line, Eq. (29) has to be expressed in the more general form

$$P_r^{off} - P_r^{on} = P_r^{off} \left| 1 - \frac{1}{\Delta v} \int_{v_1}^{v_2} e^{-\sigma(v)(N_A R + N_P L)} dv \right| . \quad (40)$$

For small optical densities $2(N_A R + N_P L)\sigma(v_0)$ one obtains with Eq. (37) the simple expression

$$P_r^{off} - P_r^{on} = P_r^{off} \left| 1 - \frac{1}{\Delta v} \int_{v_1}^{v_2} \left| 1 - (N_A R + N_P L)\sigma(v) \right| dv \right| = (N_A R + N_P L)\bar{\sigma} P_r^{off} . \quad (41)$$

which is still accurate within 10% for an optical density as high as 0.2. For atmospheric pressure broadening one obtains from Eq. (37) and

$$\sigma(v) = \frac{S}{\pi} \frac{\gamma}{(v-v_o)^2 + \gamma^2} \quad (42)$$

the absorption cross section, averaged over $\Delta v = v_2 - v_1$:

$$\bar{\sigma}(v) = \int_{v_o - p_1 \gamma}^{v_o + p_2 \gamma} \sigma(v) dv = \frac{S}{\pi(p_1 + p_2) \gamma} (\tan^{-1} p_1 + \tan^{-2} p_2) . \quad (43)$$

Here the limits of the frequency interval Δv are expressed as $(v_o - p_1 \gamma)$, and $(v_o + p_2 \gamma)$, i.e., in terms of the deviations from exact resonance in units of the spectral HWM γ . Tuning to symmetrical overlap with the resonance line implies $p_1 = p_2 = p$ so that

$$\bar{\sigma}_{\max} = \frac{S}{\pi p \gamma} \tan^{-1} p . \quad (44)$$

Of particular interest is the case in which the FWHM-values for the laser and the spectral line are equal, i.e., $\Delta v = 2\gamma$, for which

$$\bar{\sigma}_{\max} = \frac{S}{4\gamma} = \frac{\pi}{4} \sigma(v_o) ; \quad p_1 = p_2 = p = 1 . \quad (45)$$

This cross section is thus $(\pi/4)$ of that at the peak of the resonance line, $\sigma(v_o)$, obtained from Eq. (42) and also from Eq. (44) for $p \rightarrow 0$.

The gain G in cross section resulting from decreasing a laser linewidth $\Delta v = 2p\gamma$ to 2γ is now obtained by forming the ratio of Eqs. (45) and (44):

$$G = \pi p / (4 \tan^{-1} p) . \quad (46)$$

For large p the gain approaches $0.5 p$ since $\tan^{-1} p \rightarrow \pi/2$. These results are based on a rectangular profile of the laser line spectrum of width $2p\gamma$. Actually, of course, the laser line has itself a maximum at the line center. Thus,

$$G = A(p)p \quad (47)$$

where $0.5 < A \leq 1$ for $p \geq 1$.

If these averaged cross sections are applied to Eq. (41) for the difference signal at small optical densities, it is found that reduction of the linewidth by a factor p changes $(P_r^{off} - P_r^{on})$ relatively little since the reduction of P_r^{off} to $(1/p)P_r^{off}$ is nearly compensated by the increase of σ . However, while linewidth reduction generates no increase in received difference signal, it may result in two other advantages. The first of these is specificity, viz., the exclusion of spectral lines from other gas species. A second advantage results for conditions in which the noise processed by the receiver system increases with the signal received. Such increase typically, varies as $P_r^{1/2}$, which is the case for shot noise limited detection. The limiting noise sources in infrared detectors are dark current or background radiation. The latter, which is dominant in high quality (high D^*) infrared detectors, represents essentially shot noise of the black body radiation continuum. Therefore, background noise is proportional to $p^{1/2}$, hence to $(P_r^{off})^{1/2}$; (note that the effect of linewidth has not been considered in reference 2, e.g., its Eq. (20), since the laser linewidth was assumed to be of the order of the spectral linewidth or smaller). It should be added that in pre-amplification and other data processing stages noise may increase with signal power, a consideration essential for the case where a small difference of much larger signals is to be measured. Assuming that such noise is also proportional to $p^{1/2}$, or that the infrared detector is background limited, there results in case of low optical densities for the ratios of signal-to-noise with and without etalon:

$$(S/N)_{\Delta\nu=2\gamma} / (S/N)_{\Delta\nu=2p\gamma} \approx p^{-1/2} \quad . \quad (48)$$

The case of larger optical densities, for which the linear expansion of Eq. (41) is not valid, is more difficult to evaluate analytically in a general form. However, one may again define a gain

function $G = A(p)p$ for the factor by which the absorption term, which contains the integral, changes after a reduction of the laser bandwidth. In peak-to-peak tuning of laser and gas line, absorption in the line center will saturate to unity with increasing optical density, while the wings of the gas line will produce still linearly increasing absorption. At high densities, $G(p)$ will thus become smaller than unity, i.e., a reduction of laser linewidth by a factor p will reduce the difference signal in Eq. (41) by a factor larger than p . Thus if one chooses peak-to-peak tuning for the measurement of large optical densities, the laser linewidth should remain at a size several times the width 2γ . Alternatively, one may choose to reduce the laser linewidth to about 2γ , provided one adopts the detuning conditions for optimized detection or measurement outlined in Section 8.1. In this latter case one has to some extent the advantages of specificity and S/N improvement possible for low optical density measurements. The choice will depend on the gas species and atmospheric conditions.

8.3 Examples for the Density Measurements of Specific Gases

A discussion of the measurement conditions for specific gases on the basis of the preceding considerations can be compared, at least in some cases, with experimental observations over the last few years. At these laboratories measurements have been made with low-energy, temperature-tuned OPO systems on CO , H_2O , and vinyl chloride, mostly on cell samples at low pressures. Byer and his group have published a more systematic study²¹ of the capabilities offered by high energy OPO systems for the measurement of many gases. The publication²¹ (still in preprint form at the time of this writing) also summarizes measurements with the OPO of gases *in situ* or in cells of H_2O , CO_2 , SO_2 , and CH_4 . A data base of atmospheric line parameters is available from tapes.²²

On the basis of the analytical evaluations and experiments already performed, we summarize in the following the measurement possibilities for the present OPO system. These estimates are based on the capabilities of the OPO system, as delivered to NASA-Langley, in terms of

tuning range, pulse energies, and linewidths. However, examples will be cited in which we state explicitly the advantage or necessity of such provisions as external etalons, insertion of the amplifier components, and replacement of LiNbO_3 crystals by specimens of higher quality.

Estimates of the signal-to-noise ratios are based on a detector NEP of $1 \times 10^{-11} \text{ W Hz}^{-1/2}$. However, detectors with considerably lower noise equivalent powers are available. The attenuation coefficients due to scattering were chosen relatively high, and lower values apply especially under optimized atmospheric conditions. The application of these and other improved parameters would, of course, increase the estimated values for S/N and the range R.

8.3.1 H_2O

The measurement of H_2O densities is of interest for the remote determination of humidity and temperature.²³ In Eq. (29), then, $N_p = 0$ and $R = L$. Within the OPO tuning range water vapor exhibits two strong absorption regions at $1.9 \mu\text{m}$ and $2.7 \mu\text{m}$, respectively, each containing three (overlapping) bands. This absorption makes measurements of any gas impossible between $5,100-5,500 \text{ cm}^{-1}$ and $3,300-3,950 \text{ cm}^{-1}$, if large amounts of water vapor are encountered in the observation path (long path, high humidity). However, suitable lines of intermediate intensity can be found outside these limits. Examples²³ are lines at 5650.41 cm^{-1} and 5651.33 cm^{-1} . An example for lines of intermediate strengths which overlap under atmospheric pressure broadening is the region around a line at $5,641.48 \text{ cm}^{-1}$ ($1.77 \mu\text{m}$). Here operation of the OPO with 0.5 cm^{-1} FWHM would integrate over 4 lines spread over a width of 0.26 cm^{-1} . The intensities of these 4 lines quoted²⁴ for 287.7°K in units of $[\text{cm}^{-1}/(\text{gm cm}^{-2})]$ add up to 0.292. It is possible to estimate the optical density NL of the 3.33×10^{22} molecules in one gram/cm^2 of water along a path length L with Eq. (39). Here S is the sum of the intensities contributed by the four lines of the 3.33×10^{22} molecules in the path. For $\Delta\nu = 0.5 \text{ cm}^{-1}$, this yields for the optical density the value 0.58. At sea level and 78% humidity at 15°C an atmospheric path length of 1 km contains just one gram/cm^2 of water vapor. Under these conditions, absorption over $2R = 2 \text{ km}$ amounts

approximately to $1 - \exp(-1.16) = 0.69$. Equation (29) with $K=0.1$, $\rho=0.1$, $A=10^3 \text{ cm}^2$, and $\alpha_{SC}=0.4$, then yields for the difference signal $P_r^{\text{off}} - P_r^{\text{on}} = 9.6 \times 10^{-11} P_o$. At the wavelength chosen in this example, the OPO is tuned to the signal frequency corresponding to $1.77 \mu\text{m}$, where about 5 mJ pulse energy are available with internal etalon for the pulse duration of $4 \times 10^{-8} \text{ sec}$. Assume further that telescope elements reduce the energy by a factor of three to 1.67 mJ. If the infrared detector has a Noise Equivalent Power (NEP) of $1 \times 10^{-11} \text{ W Hz}^{-1/2}$, the noise power $2\text{NEP} \cdot (\tau)^{-1/2}$ equals $1 \times 10^{-7} \text{ watt}$. Thus the resulting signal-to-noise ratio is $S/N = 40$ for a single pulse pair. A humidity measurement of 1% accuracy would require 6 pulse pairs (i.e., 2.5 sec at 5 pps).

By order of magnitude, this estimate agrees with the results of Endemann and Byer²³ if it is considered that lower ρ -values were available to them from their observation platform, but that the pulse rate was higher and the pulse length shorter.

8.3.2 Temperature Measurements

The determination of absolute humidities can be carried²³ out simultaneously with a measurement of the accompanying temperature, preferably by reducing the laser bandwidth to 0.1 or 0.2 cm^{-1} . The method compares two absorption lines originating in transitions which start from thermally excited states for at least one of them. Because the population densities in the initial states follow the Boltzmann distribution at a given temperature, the latter can be measured by the difference in optical densities.

A more direct, but probably less accurate, method of temperature measurement is possible, if it is possible to scan through and identify the P- and R-branches of a vibrational-rotational band. In diatomic gases the peaks of these two branches are separated by a frequency difference²⁵ $\Delta\nu_{PR}^{\text{max}} = 2.3583(BT)^{1/2} \text{ cm}^{-1}$, where B is the rotational constant. Similar relationships exist for polyatomic molecules. Thus the measurement consists essentially of frequency determinations and involves intensities only indirectly for locating the branch maxima. It may be worthwhile to analyze the potential of this method in greater detail.

8.3.3 HC1

The fundamental vibration band of HC1 is centered at 2886 cm^{-1} and is accessible to the idler wave tuning range of the OPO. The P(4) line at 2798.94 cm^{-1} has an absorption cross section of $\sigma(v_0) = 60 \times 10^{-18} \text{ cm}^2$ at a Doppler limited linewidth²⁰ of $\gamma_D = 0.0029 \text{ cm}^{-1}$. A pressure limited linewidth of $\gamma_p = 0.05 \text{ cm}^{-1}$ should reduce the cross section to $\sigma(v_0) = 3.5 \times 10^{-18} \text{ cm}^2$. Thus a laser beam encountering in its path $2.9 \times 10^{17} \text{ molecules/cm}^2$ is depleted in its intensity to $1/e$, which occurs at 1 ppm HC1 in the atmosphere for a depletion length of 108 m. Measurements should therefore be possible for 0.01 ppm over 1 km.

Tuning with internal etalon to the P(4) line of HC1 should be possible with a pulse energy of 1 mJ (see Fig. 23). As discussed in Section 8.2, a further external etalon may enhance S/N, especially if the optical density $2N_p L \sigma \ll 1$, i.e., smaller than about 0.2-0.3. However, measurement of HC1 pollutant concentrations will be of particular interest for the environment of a localized source. Assume such source produces 1 ppm HC1 at sea level over a depth of $L = 100 \text{ m}$ so that for $\Delta v = 2\gamma_p$, there results $\bar{\sigma}_{\max} = (\pi/4)\sigma(v_0) = 2.7 \times 10^{-18} \text{ cm}^2$ and $2\bar{\sigma}_{\max} N_p L = 1.5$. A laser bandwidth $\Delta v = 0.5 \text{ cm}^{-1}$ then reduces the cross section according to Eqs. (44) and (45) by a factor $\pi p/(4\tan^{-1} p) = 2.9$ for $p=5$. Hence $2\bar{\sigma}_{\max} N_p L = 0.55$ so that a $\Delta v = 0.5 \text{ cm}^{-1}$ laser linewidth is adequate. Using otherwise the same parameters as in Section 8.3.1, a pulse pair should yield $S/N = 5$ for 1 mJ and $R = 1 \text{ km}$. However, the choice of parameters may be too conservative: 10% accuracy, rather than 1%, may be adequate for HC1 density measurements; the scattering coefficient α_{sc} can be expected to be considerably smaller at $3.5 \mu\text{m}$ than at $1.77 \mu\text{m}$ for equal atmospheric conditions; and reflectivities larger than 0.1 may be applicable. Thus ranges of 2 km or more may be quite feasible. Experimental results, with which these estimates can be compared, apparently do not yet exist. It is, of course, a separate question, if and how HC1 vapor interacts with other atmospheric constituents, especially, H_2O .

8.3.4 CO

The vibrational overtone band centered near 4233 cm^{-1} is accessible to the idler range of the OPO. A good choice may be the R(10) line at $4,300\text{ cm}^{-1}$ ($2.325\text{ }\mu\text{m}$) which is relatively strong and located near the degeneracy point of the OPO. According to Fig. 23, about 5 mJ without etalon and 2 mJ with etalon should be available in this region.

According to our own measurements,³ the cross section* of the strongest overtone lines is $1.5 \times 10^{-21}\text{ cm}^2$ at a laser bandwidth of $\Delta\nu = 0.35\text{ cm}^{-1}$. Cross sections of this order limit the measurement range to relatively large concentrations. For 1,000 ppm CO over $L = 100$ meter depth, i.e., 10 atm cm, the optical density $2\sigma LN$ is about 0.81. Using the parameters for K , ρ , A , α_{sc} , and NEP of Section 8.1, Eq. (29) yields now $P_r^{\text{off}} - P_r^{\text{on}} = 1.29 \times 10^{-6}\text{ W}$ (after allowing for a factor of three loss in the telescope). Thus $S/N = 13$ for a single pulse pair.

The reliability of these estimates can be assessed on the basis of the previous experiments³ with remote monitoring of CO. The signal-to-noise ratios obtained then agreed within a factor two with predictions based on Eq. (29) and the known detector NEP. The accuracy of the density measurement was about 5% for one second integration. This is about the same accuracy to be expected in the present example for 2 pulse pairs.

Because of the small cross section of the CO overtone absorption lines, the optical density will often be small enough to use an external etalon to advantage in the background limited detection regime.

8.3.5 SO₂

The fundamental vibration bands of SO₂ are located at frequencies smaller than $1,400\text{ cm}^{-1}$. Overtone and combination bands have higher frequencies, but even the combination band closest to the OPO range (and still of intermediate intensity) centers at 2499 cm^{-1} ($4.00\text{ }\mu\text{m}$). To be

*This cross section measured in the laboratory and reduced to the value for $2\gamma_p = 0.11\text{ cm}^{-1}$ is about three times smaller than that cited in Ref. (21).

useful in that range, the present OPO has to be refitted with LiNbO_3 crystals of larger transmittance at the long-wavelength end of the tuning range. Inclusion of the amplifier section with its particular advantage for the augmentation of idler power is also necessary. Under such conditions the possibility of measuring SO_2 densities with an OPO system has been demonstrated.²¹ OPO output mirrors with reflectivities high near $4 \mu\text{m}$ represent another factor of improvement. Because of dense spacing of the rotational lines, if resolved at all, an internal etalon is unnecessary.

8.3.6 CO_2 , C_xH_y , and Other Gases

The analysis presented so far can be easily extended to other gases accessible to the tuning range of the present OPO (with improvements indicated, where necessary). Table VII summarizes the input data for some of these, as well as the previously considered, gases. Frequencies and wavelengths are listed in Col. II and III and the peak cross sections of the pressure broadened lines in Col. IV. Col. V presents OPO linewidths with or without etalons. Col. VI shows the product of gas concentration C (in ppm) and path length L_p (m) necessary to deplete the pulse energy to $1/e$ in double pass for the linewidths in Col. V. As pointed out before, however, it may be advantageous to narrow the laser linewidth to 0.1 cm^{-1} , especially when a single line and low optical density is encountered. On the other hand, the wider laser bandwidth may overlap other gas lines not resolved. Except for H_2O , this could not be considered in Col. VI. Thus for C_xH_y and NO_2 , the depletion lengths may be shorter than indicated. Col. VII represents the output energies of the present OPO system. In general, the spectra of C_xH_y encounter coincidences with H_2O . Col. VIII indicates the lines for which H_2O absorption is particularly important.

Table VII. Cross Section and Energy Data of OPO System Application to Various Gases

I Gas	II ν_o (cm ⁻¹)	III λ_o (μm)	IV $\sigma_p(\nu_o)$ (10^{-18} cm ²)	V $\Delta\nu$ (cm ⁻¹)	VI CL_p (ppm.m)	VII E_o (mJ)	VIII Remarks
CO ₂	4983	2.007	0.21	0.5	9.7×10^6	12.0	P(8), P(10), or P(36)
CH ₄	2948.7	3.391	0.4	0.5	1700	0.9	
	3057.69	3.270	2.0	0.5	340	1.5	
C ₂ H ₆	2976.8	3.359	0.5	0.5	1400	1.0	H ₂ O Coincid.
C ₃ H ₈	2948.7	3.391	0.8	0.5	850	0.7	
	2967.6	3.370	3.1	0.5	220	1.0	H ₂ O Coincid.
C ₂ H ₄	2962.5	3.338	0.06	0.5	1.1×10^5	1.0	
H ₂ S	3789	2.639				2.4	
NO ₂	2910	3.436	0.12	0.5	5700	0.75	H ₂ O Coincid.
N ₂ O	2545	3.92					w. crystal improvement, ampl.
	3481.68	2.87	0.03	0.5	3300	1.0	w. crystal improvement
H ₂ O	5641.48	1.772	$1.9 \cdot 10^{-5}$	0.5	9.7×10^6	5.0	
HC1	2798.94	3.573	3.5	0.5	190	1.0	
CO	4300	2.325	$1.5 \cdot 10^{-3}$	0.35	1.6×10^5	2.0	
SO ₂	3499	4.002		2.0			w. crystal improvement, ampl.

APPENDIX I. SPECTRAL CHARACTERISTICS OF OPTICAL ELEMENTS IN OPO

The transmission and reflection characteristics of the optical coatings used in the OPO are reproduced in Figs. 24-27. The data are presented in the form which was received from the coating manufacturers. The "Operations and Maintenance Manual for the Westinghouse Parametric Infrared Tunable Laser System" Sec. 6, p. 36 lists the specifications for each component and the vendors capable of making the coatings at the time the report was written.

Curve 724526-8

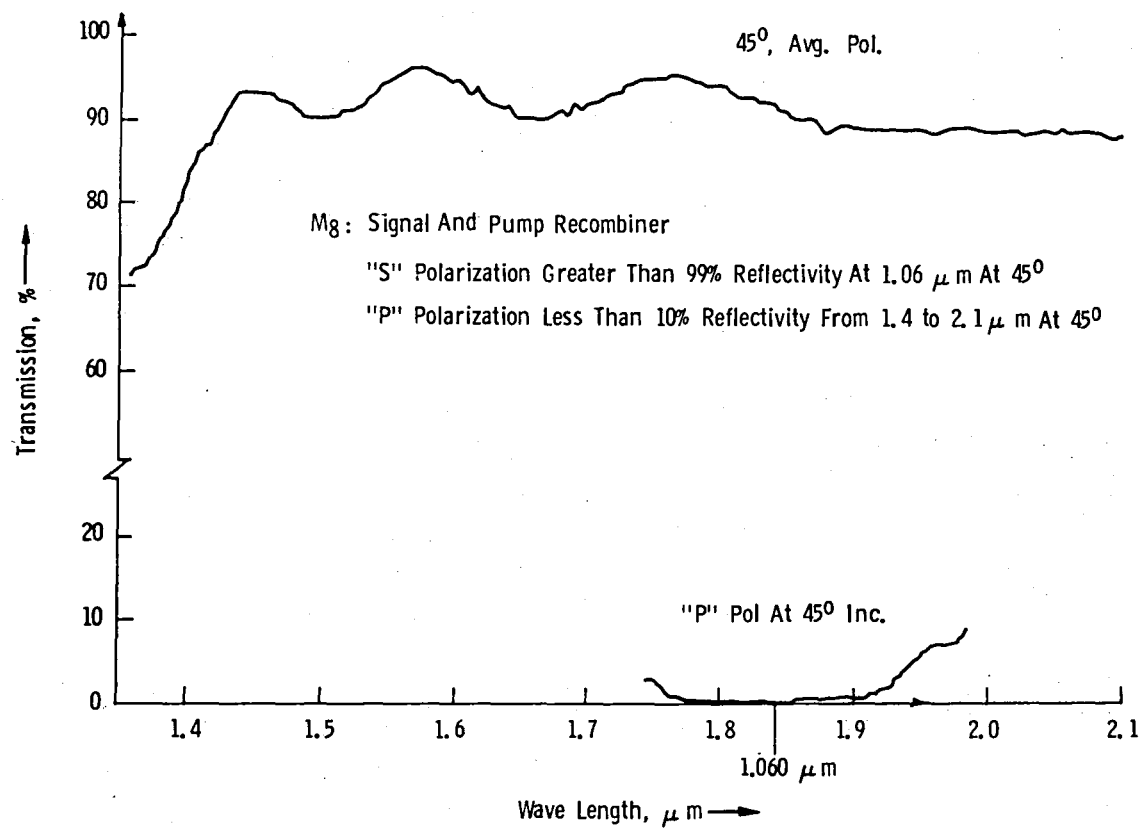


Fig. 24. Signal and pump recombiner, M_8 , from curve trace received from manufacturer (UVIRA).

Curve 724527-8

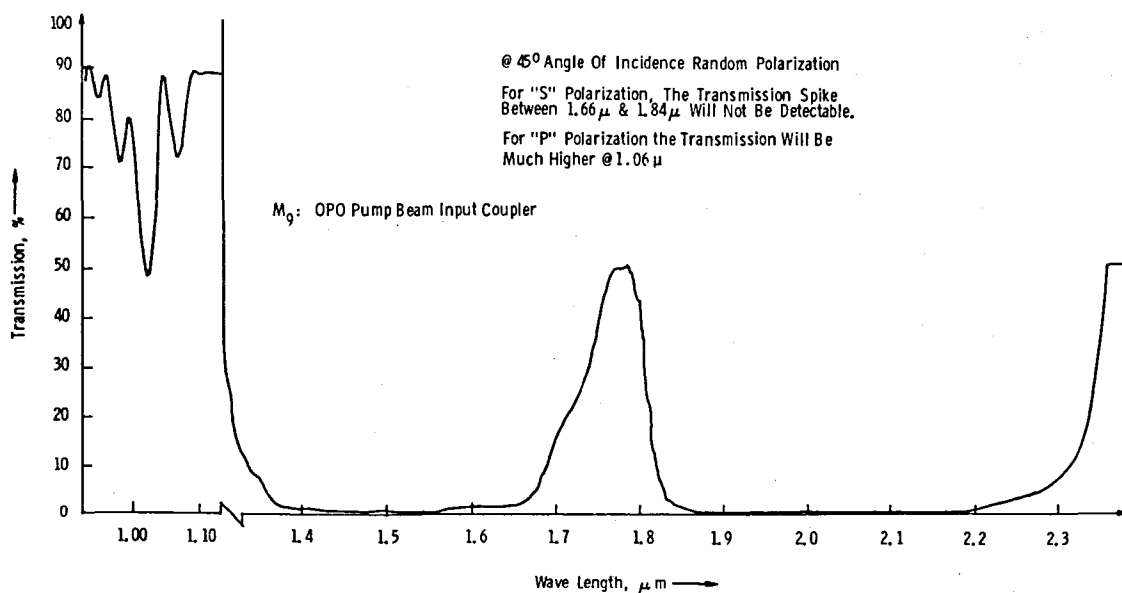


Fig. 25. OPO pump beam input coupler, M₉, reproduced from curve trace received from manufacturer (UVIRA).

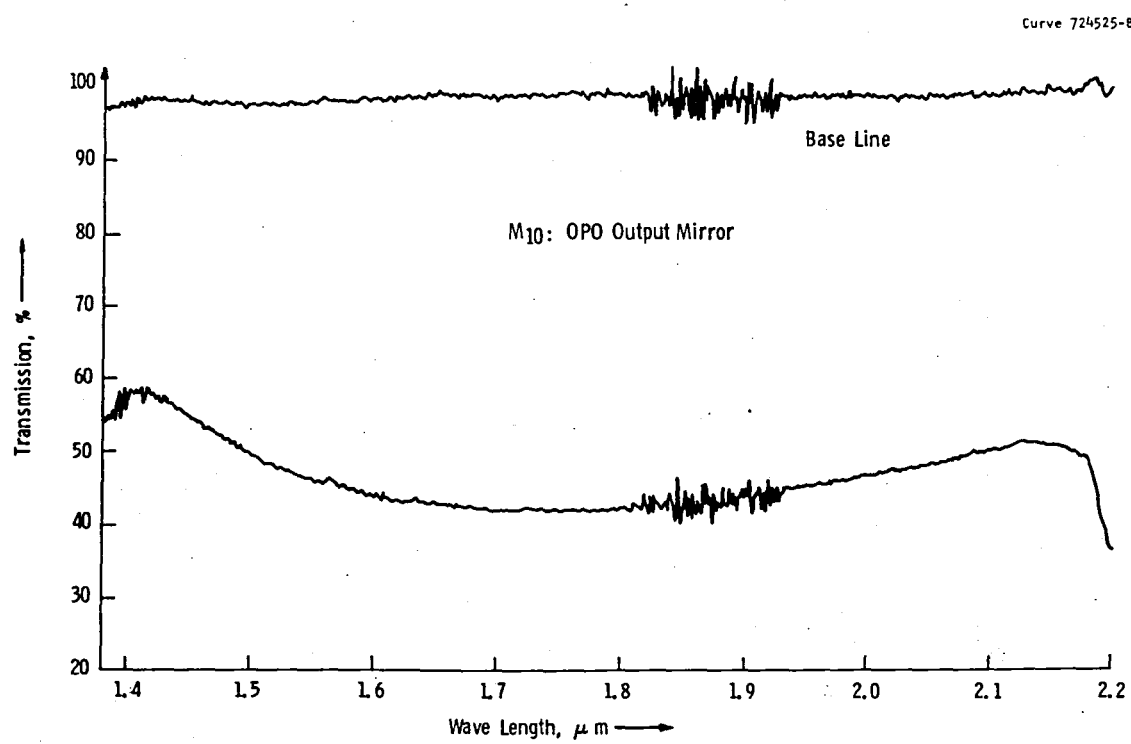


Fig. 26. OPO output mirror, M₁₀, reproduced from curve trace received from manufacturer (UVIRA).

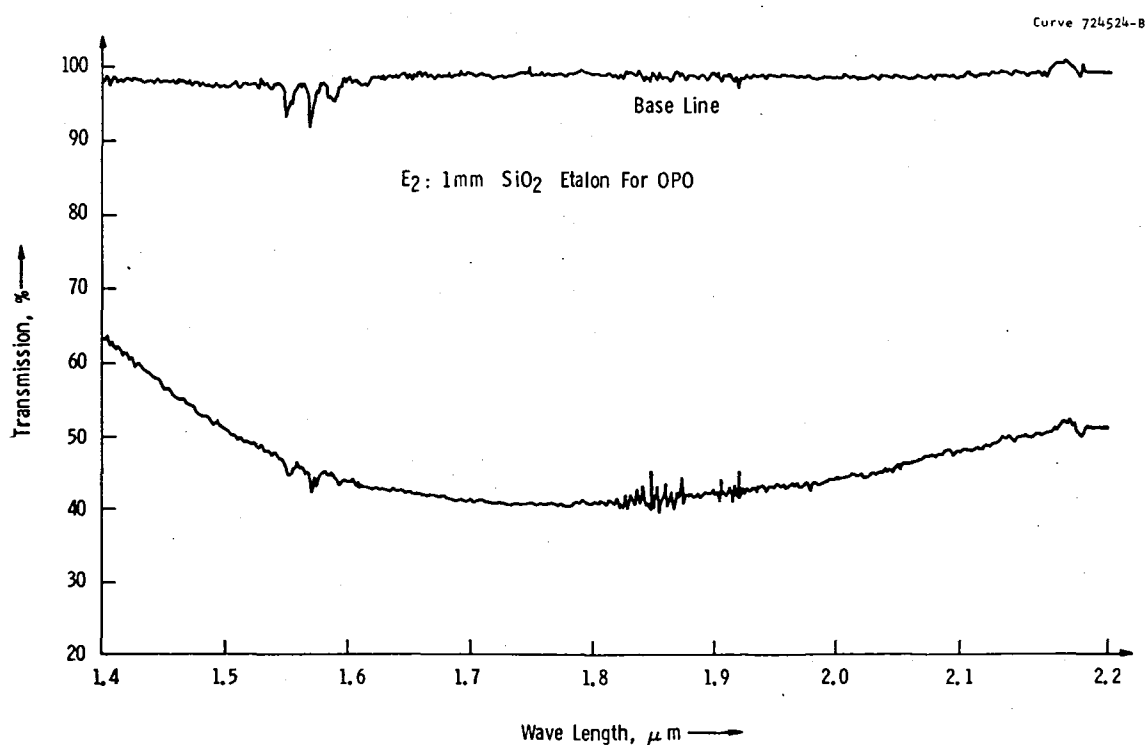


Fig. 27. Etalon for OPO, E₂, reproduced from curve trace received from manufacturer (Airtron).

REFERENCES

1. H. Kildal and R. L. Byer, Proc. IEEE 59, 1644 (1971).
2. R. L. Byer and M. Garbuny, Appl. Opt. 12, 1496 (1973).
3. T. Henningsen, M. Garbuny and R. L. Byer, Appl. Phys. Lett. 24, 242 (1974).
4. S. E. Harris, Proc. IEEE 57, 2096 (1969).
5. R. L. Herbst, R. N. Fleming and R. L. Byer, Appl. Phys. Lett. 25, 520 (1974).
6. T. Henningsen and J. J. Conroy, U.S. Patent No. 405770 (Acousto-Optic Q-Switch).
7. A. E. Siegman, "Unstable Optical Resonators for Laser Applications", Proc. IEEE 53, 277 (1965).
8. See, for example, A. Yariv, "Introduction to Optical Electronics", Holt, Rinehart and Winston, New York (1971).
9. T. Henningsen, "Evaluation of CaLaSOAP:Nd for Use in a One-Joule 30 Hz Laser Designator", Westinghouse Research Report 72-1C1-LAMAT-R1, July 1972.
10. A. E. Siegman and H. Y. Miller, Appl. Optics 9, 2729 (1970): "Unstable Optical Resonator Loss Calculations Using the Prony Method", see also A. E. Siegman, Laser Focus, p. 42, May 1971.
11. M. Hercher, "Tunable Single Mode Operation of Gas Lasers Using Internal Tilted Etalons", Appl. Opt. 8, 1103 (1969).
12. M. Born and E. Wolf, "Principles of Optics", 2nd ed. MacMillan (1964).
13. R. L. Byer, R. L. Herbst and R. N. Fleming, "A Broadly Tunable IR Source", Proc. 2nd Int. Conf. on Laser Spectroscopy, June 1975, Megeve, France, pp. 206-226, Berlin, Springer, 1975.
14. K. Nassau, M. J. Levinstein and G. M. Loiacono, "Ferroelectric Lithium Niobate, Part 2", J. Phys. Chem. Solids, 27, 989 (1966).
15. R. L. Byer, R. L. Herbst, R. S. Feigelson and W. K. Kway, "Growth and Application of [01.4] LiNbO₃", Opt. Commun. 12, 427 (1974).

17. W. L. Wolfe and G. J. Zissis, "The Infrared Handbook", IRIA Center (1978).
18. M. L. Wright, E. K. Proctor, L. S. Gasiorek, and E. M. Liston, "A Preliminary Study of Air-Pollution Measurement by Active Remote-Sensing Techniques" NASA CR-132724, National Aeronautics and Space Administration, Langley Research Center, June 1975.
19. P. W. Kruse, L. D. McGlauchlin, and R. B. McQuistan, "Elements of Infrared Technology" (Wiley, New York, 1963).
20. For a general review of this subject, see "Laser Monitoring of the Atmosphere", in Topics in Applied Physics, E. D. Hinkley, Ed., Springer, New York (1976).
21. M. Endemann and R. L. Byer, "Remote Atmospheric Measurements in the Near Infrared Using a Reliable OPO-Source", to be published.
22. R. A. McClatchey, W. S. Benedict, S. A. Burch, R. F. Calfee, K. Fox, L. S. Rothman, J. S. Garing, "AFCRL Atmospheric Absorption Line Parameter Compilation", AFCRL Report-TR-73-0096 (1973).
23. M. Endemann and R. L. Byer, Optics Lett. 5, 452 (1980).
24. W. S. Benedict and R. F. Calfee, "Line Parameters for the 1.9 and 6.3 Micron Water Vapor Bands", ESSA, Profess. Paper No. 2 (1967).
25. G. Herzberg, "Molecular Spectra and Molecular Structure", 2nd ed., D. Van Nostrand (1950).

NASA Contractor Report 159310

Distribution List
NAS1-13752

	<u>No.</u> <u>Copies</u>
NASA Langley Research Center Hampton, VA 23665	
Attn: Report and Manuscript Control Office, Mail Stop 180A Technology Utilization Office, Mail Stop 139A Dr. Edward V. Browell, Mail Stop 401A	1 1 20
NASA Ames Research Center Moffett Field, CA 94035	
Attn: Library, Mail Stop 202-3	1
NASA Dryden Flight Research Center P. O. Box 273 Edwards, CA 93523	
Attn: Library	1
NASA Goddard Space Flight Center Greenbelt, MD 20771	
Attn: Library	1
NASA Lyndon B. Johnson Space Center 2101 Webster Seabrook Road Houston, TX 77058	
Attn: JM6/Library	1
NASA Marshall Space Flight Center Marshall Space Flight Center, AL 35812	
Attn: Library, AS61L	1
Jet Propulsion Laboratory 4800 Oak Grove Drive Pasadena, CA 91103	
Attn: Library, Mail Code 111-113	1
NASA Lewis Research Center 21000 Brookpark Road Cleveland, OH 44135	
Attn: Library, Mail Stop 60-3	1
NASA John F. Kennedy Space Center Kennedy Space Center, FL 32899	
Attn: Library, NWSI-D	1
National Aeronautics and Space Administration Washington, DC 20546	
Attn: EB-8	1
NASA Scientific and Technical Information Facility 6571 Elkridge Landing Road Linthicum Heights, MD 21090	
	29 plus original

1. Report No. NASA CR-159310	2. Government Accession No.	3. Recipient's Catalog No.	
4. Title and Subtitle PARAMETRIC INFRARED TUNABLE LASER SYSTEM		5. Report Date November 1980	
		6. Performing Organization Code	
7. Author(s) M. Garbuny, T. Henningsen, and J. R. Sutter		8. Performing Organization Report No. 80-9C1-NASSA-R2	
9. Performing Organization Name and Address Westinghouse Electric Corporation Research and Development Center Pittsburgh, Pennsylvania 15235		10. Work Unit No.	
		11. Contract or Grant No. NAS1-13752	
		13. Type of Report and Period Covered Contractor Report	
12. Sponsoring Agency Name and Address National Aeronautics and Space Administration Washington, D.C. 20546		14. Sponsoring Agency Code	
15. Supplementary Notes Contract Monitor: Dr. Edward V. Browell, NASA Langley Research Center			
16. Abstract A parametric tunable infrared laser system was built to serve as transmitter for the remote detection and density measurement of pollutant, poisonous, or trace gases in the atmosphere. The system operates with a YAG:Nd laser oscillator-amplifier chain which pumps a parametric tunable frequency converter. This is the final report on work under a contract in which Westinghouse undertook to perform the necessary applied research, development, design, construction, and delivery. The completed system produced pulse energies of up to 30 mJ. The output is tunable from 1.5 to 3.6 μm at linewidths of 0.2-0.5 cm^{-1} (FWHM), although the limits of the tuning range and the narrower linewidths can be obtained only with lower energy. A simple replacement of the nonlinear crystals presently in the parametric converter by samples of the higher quality already demonstrated is expected to improve the system performance further. The system was delivered to NASA-Langley in February 1980.			
17. Key Words (Suggested by Author(s)) parametric, tunable, infrared, laser, systems, delivery, remote, gas, density, detection, measurement, pollution, poison		18. Distribution Statement Unclassified - Unlimited	
19. Security Classif. (of this report) Unclassified	20. Security Classif. (of this page) Unclassified	21. No. of Pages 115	22. Price*

End of Document